VOLUME 20 NO. 2 | JULY 2026
P-ISSN: 1411-1616 | E-ISSN:2549-8215

JURNAL ILMIAH BERKALA SAINS DAN TERAPAN KIMIA

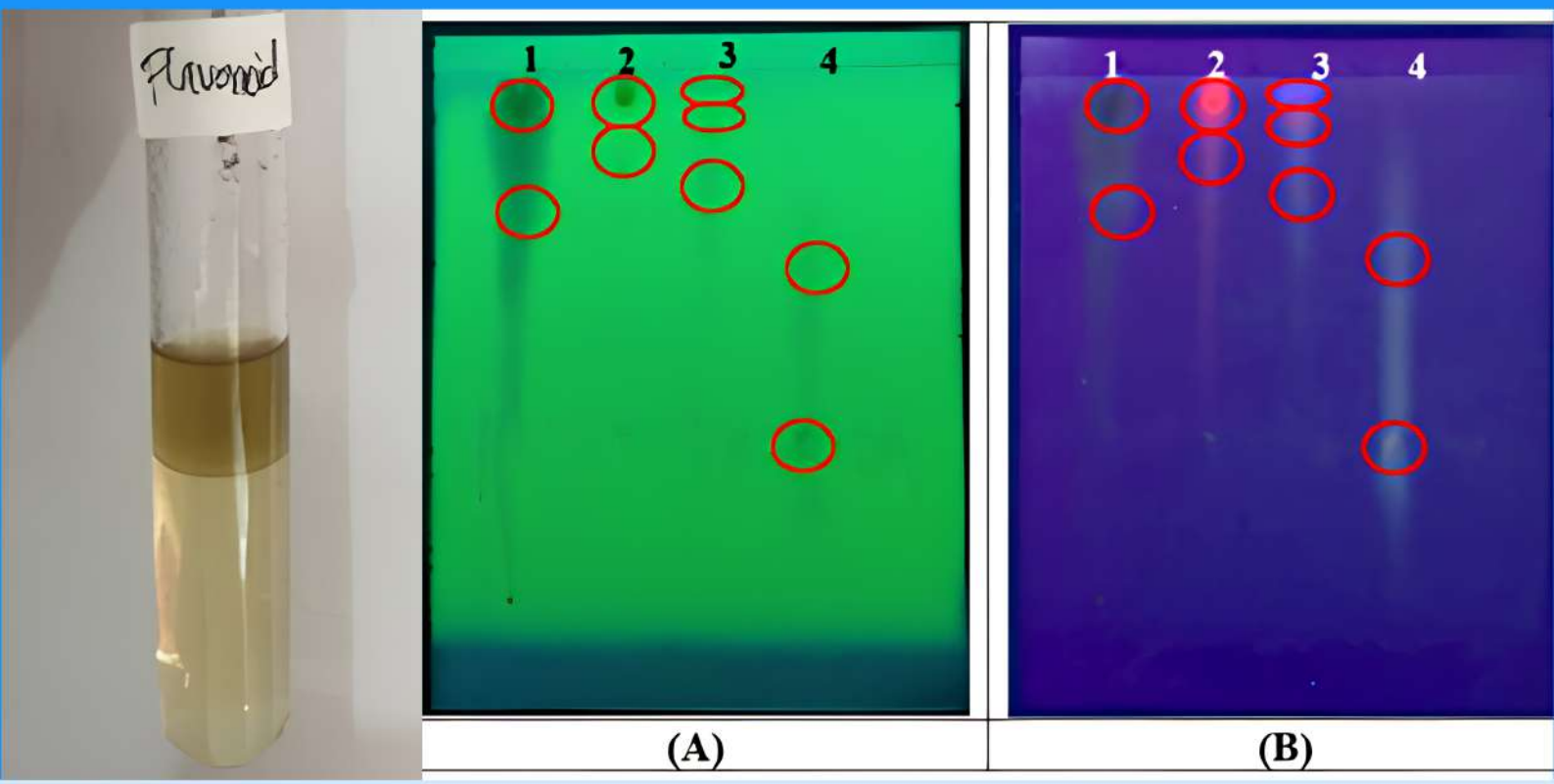

Qualitative Identification of Flavonoid Compound by Shinoda Test and TLC Method (Esati *et al*, p. 61-62)

JURNAL ILMIAH BERKALA
SAINS DAN TERAPAN
KIMIA

PUBLISHED BY:
DEPARTMENT OF CHEMISTRY, FACULTY OF MATHEMATICS AND NATURAL SCIENCES
UNIVERSITAS LAMBUNG MANGKURAT, INDONESIA

SUPERVISORY BOARD

Head of Department of Chemistry, Faculty of Mathematics and Natural Sciences, Universitas Lambung Mangkurat

PUBLISHER

Department of Chemistry, Faculty of Mathematics and Natural Sciences, Universitas Lambung Mangkurat University, Indonesia

MAILING ADDRESS

Jl. A. Yani Km. 36 Banjarbaru, Kalimantan Selatan , Indonesia 70714
Phone: 0511-4773112, 0511-4782899
Email: jstk@ulm.ac.id

FIRST EDITION: 2007

EDITOR IN CHIEF

Rahmat Eko Sanjaya

EDITORIAL BOARD

Managing Editor : Dyah Ayu Pramoda Wardani

Editorial Board Members:

Gusrizal (Universitas Tanjungpura)
Sunardi (Universitas Lambung Mangkurat)
RR. Dirgarini Julia Nurlianti Subagyono (Universitas Mulawarman)
Sura Menda Ginting (Universitas Bengkulu)
Yuana Nurulita (Universitas Riau)
Dahlena Ariyani (Universitas Lambung Mangkurat)
Ahmad Budi Junaidi (Universitas Lambung Mangkurat)
Nawwal Hikmah (Universitas Lambung Mangkurat)
Muddatstsir Idris (Universitas Lambung Mangkurat)
Amalia Khairunnisa (Universitas Lambung Mangkurat)
Abdul Aji (Institut Teknologi Sumatera)
Fatiha Khairunnisa (Universitas Airlangga)
Herdayanto Sulistyo Putro (Institut Teknologi Sepuluh Nopember)
Ika Fitriani Juli Palupi (Politeknik Industri Logam Morowali)
Rendy Muhamad Iqbal (Universitas Palangka Raya)

Reviewer for this Issue: Jurnal Ilmiah Berkala Sains dan Terapan Kimia Vol. 20, No. 2, July 2026

Umi Baroroh Lili Utami (Universitas Lambung Mangkurat)
Utami Irawati (Universitas Lambung Mangkurat)
Achmad Ramadhanna'il Rasjava (Universitas Lambung Mangkurat)
Aulia Rhamdani Arfan (Universitas Lambung Mangkurat)
Tety Wahyuningsih Manurung (Universitas Palangka Raya)
Darmawan Ali Saputra (Universitas Airlangga)
Andifa Anugerah Putra (Universitas Airlangga)
Ardiana Ilham Nurrohman (Universitas Lambung Mangkurat)

SITE EDITOR AND ADMINISTRATOR

Otok Pujinarko

ABOUT US

(Jurnal Ilmiah Berkala) Sains dan Terapan Kimia publishes scientific articles in the Chemistry field which include, but not limited to, research in chemistry, theoretical chemistry, and applied chemistry. This journal also publishes review articles about the development of chemistry. All the articles in this journal will go through a peer-review process to ensure that the quality of the article meets our standard before being published. Each article submitted to our journal will be reviewed by a reviewer having the expertise in the field. Shall the article submitted is deemed acceptable to be published in our journal, it is the writer's responsibility to make the necessary change and revision as recommended by the reviewer.
This journal is open access journal which means that all content is freely available without charge to users or / institution. Users are allowed to read, download, copy, distribute, print, search, or link to full text articles in this journal without asking prior permission from the publisher or author.

Sains dan Terapan Kimia (Jurnal Ilmiah Berkala) is published twice a year on January and July. There is no fee for authors to submit their manuscripts to be considered for publication in this jurnal. When the article is accepted for the publication. The publication fee is IDR 350.000,00 that covers article processing and DOI processing charge. Payment should be made by bank transfer to this account below

Bank	: BNI Banjarbaru
Account Number	: **107840008**
Account Name	: Dahlena Ariyani

Please send a confirmation of your proof of payment to jstk@ulm.ac.id

TABLE OF CONTENTS

Total Flavonoid Content and Antioxidant Activity of Three Fractions Vernonia amygdalina Del. from Bali…….....58-67
Ni Ketut Esati*, Indah Sri Wiratini, Kadek Duwi Cahyadi

Integration of Machine Learning and Digital Image Colorimetry in Green Synthesis Nanoparticle Logam: A Systematic Review …….. 68-80
Tiara Juliani*, Aceng Ruyani, and M Lutfi Firdaus

The Role and Isolation Techniques of Breast Milk Folate Binding Protein.....81-95
Subandrate*, M. Irsan Saleh, Dwirini Retno Gunarti, Hermansyah, Mohamad Sadikin

Development of Molecularly Imprinted Polymer (MIP) Modified Electrode for The Analysis of Fructose Content in Honey by Cyclic Voltammetry.....96-115
Salma Hananda Putri and Pirim Setiarso*

In Silico Identification of Natural Compounds as Potential FGF2 Inhibitors for Glioblastoma Therapy.....116-129
Nico Berlinson Fernando, Siti Hodijah, Agus Kartono, and Setyanto Tri Wahyudi*

JURNAL ILMIAH BERKALA SAINS DAN TERAPAN KIMIA

Jurnal Ilmiah Berkala: Sains dan Terapan Kimia
Vol. 20 No. 2, July 2026

Total Flavonoid Content and Antioxidant Activity of Three Fractions *Vernonia amygdalina* Del. from Bali

Kandungan Flavonoid Total dan Aktivitas Antioksidan Tiga Fraksi dari *Vernonia amygdalina* Del. Asal Bali

Ni Ketut Esati[1]*, Indah Sri Wiratini[2], Kadek Duwi Cahyadi[1]

[1]Department of Pharmacy, Faculty of Pharmacy and Health Sciences, Universitas Pendidikan Nasional, Denpasar 80224, Bali, Indonesia
[2]Department of Pharmacy, Sekolah Tinggi Farmasi Mahaganesha, Denpasar 80226, Bali, Indonesia

*Email: esati@undiknas.ac.id

ABSTRACT

The antioxidant was commonly used in daily life. It was a compound that was used to inhibit free radicals. The antioxidant could reduce the negative impacts of free radicals, such as damage to cell components. The public has widely used herbal plants as antioxidants. One plant known to have antioxidant activity was African leaves (Vernonia amygdalina Del.). African leaves from Bali were studied in this research. Known that a plant of the same species but in a different place of life can provide different secondary metabolite content depending on the environmental conditions in which the plant lives. This research aimed to determine total flavonoid levels and antioxidant activity fractions (n-hexane; ethyl acetate; aqueous) of African leaves extract from Tabanan (Bali). Extraction was carried out by maceration method using ethanol. The total flavonoid content of each fraction was tested using the colorimetric method ($AlCl_3$ reagent), while the antioxidant activity used the DPPH radical reduction method. The results of this study obtained total flavonoid levels in the ethyl acetate, n-hexane, and aqueous fractions, respectively, were 12.668%; 1.469%; and 0.031%. The ethyl acetate fraction provided the highest flavonoid content. The antioxidant activity was shown from the IC_{50} value, reducing the value caused the antioxidant activity to become higher. The IC_{50} were 82.596 mg/L; 121.077 mg/L; and 70.101 mg/L for the ethyl acetate, n-hexane, and aqueous fractions, respectively. Therefore, it can be concluded that the aqueous fraction of African leaves extract provides better antioxidant activity than others.

Keywords: *Vernonia amygdalina Del.; total flavonoid; antioxidants; fraction*

Received: 30 November 2022; **Accepted**: 13 April 2026: **Available online**: 29 July 2026

1. INTRODUCTION

Many people use antioxidants in their daily life. Antioxidants are compounds that function as free radical scavengers, so they can reduce the negative effects of free radicals. Therefore, antioxidants from outside the body are needed to assist in counteracting free radicals by donating one electron to unstable reactive free radicals. In addition, antioxidants can also chelate transition metal ions, such as Fe and Cu, so that new free radicals are not formed through chain reactions (Yuslianti, 2019). The use of herbal plants as antioxidants has been widely carried out by the community. One of the plants known to have antioxidant activity is African leaves (Vernonia amygdalina Del.). Based to Hasibuan et al. (2018), the n-hexane, ethyl acetate, and ethanol fraction of African

leaves from Medan City, North Sumatra are known to have antioxidant activity based on the IC50 value, which is 297.33 ± 0.46 g/mL; 177.99 ± 0.32 g/mL; 37.92 ± 1.03 g/mL (Hasibuan et al., 2014). Secondary metabolites known to act as antioxidants in the African leaves are flavonoids. Flavonoids have four mechanisms of action as antioxidants, namely capturing free radicals, binding metals so that metals are not oxidized, suppressing enzymes associated with the formation of free radicals, and stimulating the production of endogenous antioxidants (Banjarnahor & Artanti, 2014).

Based on Suhendy et al. (2022), African leaves extract from Jatinangor City, West Java has a total flavonoid content of 0.20 gQE/100 g (n-hexane extract); 0.58 gQE/100 g (ethyl acetate extract); 0.31 gQE/100 g (methanol extract), which correlates to the EC50 value of each African leaves extract, which is 717.50 g/mL (n-hexane extract); 740.28 g/mL (ethyl acetate extract); 1800.46 g/mL (methanol extract) (Suhendy et al., 2022).

However, differences in total flavonoid content in the African leaves can be influenced by several factors, such as environment, geography, and season. In environmental conditions with high temperatures, plants will increase ROS in plants causing cell damage. Plants adapt by producing compounds that are antioxidants as a form of defense against the environment, such as flavonoids so that high-temperature environmental conditions can increase flavonoid content in plants (Utomo et al., 2020). It was known that the quality of the active compounds contained in the plants will be influenced by land conditions, climate and the conditions in the environment where the plants live. This was also confirmed by Sholekah (2017), that secondary metabolites were formed from primary metabolites through various metabolic pathways which were influenced by several environmental factors. These factors such as light, temperature, pH, altitude and temperature influenced the phytochemical content. The phytochemical content such as flavonoids and beta carotene from a plant will differ in each region, influenced by environmental factors.

Based on research by Esati et al. (2021), stated that there was flavonoid content in the n-hexane, ethyl acetate, and African leaves aqueous fraction from Tabanan, Bali, but the total flavonoid content had not been determined and had not been tested for its antioxidant activity. Therefore, the researcher wants to continue This study was conducted because of the reported content of flavonoid compounds, so it is necessary to measure total flavonoid content and test the antioxidant activity of African leaves from Tabanan (Bali), then related to the effect of flavonoid compounds on antioxidant activity.

2. MATERIALS AND METHODS

2.1. Materials

African leaves (*Vernonia amygdalina* Del.) from Bali, 2,2-diphenyl-1-picrylhydrazyl (DPPH) powder (EMSURE®), quercetin (EMSURE®), powder Mg (EMSURE®), and other reagent in laboratory grade. Separating funnel (HERMA), TLC elution vessel (CAMAG), TLC plate (Merck TLC silica gel G_{60} F_{254}), UV-Vis spectrophotometer (THERMO SPECTRO GENESIS 10V-VIS), centrifugator (IPC), and evaporator (IKA).

2.2. Methods

2.2.1 Extraction of African leaves

A total of 480 g of African leaves powder was macerated with 1.5 L of 96% ethanol for 72 hours, then filtered to obtain the filtrate. The residue obtained was carried out with the same treatment. The filtrate is collected and evaporated (Depkes RI, 2000).

2.2.2 Flavonoid phytochemical screening in African leaves extract

A total of 0.2 g of extract was added to 10 mL of aquadest, then heated for 5 minutes, cooled and filtered. Take 5 mL of the filtrate, then add 0.1 g of Mg powder, 1 mL of HCl, and 2 mL of amyl alcohol. The mixture is shaken and allowed to separate (Depkes RI, 1995).

2.2.3 Fractionation

A total of 10 g of African leaves extract was dissolved in 50 mL of aquadest and 20 mL of 96% ethanol, then filtered. The filtrate was put into a separating funnel, then added *n*-hexane, shaken until homogeneous. Allow to stand until a layer of *n*-hexane and aqueous is formed. The aqueous layer was partitioned using ethyl acetate with the same treatment. Each layer was evaporated to obtain three types of fractions, i.e., *n*-hexane, ethyl acetate, and aqueous (Rukmana, 2019).

2.2.4 Identification of flavonoids

The African leaves extract fraction was analyzed using the TLC method with a mixture of eluents *n*-butanol-glacial acetic acid-water with ratio 4:1:5. The fraction was spotted on a silica gel plate and eluted. The elution results were detected under UV lamps at 254 nm and 365 nm, then the spots were spotted using NH_3 vapor (Markham, 1988).

2.2.5 Determination of total flavonoid content

The quercetin main standard solution was prepared in a series of 10-100 mg/L. Standard working solution of 40 mg/L quercetin was pipetted 0.5 mL, added 1.5 mL of 96% ethanol, 0.1 mL of $AlCl_3$, 0.1 mL of 1M potassium acetate, and added aquadest up to the mark in a 5 mL volumetric flask. It was left for 30 minutes, then the absorption spectrum was observed at 200-800 nm using a UV-Vis spectrophotometer.

A total of 25 mg of each fraction was put into a 25 mL volumetric flask, then dissolved in 96% ethanol to the mark. Pipette 0.5 mL of each fraction and the working standard solution of quercetin, add 1.5 mL of 96% ethanol, 0.1 mL of $AlCl_3$, 0.1 mL of 1M potassium acetate, and add aquadest up to the mark in a 5 mL volumetric flask. It was allowed to stand for 30 minutes, then the absorbance was measured at the maximum wavelength. The blank used was a mixture of 1.5 mL of 96% ethanol, 0.1 mL of $AlCl_3$, 0.1 mL of 1M potassium acetate, and added aquadest to mark the limit in a 5 mL volumetric flask (Depkes RI, 2017).

2.2.6 Antioxidant activity test

Antioxidant activity test using DPPH radical reduction method. Measurement of the maximum wavelength of the 40 mg/L DPPH solution in the range of 400-800 nm using a UV-Vis spectrophotometer was carried out. African leaves extract fractions were made in several concentration series, namely the *n*-hexane fraction (50, 100, 150, 200, 250 mg/L), while the ethyl acetate and aqueous fractions (20, 40, 60, 80, 100 mg/L). Quercetin was used as a positive control, made in several concentration series, namely 2, 3, 4, 5, and 6 mg/L. A total of 2 mL of 40 mg/L DPPH solution was added with 2 mL of fraction solution of each concentration, incubated for 30 minutes at room temperature, and in a dark container.

The negative control used was 2 mL of 40 mg/L DPPH solutions added with 2 mL of 96% ethanol. The mixture of fraction and negative control solution was measured for absorbance at the maximum wavelength of DPPH. The test was replicated three times. The absorbance obtained is used to determine the percent attenuation, then plotted with the concentration to determine the IC_{50} and AAI values (Rukmana, 2019).

2.2.7 Data analysis

Total flavonoid content was statistically analyzed with the help of SPSS using the One-Way ANOVA test and the post-hoc test using the Bonferroni test. IC_{50} and AAI values were processed using Microsoft Excel

3 RESULTS AND DISCUSSION

3.2 Extraction and screening flavonoid phytochemicals

The extraction results of 480 g of dried African leaves simplicia (*Vernonia amygdalina* Del.) by maceration and remaceration methods one time using 96% ethanol as solvent are shown in **Table 1**. Extracts were identified qualitatively with flavonoids which showed positive results containing flavonoids are presented in **Table 2**.

In this study, the maceration method was used because maceration is an extraction method that does not use high temperatures so that it is effective on thermolabile compounds, then followed by remaceration to extract compounds that are still left behind during the maceration process. This step was carried out for 72 hours to obtain the optimal compound. This is supported by Ningrum (2017), who said that the maceration time of 72 hours resulted in an increase in extract yield compared to 24 hours and 48 hours.

Table 1. The yield of African leaves extract

Sample	Extract weight (g)	Yield percentage (w/w)
480 g of African leaves simplicial	31.8	6.625

Table 2. Qualitative identification of flavonoid compound in African leaves extract

Test	Reagent	Result	
		Color	Picture
Shinoda	Mg powder, HCl $_{(p)}$, amyl alcohol	The yellow color on the amyl alcohol layer	

However, from the extract data, obtained a low percent yield (6.625%). This is thought to be influenced by the amount of solvent used is not sufficient in attracting compounds in the African leaves extract. Based on Depkes RI (2017), the ratio of simplicia and solvent during extraction is 1:10, while in this study a ratio of 1:3 was used. The extract was tested for phytochemical screening as a preliminary test to determine the presence of flavonoid compounds contained in the African leaves with the Shinoda test using Mg powder, HCl, and amyl alcohol. Mg and HCl aim to reduce the benzopyran core in the flavonoid structure so that a yellow flavilium salt is formed (Ergina, 2014), as shown in **Table 2**. This is in accordance with research by Kharimah *et al*. (2016), which showed that African leaves extract from West Java was positive for flavonoids. The content of secondary

metabolites in plants is influenced by several factors, such as geographical influences, temperature, and nutrients where plants grow (Cannel, 2005).

2.3. *Fractionation and identification of flavonoid*

The results of the fractionation of 10 g extract using the liquid-liquid extraction method using *n*-hexane, ethyl acetate, and water as solvents are shown in Table 3. Each fraction was then identified as its flavonoid content by the thin layer chromatography (TLC) method, then evaporated with NH_3, as presented in **Fig. 1**. The extract was fractionated with three solvents with different polarities, then identified flavonoids using TLC. This was done to ensure that the fractions of African leaves extract from Tabanan (Bali) contain flavonoid compounds. In **Fig. 1**, it can be seen that there are differences in color spots in the fractions of African leaves extract and quercetin as a comparison. Based on Markham (1988), the difference in color spots is thought to be due to the presence of different types of flavonoids. The spots in the *n*-hexane and ethyl acetate fractions there are orange spots on a 365 nm UV lamp suspected of the presence of flavonols, while in the aqueous fraction there are light blue spots indicating the presence of isoflavones.

Table 3. The yield of African leaves extract fractions

Sample	Fraction weight (g)	Yield percentage % (w/w)
Aqueous fraction	0.9158	9.158
Ethyl acetate fraction	0.6399	6.399
N-hexane fraction	3.0046	30.046

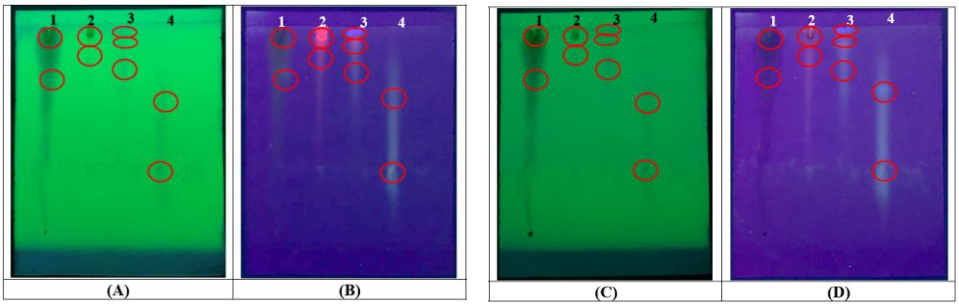

Figure 1. The result of flavonoid identification by the TLC method

Description:
A = TLC plate before evaporation of NH_3 on a 254 nm UV lamp; B = TLC plate before evaporation of NH_3 on a 365 nm UV lamp; C = TLC plate after evaporation of NH_3 on a 254 nm UV lamp; D = TLC plate after evaporation of NH_3 on a 365 nm UV lamp; spots from quercetin (1); *n*-hexane fraction (2); ethyl acetate fraction (3), and aqueous fraction (4)

2.4. *Determination of total flavonoid content*

Determination of total flavonoid content using quercetin as a standard solution and obtained the maximum wavelength of quercetin is 430 nm. The linear regression equation obtained from the standard solution of quercetin was used to calculate the total flavonoid content of each African leaves extract fraction with the results presented in **Table 4**. Determine of total flavonoid content in each African leaves extract fraction using the colorimetric method with an $AlCl_3$ reagent. The principle of this method is the formation of a stable complex with C-4 keto groups, as well as at C-3 or C-5 hydroxyl groups of flavones and flavonols which produces a yellow color. $AlCl_3$ reagent forms an acid labile complex with ortho-hydroxyl groups on the A- or B- ring of flavonoid compounds. The addition of potassium acetate aims to detect the presence of a free 7-hydroxyl group in the sample (Markham, 1988). The linear regression equation obtained is y = 0.067x + 0.0139 with an R^2 value of 0.9901, while the r-value is 0.995 which is close to the value of one. This shows that there is a positive relationship between the concentration (x) and the absorbance (y) of the solution on a linear line. The higher the concentration of quercetin solution, the higher the absorbance obtained (Gandjar & Rohman, 2018). Based on statistical analysis, a significant value was obtained (<0,005), indicating that there was an average difference between the African leaves extract fractions.

The ethyl acetate fraction had the highest total flavonoid content compared to the *n*-hexane and aqueous fractions (Table 4). Similar to Suhendy *et al*. (2022) stated that the total flavonoid content in the ethyl acetate extract of African leaves from West Java (0.584±0.050 gQE/100g) was higher than that of the *n*-hexane extract (0.197±0.063 gQE/100g) and methanol (0.315±0.007 gQE/ 100g). This is presumably because it is influenced by the semi-polar nature of ethyl acetate, so it can attract flavonoids with different polarities according to the principle of "*like dissolves like*" (Seidel, 2005).

Table 4. Total flavonoid content of African leaves extract fractions

Sample	Absorbance	Total flavonoid content±SD (% b/b)	Sig.*
Aqueous fraction	0.016	0.031±0.079	
n-Hexane fraction	0.112	1.469±0.048	<0.05
Ethyl acetate fraction	0.863	12.668±0.127	

*One-way ANOVA test, there are significant differences (<0.05)

2.5. *Antioxidant activity test*

The results of the antioxidant activity test showed that the maximum wavelength of DPPH was 517 nm which was used to measure the absorbance of the sample on a UV-Vis spectrophotometer. The results of IC_{50} values are presented in **Tables 5-8**. Each African leaves extract fraction was tested for its antioxidant activity using the DPPH radical reduction method. According to Maesaroh et al. (2018), the DPPH radical reduction method is the most effective method compared to the FRAP and FIC methods because it has high sensitivity. This can be seen based on the lowest LoQ and LoD values, which indicate that the DPPH radical can still be reduced by samples at low concentrations.

Table 5. Antioxidant activity of aqueous fraction of African leaves extract

Concentration (mg/l)	Average of absorbance	Inhibition percentage	Regression linear equation	IC_{50} (mg/L)	Category*
20	0.398	34.647	Y = 0.3156x + 27.876 R^2 = 0.9628	70.101	Moderate
40	0.360	40.941			
60	0.324	46.798			
80	0.305	49.973			
100	0.233	61.686			

Table 6. Antioxidant activity of *n*-hexane fraction of African leaves extract

Concentration (mg/l)	Average of absorbance	Inhibition percentage	Regression linear equation	IC_{50} (mg/L)	Category*
50	0.374	38.588	Y = 0.1504x + 31.79 R^2 = 0.9642	121.077	Weak
100	0.306	49.808			
150	0.290	52.381			
200	0.245	59.770			
250	0.175	71.210			

Table 7. Antioxidant activity of ethyl acetate fraction of African leaves extract

Concentration (mg/l)	Average of absorbance	Inhibition percentage	Regression linear equation	IC_{50} (mg/L)	Category*
20	0.444	27.094	Y = 0.364x + 19.935 R^2 = 0.9516	82.596	Moderate
40	0.386	36.563			
60	0.361	40.777			
80	0.333	45.320			
100	0.249	59.113			

Table 8. Antioxidant activity of quercetin

Concentration (mg/l)	Average of absorbance	Inhibition percentage	Regression linear equation	IC_{50} (mg/L)	Category*
2	0.497	18.391	Y = 14.023x – 5.9112 R^2 = 0.9812	3.987	Very strong
3	0.368	39.628			
4	0.294	51.779			
5	0.210	65.572			
6	0.149	75.534			

*The IC_{50} category is based on (4) which states that values >250 mg/l (very weak), 100-250 mg/l (weak), 50-100 mg/l (moderate), and 10-50 mg/l (very strong) (Phongpaichit, et al., 2007)

The principle of the DPPH radical reduction method is that when the DPPH solution reacts with an antioxidant compound, the compound will donate its hydrogen atom to the DPPH. The electrons on the nitrogen atom of DPPH are reduced by accepting a hydrogen atom from the reacted antioxidant compound. The DPPH radical is called a stable free radical because one free atom has moved to another atom. If the DPPH solution is mixed with antioxidant compounds that donate hydrogen atoms, it can cause the violet color of the DPPH solution to disappearing. This shows that antioxidant compounds reacted with DPPH have the ability to reduce the activity of DPPH free radicals (Yuslianti, 2019).

Antioxidant activity test in this study was carried out using a mixture of 40 mg/L DPPH solution, then incubated for 30 minutes. According to Molyneux (2004), 30 minutes is the optimal time for DPPH radicals to react with the sample. The mixture will experience a color change from dark purple to pale purple or pale yellow. This is because the sample has donated a hydrogen atom to the DPPH radical, resulting in a reduced form of the DPPH radical (Maesaroh et al., 2018). The aqueous fraction of African leaves extract from Tabanan (Bali) has better antioxidant activity (IC_{50}) than the ethyl acetate and *n*-hexane fractions (Table 5). The lower IC_{50} value indicates that at low concentrations, the sample has been able to reduce DPPH radicals by 50% (Molyneux, 2004).

Decrease in IC_{50} value was caused many factors, not only total flavonoid content in the extract, there were other factors that affect the antioxidant activity of the African leaves extract fractions, such as the effect of solvent polarity and other secondary metabolites that are thought to act as antioxidants.

Based on Gaffar et al. (2022) stated that the antioxidant activity of *n*-hexane extract of African leaves was low because non-polar solvents contained few compounds that could donate electrons or hydrogen atoms. Water solvents have high polarity, so they can attract polar secondary metabolites, such as alkaloids, tannins, flavonoids, and saponins found in the African leaves (Alara, 2017). This is still a presumption due to the limitations of this study, namely not carrying out further purification of flavonoid compounds in each fraction of African leaves extract from Tabanan (Bali).

4. CONCLUSIONS

Based on the research that has been done, it can be concluded that: there are differences in the total flavonoid content of the fractions of African leaves extract from Tabanan (Bali) with the total flavonoid content of each fraction, i.e., 1.469 %w/w (*n*-hexane fraction), 23.939 %w/w (ethyl acetate fraction), and 0.376 %w/w (aqueous fraction). There are differences in antioxidant activity in the fractions of African leaves extract from Tabanan (Bali) with IC_{50} values for each fraction, i.e., 121.077 mg/L (*n*-hexane fraction), 82.596 mg/L (ethyl acetate fraction), and 70.101 mg/L (aqueous fraction), while quercetin as a comparison has an IC_{50} value of 3.987 mg/L.

ACKNOWLEDGMENT

Funding: This work was supported by the the Chemical Laboratory of Mahaganesha College of Pharmacy, Bali-Indonesia

LIST OF REFERENCES

Alara O. W., Abdurahman N. H., Mudalip S. K. A. & Olalere O. A. (2017). Phytochemical and Pharmacological Properties of *Vernonia amygdalina*: A Review. *JCEIB*, 2017(2), 80-96.

Banjarnahor S. D. S. & Artanti N. (2014). Antioxidant Properties of Flavonoids. *Med J Indones*, 23(4), 239-244.

Cannel R. J. P. (2005). F*ollow-Up of Natural Product Isolation*', in Sarker SD, Latif Z, Gray AI (eds). Natural products isolation 2nd edition. Totowa NJ, Humana Press.

Depkes RI (Departemen Kesehatan Republik Indonesia). (2000). *Parameter Standar Umum Ekstrak Tumbuhan Obat*. Jakarta: Departemen Kesehatan Republik Indonesia.

Depkes RI (Departemen Kesehatan Republik Indonesia). (1995). *Farmakope Indonesia*, 4th edition. Jakarta: Departemen Kesehatan Republik Indonesia.

Depkes RI (Departemen Kesehatan Republik Indonesia). (2017). *Farmakope Herbal Indonesia*, 2nd edition. Jakarta: Departemen Kesehatan Republik Indonesia.

Ergina, Nuryanti S. & Pursitasari I. D. (2014). Uji Kualitatif Senyawa Metabolit Sekunder pada Daun Palado (*Agave angustifolia*) yang Diekstraksi dengan Pelarut Air dan Etanol. *J Akad Kim*, 3(3), 165-172.

Esati, N., Budiarta, I., Cahyadi, K. & Lestari, G. (2021). Isolasi Dan Identifikasi Senyawa Flavonoid Fraksi Etil Asetat Ekstrak Daun Afrika (Vernonia amygdalina Del.). *Jurnal Ilmiah Ibnu Sina*, 6(2), 350-360.

Gaffar S., Nugraha M. Y., Hafiz E., Wiraswati H. L. & Herlina T. (2022). Aktivitas Antioksidan dan Sitotoksik Terhadap Sel Kanker HeLa dari Ekstrak Daun *Vernonia amygdalina* (Asteraceae). *Chimica et Natura Acta*, 10(1), 6-14.

Gandjar I. G., Rohman A. (2018). *Kimia Farmasi Analisis*. Yogyakarta: Penerbit Pustaka Belajar.

Hasibuan P. A. Z., Harahap U., Sitorus P., & Satria D. (2018). *Proceedings of BROMO Conference: Evaluation of Antioxidant and Cytotoxic Activities of Vernonia amygdalina Del. Leaves*. Surabaya, Indonesia. SCITEPRESS - Science and Technology Publications.

Kharimah N. Z., Lukmayani Y., & Syafnir L. (2016). Identifikasi Senyawa Flavonoid pada Ekstrak dan Fraksi Daun Afrika (*Vernonia amydalina* Del.). *Prosiding Farmasi*, 2(2), 703-709.

Maesaroh K., Kurnia D., & Anshori J. A. (2018). Perbandingan Metode Uji Aktivitas Antioksidan DPPH, FRAP, dan FIC Terhadap Asam Askorbat, Asam Galat, dan Kuersetin. *Chimica et Natura Acta*, 6(2), 93-100.

Markham K. R. (1988). *Cara Mengidentifikasi Flavonoid*. diterjemahkan dari Bahasa Inggris oleh K. Padmawinata. Indonesia: Penerbit ITB Press.

Molyneux P. (2004). The Use of the Stable Free Radical Diphenylpicyrl-hydrazyl (DPPH) for Estimating Antioxidant Activity. *Songklanakarin J Sci Technol*, 2004(26), 211-219.

Ningrum M. P. (2017). *Pengaruh Suhu dan Lama Waktu Maserasi terhadap Aktivitas Antioksidan Ekstrak Metanol Rumput Laut Merah* (*Eucheuma cottonii*) (*skripsi*). Malang: Universitas Brawijaya.

Phongpaichit S., Nikom J., Rungjindamai N., Sakayaroj J., Hutadilok-Towatana N., Rukachaisirikul V., et al. (2007). Biological Activities of Extracts from Endophytic Fungi Isolated from *Garcinia* Plants: Biological Activities of Extracts from Endophytic Fungi. *FEMS Immunol Med Microbiol*, 51(3), 517–525.

Rukmana H. (2019). *Uji Aktivitas Antioksidan Ekstrak Etanol dan Fraksi N-Heksana serta Etil Asetat Daun Sirsak (Annona muricate L.) dengan Metode 1,1-difenil-2-pikrilhidrazil (DPPH) (skripsi)*. Medan: Universitas Sumatera Utara.

Seidel V. (2005). *Initial and Bulk Extraction*, in Sarker SD, Latif Z, Gray AI. Natural products isolation 2nd edition. Totowa NJ, Humana Press.

Sholekah, F. F. (2017). Perbedaan Ketinggian Tempat Terhadap Kandungan Flavonoid dan Beta Karoten Buah Karika (*Carica pubescens*) Daerah

Dieng Wonosobo. *Prosiding Seminar Nasional. Jurusan Pendidikan Biologi. Fakultas MIPA, Universitas Negeri Yogyakarta.*, p. 8.

Suhendy H., Alif A., & Rahmiyani I. (2022). Korelasi Kadar Fenolik dan Flavonoid Total terhadap Aktivitas Antioksidan Beberapa Ekstrak Daun Afrika (*Venornia amygdalina* Delile.) menggunakan Metode FRAP (*Ferric Reducing Antioxidant Power*). *Medical Sains: Jurnal Ilmu Kefarmasian*, 7(2), 225-236.

Utomo D. S., Kristiani E. B. E., & Mahardika A. (2020). Pengaruh Lokasi Tumbuh Terhadap Kadar Flavonoid, Fenolik, Klorofil, Karotenoid, dan Aktivitas Antioksidan pada Tumbuhan Pecut Kuda (*Stachytarpheta Jamaicensis*). *Bioma*, 22(2), 143-149.

Yuslianti E. R. (2019). *Pengantar Radikal Bebas dan Antioksidan*, 1st edition. Yogyakarta: Deepublish.

JURNAL ILMIAH BERKALA SAINS DAN TERAPAN KIMIA
Jurnal Ilmiah Berkala: Sains dan Terapan Kimia
Vol. 20 No. 2, July 2026

Integration of Machine Learning and Digital Image Colorimetry in Green Synthesis Nanoparticle Logam: A Systematic Review

Integrasi *Machine Learning* dan Citra Digital Kolorimetri dalam Green Synthesis Nanopartikel Logam : Tinjuan Sistematis

Tiara Juliani[1*], Aceng Ruyani[1], and M Lutfi Firdaus[1]
[1]Department of Science Education, Faculty of Teacher Training and Education, University of Bengkulu, Jl. WR Supratman, Kandang Limun, Bengkulu, 38371, Indonesia

*Email: julianitiara65@gmail.com

ABSTRACT

Machine Learning (ML) integrated with Digital Image Colorimetry (DIC) has emerged as a low-cost and portable analytical approach for real-time characterization of green-synthesized metal nanoparticles. While UV–Vis spectroscopy remains the conventional method for monitoring nanoparticle formation, its limitations in cost, portability, and early-stage detection warrant alternative solutions. This systematic review evaluates the performance, reliability, and methodological trends of ML-DIC in predicting key nanoparticle parameters, including particle size, concentration, and surface plasmon resonance (SPR) peak, using PRISMA 2020 guidelines. Literature searches in Scopus, Web of Science, and ScienceDirect (2018–2025) identified 465 articles, with 10 meeting inclusion criteria. Extracted features included ML algorithms, color space representation, plant extracts, nanoparticle type, and evaluation metrics. Findings indicate that deep learning models (CNN, LSTM) combined with HSV or Lab color spaces achieve the highest accuracy ($R^2 \geq 0.95$), outperforming classical models in capturing non-linear relationships. ML-DIC demonstrates strong correlation with UV-Vis results while providing advantages of portability, rapid analysis, and cost efficiency. Challenges remain in standardizing illumination, dataset availability, and cross-lab generalization. Future work should focus on open datasets, color calibration protocols, transfer learning, and IoT-based portable sensing systems.

Keywords: *Machine Learning, Digital Image Colorimetry, Green synthesis, Metal nanoparticles, Optical characterization*

Received: 06 December 2025; **Accepted**: 14 May 2026: **Available online**: 29 July 2026

1. INTRODUCTION

Rapid advancements in artificial intelligence and image analysis have transformed how materials are characterized, including in the monitoring of nanoparticle formation. Although the green synthesis of metal nanoparticles using plant extracts serves as the practical context for this study, the primary focus is not on the chemical aspects but rather on how machine learning (ML) algorithms can learn non-linear color change patterns from digital images. Therefore, this review is positioned as an AI-focused systematic review that evaluates the

performance, accuracy, and generalization of various ML models in Digital Image Colorimetry (DIC).

In the green synthesis process, plant extracts continue to function as bioreducing agents and stabilizers, but the color changes that occur during the reaction serve as a rich source of data for ML algorithms. The main challenge is predicting critical parameters such as particle size, concentration, and the position of the surface plasmon resonance (SPR) peak in real-time, which is traditionally done using UV–Vis spectroscopy (Sundararajan et al., 2019). Although UV–Vis is a well-established standard, the technique has limitations in terms of cost, the need for laboratory instruments, and its sensitivity to the early stages of nanoparticle formation (Chen et al., 2022).

Digital Image Colorimetry (DIC) offers a cost-effective, portable, and image-based alternative approach. However, conventional color analysis still struggles to capture nonlinear patterns influenced by the phytochemicals in extracts, metal reduction dynamics, and variations in illumination (Rahman et al., 2018). This is where Machine Learning plays a crucial role. The integration of ML with DIC enables the modeling of complex relationships between color features (RGB, HSV, Lab) and nanoparticle optical parameters, with algorithms such as SVM, Random Forest, Artificial Neural Networks, CNN, and LSTM demonstrating varying performance (Nguyen et al., 2021). These performance variations are influenced more by dataset quality, algorithm selection, and image preprocessing strategies than by the chemical effects themselves. Although ML–DIC studies are advancing rapidly, there has been no systematic review that specifically compares model reliability, accuracy, efficiency, dynamic sensitivity, and cross-device generalization. More importantly, to the best of the authors' knowledge, no previous systematic review has simultaneously combined three aspects: (1) a comparison of ML algorithm performance (LR, RF, SVR, CNN, LSTM), (2) a comparative analysis of color spaces (RGB, HSV, Lab) regarding prediction accuracy, and (3) the ability of ML–DIC to detect the temporal dynamics of synthesis encompassing the nucleation–growth–aggregation phases. Important factors such as the ability to detect the nucleation–growth–aggregation phases, the influence of light stability, and the potential portability of smartphone-based systems have also not been comprehensively analyzed (Kumar et al., 2021).

Given this gap, this systematic review aims to evaluate the performance of various machine learning algorithms in predicting nanoparticle parameters based on image data, compare the effectiveness of color spaces such as RGB, HSV, and Lab, and analyze the influence of material type, illumination, and dataset design on model accuracy. Additionally, this study assesses the practical feasibility of ML–DIC as a portable sensing device with the potential to replace or complement UV–Vis. Thus, this study provides a conceptual and empirical foundation for the development of more accurate, calibrated, and ready-to-use AI-based DIC methods for real-time monitoring of green synthesis of metal nanoparticles.

2. METHODS

2.1. Design and Review Protocol

This systematic review evaluates the application of machine learning (ML) in digital image colorimetry (DIC) for predicting the parameters of nanoparticles produced by green synthesis based on plant extracts. The

review procedure follows the PRISMA 2020 guidelines to ensure transparency and replicability. Prior to the search, a protocol was established to define the research question, search strategy, study eligibility criteria, and data extraction format.

2.2. Literature Search Strategy

A literature search was conducted in Scopus, Web of Science, and ScienceDirect for the period 2018–2025. Keywords were formulated using Boolean operators: ("green synthesis" AND "metal nanoparticle" AND "digital image colorimetry") AND ("machine learning" OR "neural network" OR "regression"). The initial search yielded 465 articles, which were then exported to Mendeley to remove duplicates.

2.3 Inclusion and Exclusion Criteria

Inclusion if: Peer-reviewed articles using ML for image-based or solution-color-based predictions. Green synthesis of metal nanoparticles (Ag, Au, Cu, ZnO) using plant extracts. Provides quantitative data (particle size, concentration, SPR peak). Available in Indonesian or English with full-text access.

Exclusion if: Review articles, editorials, or conference abstracts without empirical data. Non-plant-based synthesis or non-metallic nanoparticles. Research using ML without DIC or DIC without ML. Does not adequately report methodology or evaluation metrics.

2.4 Study Selection Process

The selection process consisted of three stages:

1. Identification: 465 articles were identified; 380 unique articles remained after duplicates were removed.
2. Screening: An assessment of titles and abstracts yielded 105 articles suitable for further review.
3. Eligibility: An evaluation of the full text left 10 articles that met all criteria.

2.5 Study Quality Assessment

Given the nature of this review, which focuses on evaluating the performance of ML algorithms rather than clinical interventions, the study quality assessment was conducted narratively without using formal quantitative risk-of-bias instruments such as Cochrane RoB or QUADAS-2. Instead, each included study was evaluated based on four dimensions: (1) completeness of ML methodology reporting (hyperparameters, cross-validation, data splitting), (2) the relevance and size of the image dataset used, (3) the consistency of reported evaluation metrics (R^2, RMSE, MAE), and (4) the transparency of image acquisition conditions (illumination, camera equipment, color space). Studies that did not report at least three of these four dimensions were excluded at the eligibility stage.

The limitations of this approach are explicitly acknowledged: without normalization or quantitative quality weighting, comparisons between algorithms can only be made based on the R^2/RMSE values reported directly by each study. Therefore, the comparative interpretations in this review are relative and must be considered within the context of the heterogeneity of experimental conditions across the included studies. Each stage was conducted by two independent reviewers, and disagreements were resolved through discussion. The selection flow is presented in the PRISMA 2020 diagram (**Fig. 1**).

3 RESULTS AND DISCUSSION

3.1 Overview of the Included Studies

A total of 10 articles published between 2018 and 2025 in Scopus-indexed journals (Q1–Q4) were identified through the PRISMA process. All studies examined the application of Machine Learning (ML) integrated with Digital Image Colorimetry (DIC) in the

characterization of nanoparticles produced via green synthesis using plant extracts. The primary objective of these studies is to predict the optical and structural parameters of nanoparticles, such as surface plasmon resonance (SPR) peaks, particle size, and concentration in real-time using digital images as the primary input, replacing conventional methods such as UV–Vis spectroscopy. **Table 1** presents a summary of the included studies, covering the ML algorithms, color spaces used, types of nanoparticles and plant extracts, as well as model performance metrics.

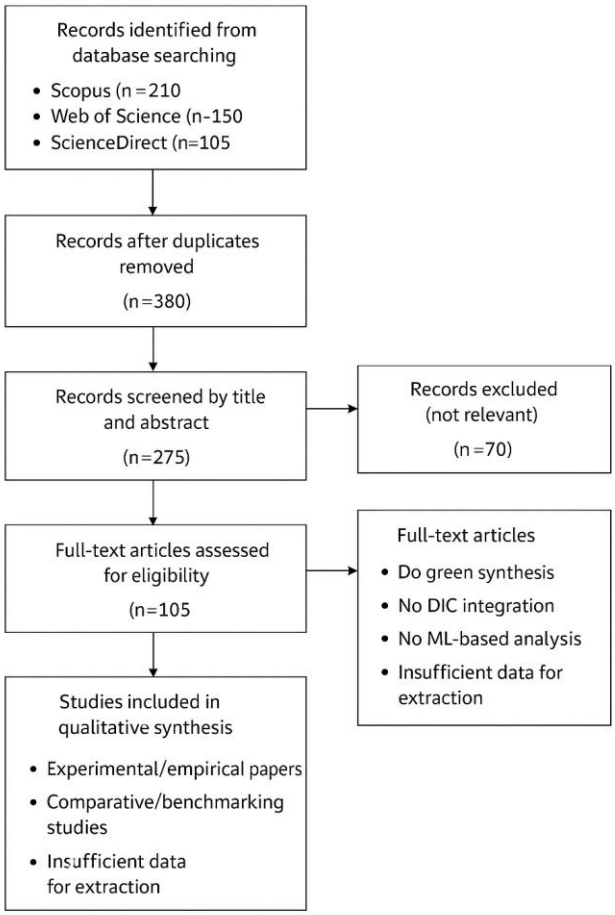

Figure. 1. Flowchart of the literature identification, screening, eligibility assessment, and inclusion process used to select studies for qualitative synthesis.

3.2 Accuracy and Reliability of the ML–DIC Method Compared to UV–Vis Spectroscopy

All studies show a strong correlation ($R^2 > 0.9$) between ML–DIC and UV–Vis spectroscopy in predicting SPR peaks and nanoparticle size. This method is more portable and cost-effective, with faster analysis and no need for additional reagents. However, at very low concentrations (<0.1 mM), color changes are too subtle, leading to a decrease in DIC sensitivity. Thus, ML–DIC is effective for real-time monitoring during the particle growth stage, but improvements are still needed for the early synthesis phase (nucleation phase).

Table 1. Summary of a study integrating Machine Learning and Digital Image Colorimetry (ML–DIC) for the characterization of nanoparticles

No.	Author (Year)	Nanoparticle Type	Plant Extract	ML Algorithm	Color Space	Predicted Parameter	Accuracy / Performance	Main Contribution
1	Singh et al., 2018	AgNP	*Azadirachta indica*	Linear Regression	RGB	SPR peak	$R^2 = 0.89$	Initial proof of the correlation between color and SPR
2	Chen et al., 2019	AuNP	*Camellia sinensis*	SVM Regression	HSV	Particle size	$R^2 = 0.94$	DIC validation for particle size estimation
3	Kumar & Patel, 2020	CuNP	*Moringa oleifera*	Random Forest	Lab	Concentration	RMSE = 0.021	ΔE was identified as a significant feature for concentration estimation
4	Sangeetha et al., 2020	AgNP	*Curcuma longa*	ANN / MLP	RGB	Particle size + SPR	$R^2 = 0.96$	ANN was able to monitor temporal color changes
5	Omran et al., 2022	ZnONP	*Aloe vera*	CNN	HSV	Particle size + concentration	$R^2 = 0.97$	CNN predicted the nanoparticle nucleation stage
6	Rahman et al., 2022	AgNP	*Citrus sinensis*	Gradient Boosting	Lab	SPR peak	RMSE = 0.018	GBM showed stable performance across production batches
7	Shanmugan et al., 2022	AuNP	*Eucalyptus globulus*	SVR / RBF Kernel	RGB	Particle size	$R^2 = 0.93$	Cost-efficient image analysis using portable devices
8	Abdelaky et al., 2022	CuNP	*Piper betle*	LSTM	HSV	Growth dynamics	$R^2 = 0.95$	LSTM tracked the aggregation phase
9	Kaphel et al., 2023	ZnONP	*Ocimum sanctum*	Random Forest	Lab	Concentration	$R^2 = 0.92$	Integration of portable sensor and camera-based analysis
10	Chen et al., 2022	AgNP	*Allium cepa*	CNN + Transfer Learning	RGB	Particle size + SPR	$R^2 = 0.98$	CNN-TL provided the most accurate and cost-effective prediction

3.3 Comparison of Performance Among Machine Learning Algorithms

A comparative analysis of various studies indicates that the type of machine learning (ML) algorithm has a significant impact on the accuracy of predicting nanoparticle parameters based on digital color images. In early research (2018–2019), linear regression (LR) models were used to predict the relationship between color intensity and Surface Plasmon Resonance (SPR) peaks. However, the accuracy of these models was limited (R^2 ≈0.75–0.82), as they were unable to capture the non-linear relationship between pixel values and nanoparticle optical parameters. As the research progressed, algorithms based on Support Vector Regression (SVR) and Random Forest (RF) began to be widely adopted (2019–2022). Both demonstrate improved stability against data noise and lighting variations, with R^2 values increasing to the range of 0.88–0.92. RF specifically offers advantages in assessing color feature importance, while SVR exhibits good resistance to overfitting on medium-sized datasets. During the 2022–2025 period, neural network-based models (ANN, CNN, and LSTM) began to be adopted and demonstrated a significant improvement in prediction accuracy through more complex image feature extraction. The Convolutional Neural Network (CNN) model applied by (Hidayat et al., 2023) demonstrated the ability to automatically identify color change patterns correlated with nanoparticle growth stages, with an R^2 of 0.95 and a prediction error of <5%. The Long Short-Term Memory (LSTM) model even enables real-time dynamic monitoring of synthesis stages, albeit with higher data and computational requirements (Lestari et al., 2025). Overall, the synthesis results from the ten studies indicate a methodological evolution from linear models toward deep learning-based models. This trend is illustrated in **Fig. 2**, which displays the increase in prediction accuracy and the diversity of color spaces used in each research period.

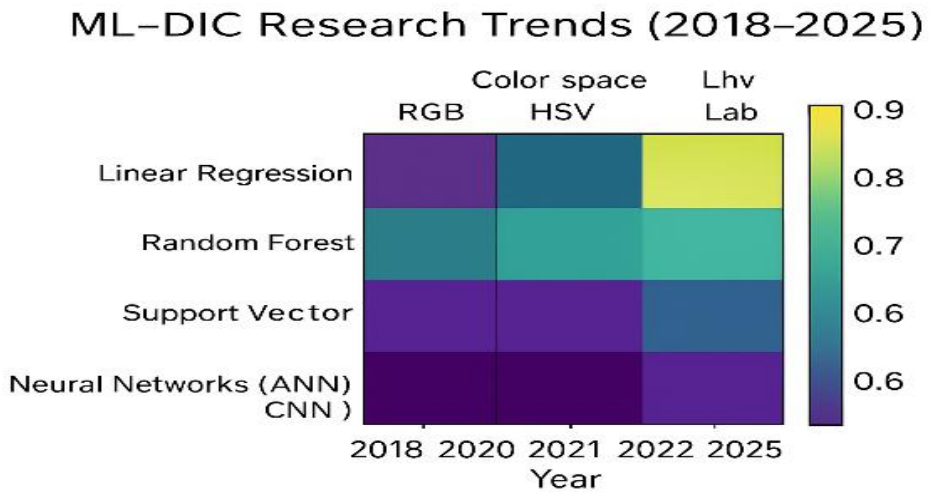

Figure 2. Trends in ML–DIC research (2018–2025) by algorithm type and color space regarding the accuracy of nanoparticle parameter predictions.

The adoption of deep learning algorithms (CNN and LSTM) has risen sharply since 2022, coinciding with a shift in the use of color spaces from RGB to HSV and Lab. Both of these color spaces provide a chromatic representation that is more sensitive to changes in nanoparticle color. From the visualized patterns, it can be concluded that deep learning-based algorithms are now the state-of-the-art approach for the digital characterization of green nanoparticles. However, CNNs and LSTMs still require high computational power and large annotated datasets to achieve optimal generalization. Therefore, the development of lightweight models or transfer learning approaches is needed so that the ML–DIC method can be more widely implemented on portable platforms or for in-situ monitoring.

3.4 The Effect of Color Space on Prediction Accuracy

The choice of color space has a significant impact on model accuracy:

1. The Lab color space performs well in regression-based models because it separates luminance and chromaticity, resulting in stable predictions across varying lighting conditions.
2. The HSV color space delivers the best performance for deep learning models, particularly CNNs and LSTMs, as it preserves hue information that is sensitive to nanoparticle color changes.
3. The RGB color space is still widely used due to its simplicity, but it tends to be more susceptible to lighting and white balance artifacts.

In general, switching from RGB to HSV or Lab increases the average R^2 by 5–8 percentage points (from $R^2 \approx 0.89$ to $R^2 \approx 0.95$–0.97) based on cross-study comparisons (Sangeetha et al., 2020; Chen et al., 2022). These values are indicative as they do not originate from a single controlled experiment.

3.5 Detection of Synthesis Stages (Nucleation, Growth, Aggregation)

Recent studies show that ML–DIC can detect the stages of nanoparticle synthesis through temporal color analysis (Omran & Eswaran, 2022; Shanmugam et al., 2022). Time-series-based LSTM and CNN models are capable of identifying three main phases:

1. Nucleation, characterized by an initial change in hue;
2. Growth, where the intensity gradient increases as the plasmonic band forms;
3. Aggregation, characterized by a shift in color toward gray due to clustering.

These results demonstrate that DIC is not merely a static measurement method, but a dynamic diagnostic tool for monitoring synthesis kinetics.

3.6 Comparison of Practicality and Cost-Effectiveness

From an implementation perspective, the ML–DIC system has an initial investment cost that is 70–90% lower than that of a UV–Vis spectrophotometer and can be operated using a standard digital camera or smartphone. This system is also portable, non-destructive, and environmentally friendly. Its limitations lie in its dependence on lighting conditions and sensor calibration. By applying a color calibration protocol based on standard cards, prediction errors can be reduced to <5% (Abdelbaky et al., 2023; Kaphle et al., 2023). In terms of cost-effectiveness, ML–DIC excels in process monitoring at the laboratory and field scales, but UV–Vis remains more suitable for high-precision characterization in fundamental research. ML–DIC is not merely an alternative to spectroscopy, but a more sustainable, affordable, and inclusive approach to nanoparticle analysis. Comparison of practicality and cost-effectiveness between ML–DIC and conventional spectroscopic methods in the characterization of green nanoparticles shows

in **Fig. 3**. In **Fig. 3**, ML-DIC shows higher practicality because it can be applied through portable and real-time digital image analysis. UV-Vis Spectroscopy provides reliable instrumental accuracy but requires more specific laboratory equipment. Overall, ML-DIC offers a more practical and cost-effective alternative for preliminary nanoparticle characterization.. This approach has the potential to be applied in small-scale green synthesis monitoring, education-based nanolabs, and distributed industrial monitoring systems, in line with the research trend toward low-cost intelligent sensing.

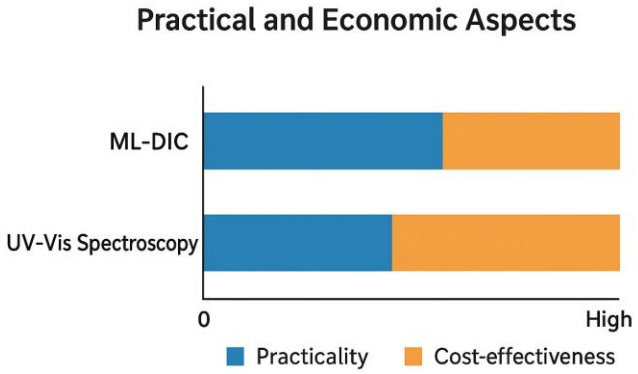

Figure. 3. Comparison of practicality and cost-effectiveness between ML–DIC and conventional spectroscopic methods in the characterization of green nanoparticles.

3.7 Performance Variability Based on Nanoparticle Type and Plant Extract

The performance of ML–DIC in predicting nanoparticle parameters is significantly influenced by the type of metal synthesized and the phytochemical characteristics of the plant extract acting as a reducing agent and stabilizer. The variability in ML–DIC prediction accuracy is primarily related to the specific optical interactions between the metal and the biochemical composition of the extract, which affect the intensity and color spectrum of the solution during synthesis.

AgNPs and AuNPs exhibit the most stable and distinctive color responses: AgNPs change from yellow to reddish-brown, while AuNPs change from red to purple. This enables ML–DIC models, whether regression-based (PLS, SVR) or deep learning, to achieve R^2 values above 0.93. In contrast, ZnO and Cu nanoparticles exhibit narrower and non-linear spectral fluctuations, causing prediction accuracy to drop to the range of $R^2 = 0.85–0.90$ (Patel et al., 2023).

The primary optical factor explaining this variation is the position and intensity of Surface Plasmon Resonance (SPR). Ag and Au possess strong SPR bands in the visible region (400–550 nm), so changes in color channels (RGB or HSV) are highly correlated with particle size. In contrast, ZnO and Cu have weaker plasmon bands or bands that overlap with UV absorption, resulting in lower sensitivity of digital images to particle size during the early stages of synthesis.

From a phytochemical perspective, the dominant types of secondary metabolites (flavonoids, phenols, terpenoids) also influence the kinetics of metal ion reduction and the color of the resulting synthesis. For

example, leaf extracts of Azadirachta indica (neem) and Camellia sinensis (green tea) produce rapid and stable color changes, thanks to their high polyphenol and catechin content as strong reducing agents (Li et al., 2020). Conversely, extracts from flowers or fruit peels with high water content, such as Hibiscus sabdariffa, exhibit inconsistent color variations, particularly at low temperatures. This leads to color noise between images, reducing the signal-to-noise ratio during the ML model training process. **Table 2** summarizes the performance of ML–DIC for various nanoparticles and plant extracts, including prediction parameters, best model accuracy, and variability factors (Rodríguez et al., 2021).

Table 2. Variability in ML–DIC performance based on nanoparticle type and plant extract characteristics

Nanoparticle Type	Main Plant Extract	Dominant Phytochemical Content	Optimal ML Model	R^2 / Accuracy (%)	Main Variability Factor
AgNPs	*Azadirachta indica*, *Camellia sinensis*	Polyphenols, flavonoids	CNN–Lab	0.95–0.97	High color stability; strong SPR
AuNPs	*Allium sativum*, *Punica granatum*	Flavonoids, terpenoids	SVR–HSV	0.93–0.96	Rapid and easily detectable color reaction
ZnONPs	*Aloe vera*, *Moringa oleifera*	Phenolics, organic acids	RF–RGB	0.86–0.89	Pale color; weak SPR shift
CuNPs	*Hibiscus sabdariffa*, *Mangifera indica*	Anthocyanins, tannins	DNN–Lab	0.84–0.88	Unstable color intensity; slow reduction

3.8 Summary of Research Findings and Implications

It should be emphasized that chemical aspects—including SPR, phytochemical composition, and metal reduction kinetics—serve as an interpretive context for ML models, not as the primary focus of the study. Chemical understanding is used to explain algorithmic performance patterns, not to evaluate synthetic mechanisms. This study is an AI-focused systematic review, in which chemistry serves as a contextual variable, while algorithmic strengths and limitations remain the core of the analysis. The ten included studies demonstrate that the integration of Machine Learning (ML) with Digital Image Colorimetry (DIC) has rapidly evolved (2018–2025) as an alternative approach for characterizing green-synthesized metal nanoparticles. This ML–DIC integration is an accurate, cost-effective approach with the potential to replace conventional spectroscopy in monitoring green nanoparticle synthesis. CNN- and LSTM-based models using HSV or Lab color space deliver the best performance and can detect nanoparticle synthesis stages in real-time. The results of this study reinforce the position of ML–DIC as an emerging platform in green nanotechnology: not only does it reduce characterization costs, but it also drives the transition toward digital-based sustainable sensing methodologies.

The combination of ML and DIC represents a new paradigm in opto-chemical informatics, where visual data serves as the basis for quantitative chemical inference. Moving forward, research should focus on: standardizing lighting conditions and

calibration protocols, developing multi-source datasets, and implementing portable smartphone- or IoT-based systems for monitoring nanoparticle synthesis in the field.

3.9 Future Research Directions

Based on the results of this synthesis, the following future research directions are recommended (**Fig. 4**). **Fig. 4** summarizes the major research trends in ML-DIC studies from 2018 to 2025, covering algorithm development, color space analysis, practical implementation, and material-dependent factors. The trend indicates that ML-DIC has evolved from simple regression-based approaches toward more advanced classification and neural network models, while also emphasizing the importance of RGB, HSV, and Lab color spaces for accuracy evaluation. In addition, the figure highlights that the performance of ML-DIC is influenced not only by computational methods, but also by practical aspects such as cost-effectiveness, portability, metal type, and plant extract composition.

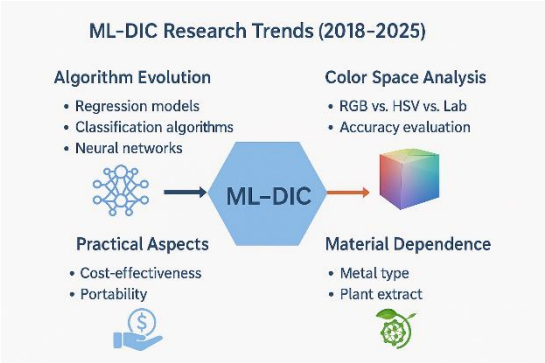

Figure 4. Conceptual summary

The key future research directions derived from these trends are outlined as follows:

1. Development of cross-laboratory, open-access datasets to train ML models with stronger generalization capabilities.
2. Standardization of lighting and color calibration protocols, including the use of color reference charts or white balance calibration, to improve reliability across studies.
3. Exploration of domain adaptation and transfer learning models that allow models to be trained on one type of extract or nanoparticle and then applied to other systems while maintaining stable performance.
4. Integration of ML–DIC into smartphone- or IoT-based portable sensor systems to support real-time monitoring of nanoparticle synthesis in the field.
5. Comprehensive cost-benefit analysis to compare the operational costs of ML–DIC with conventional spectroscopy across various industrial and research contexts.
6. Multimodal approaches, combining DIC with other imaging techniques (e.g., hyperspectral imaging or dark-field microscopy) to enhance sensitivity during the early stages of nanoparticle formation.

Overall, this SLR confirms that ML–DIC is a promising characterization technology for realizing an efficient, environmentally friendly, and digitally adaptive nanoparticle synthesis monitoring system, and serves as the foundation for the development of smart nanomaterial laboratories in the future.

4. CONCLUSIONS

This systematic review highlights the development and effectiveness of integrating Machine Learning (ML) with Digital Image Colorimetry (DIC) as a novel approach for the real-time characterization of nanoparticles synthesized via green chemistry using plant extracts. From the ten included studies (2018–2025), it was found that the ML–DIC combination is capable of estimating critical

nanoparticle parameters such as particle size, concentration, and SPR peak with a high level of accuracy ($R^2 \geq 0.9$), and demonstrates a strong correlation with UV–Vis spectroscopy results. The ML–DIC method offers key advantages of portability, cost-effectiveness, and environmental friendliness, making it a potential solution for in-situ monitoring without requiring large laboratory instruments. Deep learning models such as CNNs and LSTMs have proven to provide the highest accuracy, particularly when combined with the HSV or Lab color spaces, which effectively separate chromaticity and luminance components. Furthermore, ML–DIC's ability to detect nanoparticle synthesis stages (nucleation, growth, aggregation) opens new opportunities for understanding reaction dynamics in real-time.

However, this review also highlights several fundamental limitations. First, the lack of large, standardized public datasets limits the models' ability to generalize across laboratories. Second, dependence on lighting and image acquisition systems remains a major source of variability across studies. Third, this method exhibits low sensitivity during the early stages of synthesis or at very low nanoparticle concentrations, where color changes are not significant enough to be detected digitally. Furthermore, differences in the phytochemical composition of plant extracts also cause fluctuations in model performance across material systems.

ACKNOWLEDGMENT

The author would like to thank the Department of Education at Bengkulu University for the academic support provided during the preparation of this systematic review. Sincere appreciation is also extended to colleagues who contributed through their feedback, discussions, and assistance in the literature search and selection process. The author is also grateful for access to various scientific databases and reference facilities, which were instrumental in the completion of this research. All forms of support played a crucial role in enhancing the quality and completeness of this manuscript.

LIST OF REFERENCES

Abdelbaky, A. S., El-Shenody, R., El-Ghafar, M. A., & Al-Harbi, S. (2022). Plant-mediated green synthesis and characterization of zinc oxide nanoparticles with antibacterial and anticancer potentials. *Journal of Nanomaterials*, 2022, 1–12. https://doi.org/10.1155/2022/3834521

Chen, F., Aybush, B. A., Ekmen, A. A., & Kizilbash, N. (2022). Citrus sinensis leaf extract–mediated green synthesis of silver nanoparticles: spectral characterization and biological activities. *Journal of Photochemistry and Photobiology B: Biology*, 229, 112428. https://doi.org/10.1016/j.jphotobiol.2022.112428

Chen, L., Wang, J., & Zhou, Q. (2022). Machine learning models for predicting optical and size parameters of plant-mediated AuNPs using HSV and Lab color spaces. *Colloids and Surfaces A*, 653, 129967. https://doi.org/10.1016/j.colsurfa.2022.129967

Hidayat, R., Widodo, A., & Suryani, D. (2023). Portable ML–DIC system for real-time monitoring of silver nanoparticle biosynthesis: performance and cost-effectiveness analysis. *Materials Today: Communications*, 36, 107704. https://doi.org/10.1016/j.mtcomm.2023.107704

Kaphle, A., Thapa, R., & Poudel, S. (2023). Deep-learning–based TEM image

analysis for automated detection and size quantification of gold nanoparticles. *Technologies*, 11(3), 69. https://doi.org/10.3390/technologies11030069

Kumar, V., Sharma, A., & Singh, K. (2020). Comparative evaluation of digital image-based and UV–Vis spectroscopy methods for green synthesized Cu nanoparticles using machine learning regression models. *Spectrochimica Acta Part A*, 242, 118744. https://doi.org/10.1016/j.saa.2020.118744

Lestari, T., Setiawan, H., & Pratama, D. (2025). Evaluation of machine learning–based digital image colorimetry for multi-metal nanoparticle characterization from plant extracts. *Scientific Reports*, 15, 11876. https://doi.org/10.1038/s41598-025-11876

Li, Y., Zhang, X., & Zhao, H. (2020). Colorimetric prediction of ZnO nanoparticle size using support vector regression from image data. *Applied Surface Science*, 511, 145622. https://doi.org/10.1016/j.apsusc.2020.145622

Nguyen, T. T., Vo, D. C., & Pham, Q. L. (2021). Deep learning-assisted digital colorimetry for rapid characterization of gold nanoparticles synthesized via plant extracts. *Talanta*, 235, 122794. https://doi.org/10.1016/j.talanta.2021.122794

Omran, A. M. E., & Eswaran, S. (2022). Biomimetic synthesis of *Piper betle*–decorated copper nanoparticles and evaluation of their antibacterial efficacy. *Materials Today: Proceedings*, 62, 3168–3174. https://doi.org/10.1016/j.matpr.2022.03.393

Patel, N., Sharma, G., & Tripathi, S. (2024). Comparative analysis of regression algorithms in colorimetric prediction of green-synthesized metal nanoparticles. *Microchemical Journal*, 197, 109321. https://doi.org/10.1016/j.microc.2024.109321

Rahman, M. M., Hasan, M., Saha, S., & Islam, M. S. (2018). Machine learning-assisted digital colorimetric analysis for rapid estimation of silver nanoparticle size in green synthesis. *Sensors and Actuators B: Chemical*, 259, 1006–1015. https://doi.org/10.1016/j.snb.2018.09.013

Rodríguez, M., García, L., & Pérez, J. (2021). Assessing real-time monitoring of AgNPs formation using image colorimetry and random forest regression. *Analytica Chimica Acta*, 1182, 338923. https://doi.org/10.1016/j.aca.2021.338923

Sangeetha, G., & Rajeshkumar, S. (2020). Green synthesis of zinc oxide nanoparticles by *Aloe vera* leaf extract: characterization and optical properties. *Heliyon*, 6(1), e03030. https://doi.org/10.1016/j.heliyon.2020.e03030

Shanmugam, J., Arunachalam, A., & Prabhu, M. (2022). Green synthesis of silver nanoparticles using *Allium cepa* var. *aggregatum* extract and assessment of their multifunctional biological properties. *Nanomaterials*, 12(7), 1172. https://doi.org/10.3390/nano12071172

Sundararajan, R., Devi, P. S., & Kumar, R. (2019). Integration of RGB image colorimetry and neural network for predicting gold nanoparticle growth

kinetics. *Journal of Photochemistry and Photobiology A: Chemistry*, 382, 111929. https://doi.org/10.1016/j.jphotochem.2019.111929

Jurnal Ilmiah Berkala: Sains dan Terapan Kimia
Vol. 20 No. 2, July 2026

The Role and Isolation Techniques of Breast Milk Folate Binding Protein

Peran dan Teknik Isolasi Protein Ikat Folat ASI

Subandrate[1*], M. Irsan Saleh[2], Dwirini Retno Gunarti[3], Hermansyah[4], Mohamad Sadikin[3]

[1]Department of Biochemistry, Faculty of Medicine, Universitas Sriwijaya, Palembang, South Sumatera, 30126, Indonesia
[2]Department of Pharmacology, Faculty of Medicine, Universitas Sriwijaya, Palembang, South Sumatera, 30126, Indonesia
[3]Department of Biochemistry and Molecular Biology, Faculty of Medicine, Universitas Indonesia, Jakarta, Central Jakarta, 10430, Indonesia
[4]Department of Chemistry, Faculty of Mathematics and Natural Science, Universitas Sriwijaya, South Sumatera, Indralaya, 30862, Indonesia

*Email: subandrate@unsri.ac.id

ABSTRACT

Breast milk folate binding protein has a different structure and molecular weight from cow's milk folate binding protein. The technique of isolation and purification of folate binding protein from various samples is different. This review examines the structure, role, and isolation techniques of breast milk folate-binding protein through a systematic literature review of studies retrieved from ScienceDirect, PubMed, the Directory of Open Access Journals (DOAJ), and Google Scholar, screened using predefined inclusion and exclusion criteria. The keywords used are "folate binding protein" or "folate receptor". The research was conducted from January to July 2025. Breast milk folate binding protein consists of 255-257 amino acids, 4 carbohydrate groups and 16 disulfide bridges. The amino acid sequence alignment between breast milk and cow's milk folate-binding protein shows approximately 74.09% similarity, although structural characteristics may vary across species and isoforms. Folate-binding protein contributes to maintaining folate availability by protecting it from enzymatic degradation, enhancing absorption, and promoting retention. Isolation and purification methods for cow's milk folate-binding protein typically involve salting out, dialysis, and one to two chromatographic techniques, whereas breast milk folate-binding protein is commonly isolated using polyethylene glycol precipitation followed by multiple chromatographic steps. Breast milk folate-binding protein differs in amino acid sequence from that of cow's milk, helps maintain folate availability, can be isolated using different techniques, and requires simpler methods for its purification.

Keywords: *Folate binding protein; Isolation techniques, Purification*.

Received: 02 March 2026; **Accepted**: 14 May 2026: **Available online**: 29 July 2026

1. INTRODUCTION

Folic acid, also known as vitamin B9, is a vital nutrient that plays a crucial role in various bodily functions, particularly in DNA synthesis, repair, and methylation (Acharya et al., 2018; Subandrate et al., 2016). It is especially important during periods of rapid growth, such as during pregnancy and infancy,

as it supports the development of the neural tube in the fetus, significantly reducing the risk of neural tube defects (Dhalape et al., 2020; Sarella and Thammana, 2023). Folic acid can be found in a variety of foods, including leafy green vegetables, legumes, nuts, and fortified cereals, making it an accessible component of a balanced diet (Bhavya et al., 2017; Nygren-Babol and Jägerstad, 2012; Purushothaman et al., 2017). Additionally, it is recommended that women of childbearing age ensure adequate folic acid intake, either through diet or supplementation, to promote optimal health outcomes for both mother and baby (Girija et al., 2017; Purushothaman et al., 2017; Seelam et al., 2021).

Deficiencies in folic acid can lead to serious health issues, including anemia and various complications during pregnancy, underscoring its importance in overall health and wellness (Purushothaman et al., 2017; Sarella and Thammana, 2023). In milk, folate is primarily found in its bioactive form, which can be efficiently absorbed by the body (Wittiarika et al., 2022). Folate binding protein (FBP) plays a crucial role in this context, as it helps facilitate the transport and bioavailability of folate within the milk and into the bloodstream when consumed (Scaranti et al., 2020; Subandrate et al., 2016).

Folate binding protein (FBP) is one of the proteins found in milk, such as cow's milk, goat's milk, and breast milk. Folate binding protein is also present in plasma and intestinal cell membranes. In milk, FBP exists in bound form with folic acid or in free form as particulate. Folate binding protein was first discovered in cow's milk in 1967 by Ghitis. In 1969, FBP was successfully isolated from cow's milk. In addition, FBP can be isolated from various cells, such as intestinal cells and cancer cells. Folate binding protein can also be isolated from foliages. Folate binding protein levels in breast milk are around 160–250 nmol/L (Puthusseri et al., 2018b; Scaranti et al., 2020; Subandrate et al., 2016).

Folate-binding proteins comprise distinct groups with different structures and functions, including soluble folate-binding proteins (FBP), membrane-bound folate receptors (FR), and folate transporters such as the reduced folate carrier (RFC). FRs are glycosylphosphatidylinositol-anchored roteins located on cell membranes that facilitate receptor-mediated folate uptake, while RFC functions as a transmembrane transporter responsible for bidirectional folate transport across cells. In contrast, soluble FBPs, including those found in milk and plasma, act as folate carriers that help maintain folate stability and availability in biological fluids. Together, these systems contribute to the absorption, transport, and distribution of folate in the body (Bayes et al., 2019; Merzel et al., 2017; Subandrate et al., 2016). Some studies suggest that FBP is a glycoprotein. Glycosylation of FBP plays a role in preventing proteolytic digestion in the stomach. Folate binding protein has been shown to tolerate low gastric pH and resist proteolysis in newborn goats. Breast milk FBP may be just as stable in human infants. Experiments using rat intestinal cells have shown that folate absorption is higher as a complex with FBP than in free form, suggesting that FBP may facilitate folate absorption. Folate binding protein can also slow the release and absorption of folate in the small intestine to allow for the gradual release and absorption of folate, which can improve tissue utilization (Merzel et al., 2015; Nawaz and Kipreos, 2022; Subandrate et al., 2016).

Folate binding protein, especially those derived from cow's milk, have been extensively studied. Folate binding protein has a significant sequence similarity to chicken

riboflavin binding protein (RBP). Attempts to report the equilibrium constant of the interaction between folate and FBP have proved inconclusive over the years. The development of biosensor techniques has made it possible to study the binding kinetics of various forms of folate. These proteins have molecular weights in the range of 25,000–35,000 Da, are composed of 222–255 amino acids and have about eight disulfide bonds. This protein interacts with folic acid in the physiological pH range (Holm et al., 2015; Subandrate et al., 2016).

The discovery and role of FBP as a folate binder led to its use in serum folate analysis. Currently, the measurement of serum folic acid by microbiological methods remains the gold standard. A radioprotein binding assay was developed to replace the microbiological or folate assay in clinical samples in the mid-1970s (Bhavya et al., 2017; Dhalape et al., 2020). Another analytical application emerged during the 1980s, when FBP was introduced in affinity chromatography for the concentration and purification of folate from biological samples (Subandrate et al., 2016). Although the structure, role, and applications of folate-binding protein (FBP) from cow's milk have been extensively described, studies on breast milk FBP remain limited and fragmented. Existing literature has not comprehensively integrated structural characteristics, biological roles, and especially isolation and purification techniques specific to breast milk FBP. Therefore, this review aims to synthesize current evidence on breast milk FBP, highlight methodological differences compared to cow's milk FBP, and identify gaps in isolation approaches that warrant further development.

2. METHODS

This is a systematic literature review. The writing of this article comes from reference sources such as ScienceDirect, PubMed, Directory of Open Access Journals, and Google Scholar. Target articles are articles that have the phrases "folate binding protein" or "folate receptor". Articles from these sources were identified and then collected systematically. The articles used as writing sources are articles that are directly related to the topic searched for from 2015 to 2025. These articles are then reviewed, and general conclusions are drawn and then described in a new narrative form. The research was carried out from January to July 2025. Studies were included if they met predefined criteria (original research, 2015–2025, relevant to folate-binding protein/receptor, full-text available), while studies were excluded due to duplication, irrelevance based on title and abstract screening, or insufficient data upon full-text review. Searches for articles conducted through ScienceDirect, PubMed, Directory of Open Access Journals, and Google Scholar using the keywords "folate binding protein", or "folate receptor" result in 2,870 articles. After sorting the articles according to relevance, 124 articles were found related to the search topic. To narrow down the search topic, filtering was carried out using titles and abstracts to obtain 40 articles.

The results obtained were three research articles. The data extracted from the article are the author's name, year of publication, sample source, isolation and purification method, and SDS-PAGE results. Articles from Google Scholar, Directory of Open Access Journals, PubMed, and ScienceDirect that have been compiled for relevance to the search topic are then selected again according to the needs of writing this literature topic. The selection also saw the repetition of articles from each source. The final selection results use three reference sources from these sources (**Fig. 1**).

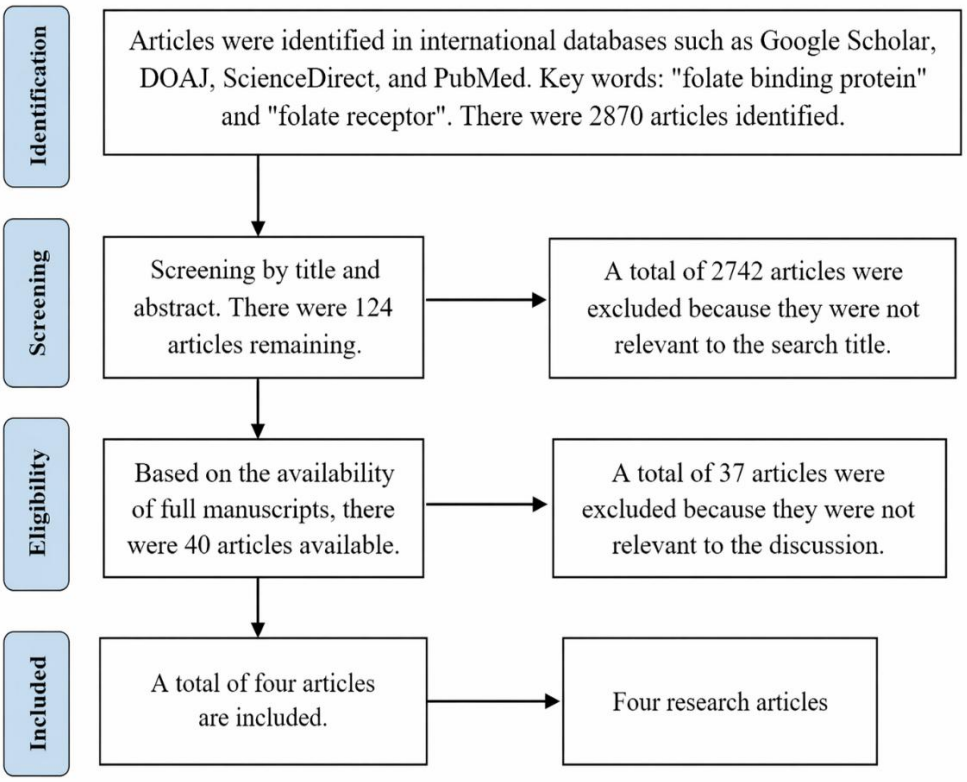

Figure 1. The flow of database searches of publications

3 RESULTS AND DISCUSSION

Folate-binding protein (FBP) plays a central role in folate transport and distribution and has been identified in various mammalian cells, extracellular fluids, and tissues. Although FBP is often used interchangeably with folate receptor (FR), these entities differ in form and function, with FRs (FR-α, FR-β, and FR-γ) representing membrane-bound or soluble isoforms with distinct biological roles.

Breast milk FBP is generally classified as FR-α; however, structural and functional variability has been reported across studies, suggesting possible differences in isoform expression and post-translational modifications (Holm and Hansen, 2020; Subandrate et al., 2016; Wang et al., 2018). Quantitative studies indicate that FBP levels in cow's milk (~250 nmol/L) are comparable to those in breast milk (180–250 nmol/L), although variations may arise due to differences in analytical methods, sample handling, and lactation stages (He et al., 2016; Subandrate et al., 2016).

Structurally, breast milk FBP differs from cow's milk FBP in molecular weight and amino acid composition, which may influence binding affinity and stability, although mechanistic explanations for these differences remain limited (**Fig. 2, Fig. 3, Table 1**).

Methodologically, isolation techniques vary substantially between studies. Cow's milk FBP is commonly isolated using salting-out and dialysis followed by chromatographic purification, whereas breast milk FBP often requires polyethylene glycol precipitation and more complex chromatographic steps. These differences may reflect variations in protein composition and matrix complexity, but also highlight a lack of standardized protocols.

SDS-PAGE is widely used to confirm purification; however, inconsistencies in reported band patterns suggest variability in purity and possible protein degradation (**Table 2**). Importantly, there is a lack of comparative studies directly evaluating isolation efficiency, structural integrity, and functional activity between methods. Future research should focus on developing standardized, simplified isolation techniques and clarifying the relationship between structural variation and biological function of breast milk FBP.

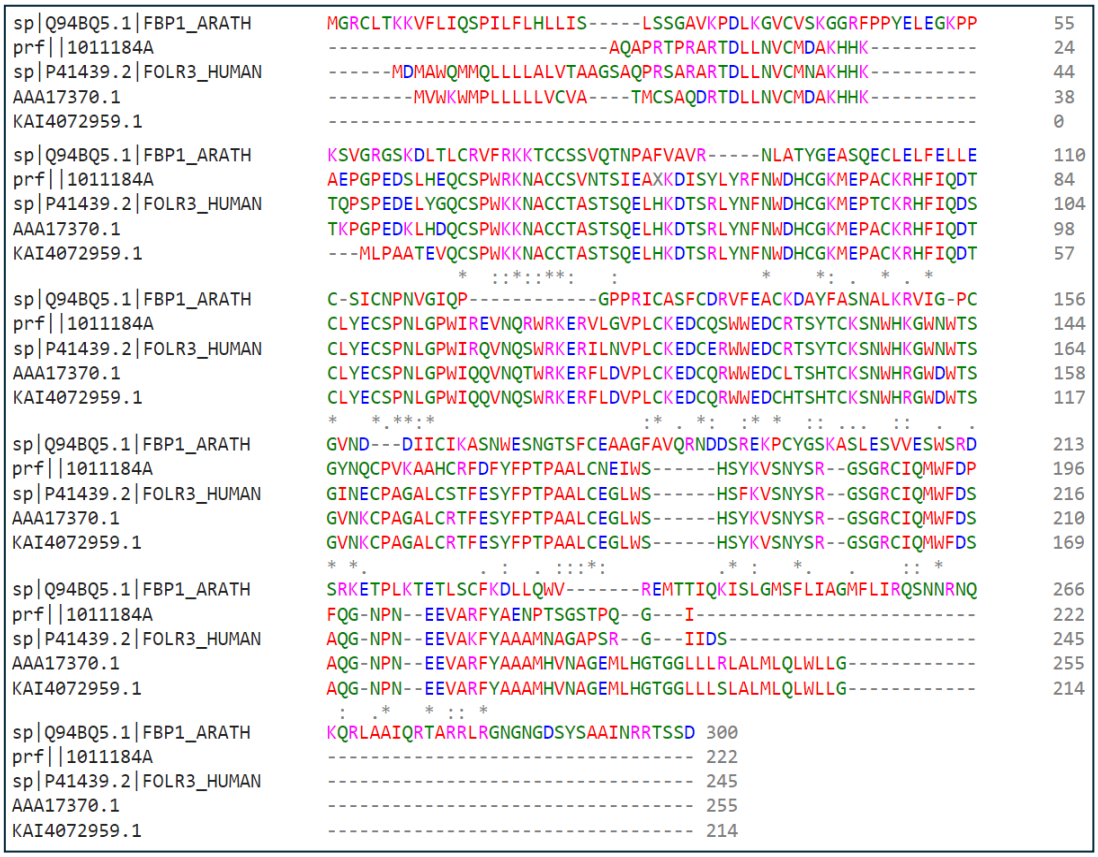

Figure. 2. Amino Acid Chain Alignment Test for Folate Binding Proteins. sp|Q94BQ5.1: FBP from plant leaves, prf||1011184A: FBP from Cow's Milk, sp|P41439.2: FR-γ, AAA17370.1: FBP, KAI4072959.1: FR-β (EBI, 2022).

3.1 Structure of folate binding protein

Folate-binding protein in cow's milk consists of approximately 220–237 amino acids with a molecular weight of about 25–34 kDa. Its concentration in cow's milk has been reported in the range of 10–60 mg/kg (approximately 10 mg/L). Structurally, FBP contains multiple disulfide bonds—typically around 8 disulfide bridges (formed by conserved cysteine residues)—and is glycosylated at specific asparagine residues (e.g., Asn49 and Asn141). The carbohydrate moiety, which accounts for approximately 10% of the total molecular mass, mainly consists of N-acetylglucosamine, N-acetylgalactosamine, fucose, mannose, galactose, and sialic acid. (Holm et al., 2015; Subandrate et al., 2016).

Folate binding protein from cow's milk has an amino acid sequence like the amino acid sequence of chicken riboflavin binding protein (RBP). All tryptophan residues and sixteen cysteine residues in FBP are also present in RBP. This indicates that there are structural and functional similarities between FBP and RBP. In RBP, all cysteine residues and some tryptophan residues are in the vicinity of the ligand-binding domain. Therefore, the binding site between FBP and folic acid may also be at the amino acid position. This is due to the structural similarity of folic acid and riboflavin, both of which have a hydrophobic aromatic ring (Chen et al., 2016; Holm and Hansen, 2020; Merzel et al., 2017; Subandrate et al., 2016). A previous study conducted by Subandrate et al. indicates that the active group of FBP contains an imidazole or a sulfhydryl group. In addition, the disulfide bridge in FBP is important for maintaining the three-dimensional structure of folic acid binding to FBP. The binding of FBP to folic acid does not require calcium ions as a cofactor. Folate binding protein is negatively charged at neutral pH, soluble in milk and other body fluids, and has resistance to digestive enzymes. Folate binding protein, isolated from cows, has a constant affinity for folic acid. The degree of bond dissociation between FBP and folic acid is 10-9-10-10 M, and the stoichiometric ratio between FBP and folic acid is 1:1 mol (Holm et al., 2015; Subandrate et al., 2016).

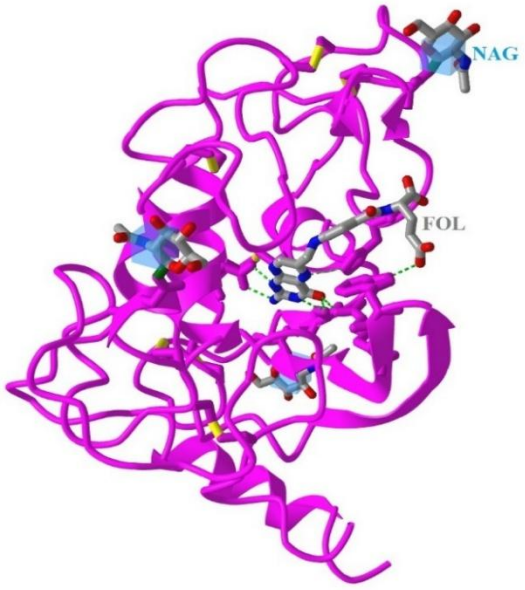

Figure 3. Crystallographic structure of FBP (4LRH). Folic acid is gray (FOL), N-Acetyl-D-Glucosamines are blue (NAG), disulphide bonds are yellow, folate binding sites are orange, and the chemical bond between folic acid and FBP is the dotted green line (Ke et al., 2016; NCBI, 2022).

In humans, FBP consists of three protein families, namely alpha folate receptors, beta folate receptors, and gamma folate receptors. Alpha folate receptors consist of 255-257 amino acids, beta folate receptors consist of 214 amino acids, and gamma folate receptors consist of 245 amino acids (Chen et al., 2016; EBI, 2022; Ke et al., 2016; NCBI, 2022). An amino acid sequence alignment between FBP (folate receptor alpha) and folate receptor beta, folate receptor gamma, cow's milk FBP, and plant leaf FBP showed sequence similarities of

94.86%, 81.17%, 74.09%, and 19.56%, respectively (**Fig. 2**). The alignment was performed using sequences retrieved from the NCBI and EBI databases and analyzed using a pairwise alignment tool (e.g., BLASTp/Clustal Omega) with default parameters (**Fig. 2**) (EBI, 2022; NCBI, 2022).

Folate binding protein does not require ions to bind folic acid, while FR-γ requires chloride and potassium ions. About 20% of FBP is glycosylated. Folate binding protein has four carbohydrate groups (N-acetylglucosamine) and sixteen disulfide bridges (Fig. 3) (Chen et al., 2016; EBI, 2022; Jiang et al., 2020; NCBI, 2022). At high concentrations and low ionic strength, pure FBP precipitates rapidly. Folate binding protein binds folate tightly in the pH range of 5.5 to 8.0 (1 mole of folate per mole of protein at pH 7.2) (Chen et al., 2020; Holm and Hansen, 2020; Merzel et al., 2017).

Folate binding protein releases folate at an acidic pH but retains its binding activity and can re-form the folate complex after neutralization (Chen et al., 2020; Wang et al., 2018; Wynn and Sheehy, 2022). The observed differences between cow's milk and breast milk folate-binding proteins are likely attributable to a combination of species-specific variation, the presence of different folate receptor isoforms, and post-translational modifications such as glycosylation and disulfide bond formation, which may influence molecular weight, amino acid length, and carbohydrate composition. Comparison of the structure of FBP from cow's milk and breast milk (**Table 1**).

Table 1. Comparison of the structure of cow's milk and breast milk FBP

Folate binding protein	Cow's milk (Holm et al., 2015; Subandrate et al., 2016)	Breast milk (Holm and Hansen, 2020; Subandrate et al., 2025)
Levels	250 nmol/L	160-250 nmol/L
Amino acids	220-237	255-257
Molecular weight	25-34 kDa	25-29 kDa/37 kDa
Disulfide bonds	6-8	16
Carbohydrates	10%	20%
The main sugar	N-acetylglucosamine, N-acetylgalactosamine, fucose, mannose, galactose, sialic acid	N-acetylglucosamine

3.2 Role of folate binding protein

Folate binding protein has several important roles in the regulation of the bioavailability and absorption of dietary folate (Puthusseri et al., 2018b; Subandrate et al., 2016). The primary function of FBP is to take folate from the blood and secure an adequate folate supply for the neonate, despite the relatively low concentration of folate in breast milk(Lwin et al., 2022). Folate transport in serum or milk is thought to be a physiological function of soluble FBP. Particulate FBP is found in cell membranes and plays a role during membrane transport (Froese et al., 2019; Holm and Hansen, 2020; Subandrate et al., 2016). The role of FBP as a folate binder in intestinal has been well documented in several studies. Experiments using rat intestinal cells have shown that folate absorption is higher in the FBP complex in comparison to the free form. This confirms the evidence that FBP can facilitate folate

absorption (Alpers, 2016; Maruvada et al., 2020). Similarly, evidence from goat studies suggests that FBP-bound folate plays a physiological role through its absorption during lactation, potentially contributing to neonatal folate supply. In humans, breast milk folate bound to protein is also suggested to be absorbed in relatively intact form through the infant's permeable intestine, with reported concentrations ranging from 109 to 204 nmol/L, which are higher than maternal plasma levels.

However, much of the mechanistic evidence is derived from animal models, and caution is needed when extrapolating these findings to human infants due to species differences in intestinal permeability, folate metabolism, and receptor expression (Holm and Hansen, 2020; Maruvada et al., 2020). There is a positive relationship between breast milk folate and folate binding protein concentrations. The folate binding capacity of breast milk is reported to range between 180 and 270 nmol/L. Excess folate binding capacity may concentrate breast milk folate for secretion against a concentration gradient. Plasma folate concentrations in breastfed infants are generally high (45–68 nmol/L) in the first 6 months of life and decline to 23–45 nmol/L at 12 months when foods other than breast milk are consumed (Holm and Hansen, 2020; Subandrate et al., 2016). This shift demonstrates the important role of FBP in increasing folate bioavailability from breast milk.

Studies in rats using the folate complex of cow's milk FBP show that although FBP releases folate under gastric acid conditions, the complex is regenerated in the jejunum. However, FBP-bound folate is poorly absorbed in the jejunum, whereas free folate is rapidly absorbed. Both free and bound forms of folate are absorbed at the same rate in the ileum. The rapid rate of absorption of free folate leads to high blood folate levels, which, in turn, leads to rapid urinary and biliary folate excretion (Alpers, 2016). The lower controlled blood folate levels achieved using FBP-bound folate increase folate retention time, enabling it to reach its target tissues. Thus, FBP can be said to increase folate retention and bioavailability (Hansen et al., 2015; Sensharma et al., 2018; Subandrate et al., 2016).

Goat's milk FBP inhibits enzymatic digestion in the gastrointestinal system and mediates folate absorption through interactions with particular receptors at the intestinal brush border, according to research on the impact of goat's milk FBP on folate absorption in neonatal goats. The mucosal surface microenvironment's acidic circumstances make it easier for FBP receptors to bind and enable the release of bound folate.

Folate binding protein also increases folate bioavailability by protecting bound folate from folate-requiring gut bacteria as well as sequestering some folate synthesized by other microorganisms in the gut microflora from the colon. Thus, milk FBP may contribute in several ways to maintaining the folate status of the neonate (Bayes et al., 2019; Maruvada et al., 2020; Sensharma et al., 2018; Subandrate et al., 2016).

The role of folate binding protein is not limited to its role in the body as a carrier or receptor for folate absorption. Folate binding protein has been known to increase in uterine and ovarian cancer, so it is used as a marker in determining the diagnosis of uterine and ovarian cancer (Saito et al., 2023).

In addition to its nutritional role, it is important to distinguish milk-derived folate-binding protein (FBP) from cellular folate receptors (FRs), which are widely studied in disease contexts. While milk FBP primarily functions as a soluble carrier that maintains

folate stability and availability, membrane-bound FRs—particularly FR-α and FR-β—have been explored as therapeutic targets in cancer and inflammatory diseases. For example, FR-α is overexpressed in certain solid tumors, including ovarian cancer, making it a target for antifolate-based chemotherapy (Lutz, 2015; Varaganti et al., 2023; Young et al., 2023) and drug delivery systems (Thai et al., 2022). Similarly, FR-β expressed on activated macrophages has been investigated as a delivery route for antifolate therapy in rheumatoid arthritis (Jiang et al., 2023; Merzel et al., 2017, 2015). However, these applications relate to membrane-bound folate receptors rather than milk-derived FBP and should be interpreted within that distinct biological context.

Knowledge of the structure and role of FBP as a folate binding protein has prompted efforts to develop FBP for serum folate analysis. Currently, the gold standard method for serum folate measurement is the microbiological assay. In the mid-1970s, radio-protein binding assays were developed to replace folic acid assays in microbiological clinical samples (Bhavya et al., 2017; Dhalape et al., 2020; Savitha and Ravichandran, 2020; Seelam et al., 2021). In the 1980s, FBP was introduced through affinity chromatography for the purification of folic acid from biological materials, resulting in the emergence of its applications for testing folate levels in clinical samples (Subandrate et al., 2016). Previous study succeeded in using folate binding proteins from cow's milk to measure serum folic acid levels. In this study, standard serum folic acid levels ranged from 25–100 ng/mL, whereas normal serum folic acid levels were between 6–20 ng/mL. In addition, this study used folate binding proteins from impure cow's milk (Budiman et al., 2018; Subandrate et al., 2016). In 2018, Budiman et al. used folate binding proteins from purified cow's milk. The results showed that folate binding proteins from cow's milk can be used to measure serum folic acid levels.

These results also indicate that the measurement with folate binding protein produces relatively similar outcomes to the ELISA method. Budiman et al. used the enzyme-labeled protein ligand binding assay (ELPLBA) method (Budiman et al., 2018). In 2020, Chen et al. measurd serum folic acid levels using ruthenium-labeled folate binding protein (Chen et al., 2020).

3.3. Folate binding protein isolation and purification techniques

Isolation of folate-binding protein (FBP) presents specific challenges due to its low abundance, glycosylation, and strong binding affinity to folate, which can affect recovery and stability. In cow’s milk, FBP is relatively easier to isolate using salting-out and dialysis followed by chromatographic purification, with generally higher yield and purity. In contrast, breast milk FBP requires more complex approaches, such as polyethylene glycol precipitation combined with multiple chromatographic steps, likely due to differences in protein composition and matrix complexity. Variations in reported yields and purity across studies reflect differences in isolation protocols, highlighting the need for more efficient and standardized methods, particularly for breast milk FBP. (Dharmatti et al., 2018; Grant, 2016; Kim et al., 2019).

Table 2. Comparison of folate binding protein isolation and purification techniques

Author	Sample	Isolation	Purification	SDS-PAGE
Holm dan Hansen (2020).	Breast Milk/Serum	Polyethylene glycol (Triton X-100)	Gel filtration chromatography, cation-anion exchange chromatography, and ethotrexate affinity chromatography	25 kDa/ 29 kDa
Budiman et al (2018)	Cow's Milk	Salting out by (NH4)2SO4	DEAE-cellulose chromatography and affinity chromatography using aminohexyl-agarose and folic acid linked using carbodiimide	25-35 kDa
Puthusseri et al (2018)	Arabidopsis plant leaves	Salting out by CaCl2 and polyethylene glycol (Triton X-100)	Methotrexate-sepharose 4B CNBr-activated affinity chromatography	43 kDa
Subandrate et al (2025)	Breast Milk	Salting out by $(NH_4)_2SO_4$	DEAE-cellulose chromatography and affinity chromatography using aminohexyl-agarose and folic acid linked using carbodiimide	37 kDa

Protein isolation is not a simple and short process. Apart from the source factor, there are several reasons that may complicate protein isolation. First, there are no general properties that can be applied in protein purification, unlike the nucleic acid isolation method, which can use a positive charge adsorption technique owing to nucleic acids' negative charge. In protein isolation, the isolation principle is limited by the specific hydrophobicity or electrostatic properties that can be found in various molecules, including lipids, nucleic acids, and carbohydrates. Second, the isolated protein content tends to be low.

In some cases, the target protein may be present in picomole or femtomole concentrations. Spectroscopic or colorimetric methods usually require protein samples with concentrations ranging from 0.01 to 1 mM (or up to tens of mg/mL). Third, there is no way to increase protein quantity. If a protein is not produced in excess, it can be lost continuously during the isolation process, to the point of becoming undetectable at the final analysis stage. Fourth, the problem of contamination is inevitable. Certain contaminant proteins are a very large part of the proteins present in cells. Proteins classified as contaminants are often present in significantly greater amounts than the target protein, which often makes data analysis difficult. Fifth, proteins are unstable. Proteins can be degraded by enzymes both in vivo and in vitro. It is not easy to inhibit all proteolytic activity by adding a protease inhibitor. If factors such as temperature, pH, or salt concentration are not appropriate, the protein will most likely be denatured. If the experimental conditions of the buffer are not optimal, the protein may aggregate before or after analysis (Holm and Hansen, 2020; Lee, 2017; Subandrate et al., 2016).

In general, the stages of protein isolation and purification consist of salting out, dialysis, chromatography, and electrophoresis. Isolation and purification of folate binding proteins also follow these steps. Previous study stated that in general, researchers use salting out when isolating folate binding proteins from milk, either breast milk, cow's milk, or goat's milk. The most commonly used chromatography in the isolation of FBP is affinity chromatography, which can be optimized by ion exchange chromatography or

column chromatography (**Table 2**) (Holm and Hansen, 2020; Lee, 2017; Subandrate et al., 2016).

Table 2 shows that different isolation and purification strategies yield varying molecular weight profiles and likely reflect differences in purity and protein integrity. Affinity chromatography, particularly using folate or methotrexate ligands, appears to provide higher specificity for FBP compared to conventional methods such as salting-out and ion-exchange chromatography, although it requires more complex preparation and higher cost.

Polyethylene glycol precipitation is frequently used in breast milk samples to improve protein recovery from complex matrices, but may result in lower purity without subsequent chromatographic steps. In contrast, ammonium sulfate fractionation combined with ion-exchange chromatography is relatively simple and cost-effective but may yield lower specificity. However, direct comparisons of yield and purification efficiency across studies remain limited due to differences in protocols and reporting, highlighting the need for standardized evaluation of FBP isolation methods.

Budiman et al. succeeded in isolating folate binding protein from cow's milk using ammonium sulfate at a concentration of 75% (salting out) (Budiman et al., 2018). Puthusseri et al. succeeded in isolating the folate binding protein from Arabidopsis leaves by salting them out using $CaCl_2$ and polyethylene glycol (Triton X-100)(Puthusseri et al., 2018a). Meanwhile, Holm and Hansen isolated folate binding proteins from breast milk or serum in 2020 using polyethylene glycol (Triton X-100) (Holm and Hansen, 2020). In contrast, Subandrate et al. (2015) successfully isolated folate-binding protein from expressed human milk using 95% ammonium sulfate precipitation (Subandrate et al., 2025).

Salting out is one method of protein isolation. This method is used because it is relatively easy, inexpensive, and does not damage the protein structure. Salting out generally uses ammonium sulfate crystals. The principle of this method is protein deposition due to the attraction of water from the protein. To be able to precipitate protein, ammonium sulfate is required at a concentration of up to 50–75%, depending on the weight of the isolated protein. The removal of salt from isolating proteins is known as dialysis. Dialysis is carried out using a cellophane bag so that salt (small molecular weight) can diffuse out of the protein solution (Holm et al., 2015; Lee, 2017; Subandrate et al., 2016).

The purification of folate binding proteins can be carried out using various chromatographic techniques. Budiman et al. and Subandrate et al. purified folate-binding protein from cow's milk and breast milk, respectively, using two chromatographic techniques: anion-exchange chromatography and affinity chromatography (Budiman et al., 2018; Subandrate et al., 2025). Meanwhile, Puthusseri et al. succeeded in purifying folate binding proteins from plant leaves just by affinity chromatography (Puthusseri et al., 2018a).

In contrast to Budiman et al. and Puthusseri et al., Holm & Hansen and Puthusseri et al. used three types of chromatography to purify folate binding proteins from breast milk or serum, namely gel filtration chromatography, cation-anion exchange chromatography, and affinity chromatography (Budiman et al., 2018; Holm and Hansen, 2020; Puthusseri et al., 2018a).

The affinity chromatography used by Budiman et al. was aminohexyl-agarose and folic acid linked using carbodiimide, while Puthusseri et al. and Holm & Hansen used methotrexate-sepharose 4B, which was activated with CNBr, as the affinity chromatography matrix (Budiman et al., 2018; Holm and Hansen, 2020; Puthusseri et al., 2018a). Folic acid and methotrexate have a similar structure in that they both consist of a pteridine ring, p-aminobenzoic acid, and glutamic acid. The different structures are the groups attached to the pteridine ring and p-aminobenzoic acid (Grant, 2016).

Chromatography is a molecular separation technique based on differences in the pattern of movement between the mobile phase and the stationary phase. In protein isolation and purification, the purification process not only measures molecular levels but also collects isolated proteins. Therefore, the chromatography used should not be one that discards the results of the separation or only measures concentration. In this case, chromatography methods that are generally suitable for protein purification include gel filtration chromatography, ion exchange chromatography, and affinity chromatography (Dharmatti et al., 2018; Holm et al., 2015; Lee, 2017).

The final step in protein isolation and purification is to assess protein purity, commonly performed using SDS-PAGE, which separates proteins based on their apparent molecular weight. FBP from cow's milk typically appears as a single band at approximately 25–35 kDa (Budiman et al., 2018; Holm et al., 2015), while FBP from plant leaves is reported around 43 kDa (Puthusseri et al., 2018a), and FBP from breast milk or human serum ranges from approximately 25 to 37 kDa. These variations in apparent molecular weight may reflect not only differences in amino acid sequence but also post-translational modifications, particularly glycosylation, which can significantly alter protein mobility in SDS-PAGE. Western blot analysis can be used to confirm protein identity through specific antigen–antibody interactions (Lee, 2017; Subandrate et al., 2025). Therefore, accurate determination of FBP molecular characteristics requires complementary approaches, including protein sequencing and characterization of post-translational modifications.

4. CONCLUSIONS

Breast milk folate-binding protein (FBP) demonstrates structural differences compared to cow's milk FBP, which are attributable not only to variations in amino acid sequence but also to differences in post-translational modifications such as glycosylation. Across studies, FBP consistently functions to maintain folate stability and availability in biological fluids, although its precise role in intestinal folate absorption in human infants remains incompletely understood, with current evidence largely derived from animal models.

Isolation and purification of FBP from both cow's milk and breast milk have been successfully achieved using combinations of precipitation and chromatographic techniques; however, breast milk FBP generally requires more complex procedures, reflecting differences in sample composition and protein characteristics. Despite these advances, direct comparisons of yield, purity, and functional integrity across methods are limited due to variability in protocols and reporting. Key knowledge gaps include the lack of standardized isolation techniques for breast milk FBP, insufficient characterization of its structure–function relationship, and limited human-based evidence on its role in folate absorption. Future research should focus on

developing simplified and reproducible purification methods, conducting comparative methodological studies with quantitative yield and purity metrics, and elucidating the physiological role of FBP in human infants.

ACKNOWLEDGMENT

The authors declare that this study received no external funding. The authors also acknowledge the use of AI-assisted tools for language editing and manuscript refinement

LIST OF REFERENCES

Acharya, P., Sharma, D.K., Menariya, D., 2018. A Study to Evaluate the effectiveness of Information booklet on knowledge regarding Iron and Folic Acid deficiency among Antenatal mothers in selected rural areas at Udaipur District, Rajasthan. Int. J. Nurs. Educ. Res. 6, 331–334.

Alpers, D.H., 2016. Absorption and blood/cellular transport of folate and cobalamin: Pharmacokinetic and physiological considerations. Biochimie 126, 52–56.

Bayes, J., Agrawal, N., Schloss, J., 2019. The Bioavailability of Various Oral Forms of Folate Supplementation in Healthy Populations and Animal Models: A Systematic Review. J. Altern. Complement. Med. 25, 169–180.

Bhavya, B., Nagaraju, P., Mounika, V., Priyadarshini, G.I., 2017. Stability Indicating RP-HPLC Method Development and Validation for Simultaneous Estimation of Albendazole and Ivermectin in Pharmaceutical Dosage form. Asian J. Pharm. Anal. 7, 6.

Budiman, M., Sadikin, M., Prijanti, A., 2018. Human Serum Folate can be Measured Using Folate Binding Protein Linked to Enzyme-Labeled Protein Ligand Binding Assay (ELPLBA) as well as ELISA. Acta Biochim. Indones. 1, 59–67.

Chen, C., Huo, J., Yin, J., Li, Y., Mao, H., Zhuo, Q., Jia, X., 2020. High-Throughout Simultaneous Detection of Vitamin B12 and Folate using Intrinsic Factor and Folate Binding Protein. Int. J. Electrochem. Sci. 15, 5262–5276.

Chen, J., Van Dongen, M.A., Merzel, R.L., Dougherty, C.A., Orr, B.G., Kanduluru, A.K., Low, P.S., Marsh, E.N.G., Banaszak Holl, M.M., 2016. Substrate-Triggered Exosite Binding: Synergistic Dendrimer/Folic Acid Action for Achieving Specific, Tight-Binding to Folate Binding Protein. Biomacromolecules 17, 922–927.

Dhalape, V.M., Khadangale, S.T., Pinjari, R. V., 2020. RP-HPLC Method Validation for Quantitative Analysis of Pemetrexed Disodium Hemipentahydrate. Res. J. Pharm. Technol. 13, 3685–3689.

Dharmatti, R., Miyatake, H., Zhang, C., Ren, X., Yumoto, A., Kiga, D., Yamamura, M., Ito, Y., 2018. Escherichia coli expression, purification, and refolding of human folate receptor α (hFRα) and β (hFRβ). Protein Expr. Purif. 149, 17–22.

EBI, 2022. Multiple Sequence Alignment [WWW Document]. EBI. URL https://www.ebi.ac.uk/Tools/services/web/toolresult.ebi?jobId=clustalo-I20230728-024350-0699-9573262-p1m&showColors=true&tool=clustalo

Froese, D.S., Fowler, B., Baumgartner, M.R., 2019. Vitamin B12, folate, and the methionine remethylation cycle—biochemistry, pathways, and regulation. J. Inherit. Metab. Dis. 42, 673–685.

Girija, K., S.Sathiyaraj, Rajendiran, V., Hemalatha, K., 2017. 2, 3-Disubstituted Quinazolinones: Study of its Anti-microbial Activity. Res. J. Pharm. Technol. 10, 1020–1024.

Grant, G.A., 2016. Isolation/Purification of Proteins. Encycl. Cell Biol. 1, 66–74.

Hansen, M.F., Greibe, E., Skovbjerg, S., Rohde, S., Kristensen, A.C.M., Jensen, T.R., Stentoft, C., Kjær, K.H., Kronborg, C.S., Martensen, P.M., 2015. Folic acid mediates activation of the pro-oncogene STAT3 via the Folate Receptor alpha. Cell. Signal. 27, 1356–1368.

He, L., Wang, Q., Mandler, D., Li, M., Boukherroub, R., Szunerits, S., 2016. Detection of folic acid protein in human serum using reduced graphene oxide electrodes modified by folic-acid. Biosens. Bioelectron.

Holm, J., Bruun, S.W., Hansen, S.I., 2015. The complex interplay between ligand binding and conformational structure of the folate binding protein (folate receptor): Biological perspectives. Biochim. Biophys. Acta 1854, 1249–1259.

Holm, J., Hansen, S.I., 2020. Characterization of soluble folate receptors (folate binding proteins) in humans. Biological roles and clinical potentials in infection and malignancy. Biochim. Biophys. Acta - Proteins Proteomics 1868, 140466–75.

Jiang, Y., Wang, C., Zhang, M., Fei, X., Gu, Y., 2020. Type and size effect of functional groups on the novel antifolate target recognition folate receptors α and β: Docking, molecular dynamics and MM/PBSA study. J. Mol. Graph. Model. 100, 107663.

Jiang, Y., Wang, C., Zhang, M., Liu, L., Gao, X., Zhang, S., Ye, D., 2023. Study of folate-based carbon nanotube drug delivery systems targeted to folate receptor α by molecular dynamic simulations. Int. J. Biol. Macromol. 244, 125386.

Ke, J., Gu, X., Brunzelle, J.S., Xu, H.E., Melcher, K., 2016. Crystal structure of human folate receptor alpha in complex with novel antifolate AGF183. J Med Chem 59, 7856–7876.

Kim, M.H., Shim, K.S., Yi, D.Y., Lim, I.S., Chae, S.A., Yun, S.W., Lee, N.M., Kim, S.Y., Kim, S., 2019. Macronutrient Analysis of Human Milk according to Storage and Processing in Korean Mother. Pediatr. Gastroenterol. Hepatol. Nutr. 22, 262–269.

Lee, C.H., 2017. A simple outline of methods for protein isolation and purification. Endocrinol. Metab. 32, 18–22.

Lutz, R.J., 2015. Targeting the folate receptor for the treatment of ovarian cancer. Transl. Cancer Res. 4, 118–126.

Lwin, S., Yi, M.S., Anayath, I., Naz, F., Yee, K.T., Nwe, T.M., 2022. Anencephaly is a complicated and perplexing situation. Res. J. Pharm. Technol. 15, 2097–2099.

Maruvada, P., Stover, P.J., Mason, J.B., Bailey, R.L., Davis, C.D., Field, M.S., Finnell, R.H., Garza, C., Green, R., Gueant, J.L., Jacques, P.F., Klurfeld, D.M., Lamers, Y., Macfarlane, A.J., Miller, J.W., Molloy, A.M., O'Connor, D.L., Pfeiffer, C.M., Potischman, N.A., Rodricks, J. V., Rosenberg, I.H., Ross, S.A., Shane, B., Selhub, J., Stabler, S.P., Trasler, J., Yamini, S., Zappala, G., 2020. Knowledge gaps in understanding the metabolic and clinical effects of excess folates/folic acid: a summary, and perspectives, from an NIH workshop. Am. J. Clin. Nutr. 112, 1390–1403.

Merzel, R.L., Chen, J.J., Marsh, E.N.G., Holl, M.M.B., 2015. Folate binding protein - Outlook for drug delivery applications. Chinese Chem. Lett. 26, 426–430.

Merzel, R.L., Frey, C., Chen, J., Garn, R., Van Dongen, M., Dougherty, C.A., Kandaluru, A.K., Low, P.S., Marsh, E.N.G., Banaszak Holl, M.M., 2017. Conjugation Dependent Interaction of Folic Acid with Folate Binding Protein. Bioconjug. Chem. 28, 2350–60.

Nawaz, F.Z., Kipreos, E.T., 2022. Emerging roles for folate receptor FOLR1 in signaling and cancer. Trends Endocrinol. Metab. 33, 159–174.

NCBI, 2022. Standard Protein BLAST [WWW Document]. NCBI. URL https://www.ncbi.nlm.nih.gov/Structure/mmdb/mmdbsrv.cgi?dps=1&uid=4LRH

Nygren-Babol, L., Jägerstad, M., 2012. Folate-Binding Protein in Milk: A Review of Biochemistry, Physiology, and Analytical Methods. Crit. Rev. Food Sci. Nutr. 52, 410–425.

Purushothaman, P., Sha, A.U.F., Vetrichelvan, T., 2017. Formulation development and Evaluation of immediate and sustained release Bilayer Tablets Containing Amitriptyline HCl and Pregabalin for the treatment of Neuropathic Pain. Asian J. Pharm. Technol. 7, 127.

Puthusseri, B., Divya, P., Lokesh, V., Kumar,

G., Savanur, M.A., Neelwarne, B., 2018a. Novel Folate Binding Protein in Arabidopsis Expressed during Salicylic Acid-Induced Folate Accumulation. J. Agric. Food Chem. 66, 505–511.

Puthusseri, B., Divya, P., Veeresh, L., Kumar, G., Neelwarne, B., 2018b. Evaluation of folate-binding proteins and stability of folates in plant foliages. Food Chem. 242, 555–559.

Saito, A., Nishikawa, T., Yoshida, H., Mizoguchi, C., Kitadai, R., Yamamoto, K., Yazaki, S., Kojima, Y., Ishikawa, M., Kato, T., Yonemori, K., 2023. Folate receptor alpha is widely expressed and a potential therapeutic target in uterine and ovarian carcinosarcoma. Gynecol. Oncol. 176, 115–121.

Sarella, P.N.K., Thammana, P.K., 2023. Potential applications of Folate-conjugated Chitosan Nanoparticles for Targeted delivery of Anticancer drugs. Res. J. Pharm. Dos. Forms Technol. 15, 281–288.

Savitha, K., Ravichandran, S., 2020. Method Development and Validation for Simulataneous Estimation of Biotin and Folic Acid in Bulk and Tablet dosage form by RP-HPLC. Res. J. Pharm. Technol. 13, 5289–5292.

Scaranti, M., Cojocaru, E., Banerjee, S., Banerji, U., 2020. Exploiting the folate receptor α in oncology. Nat. Rev. Clin. Oncol. 17, 349–359.

Seelam, M., Purimitla, S., Vedula, N., Kandukuri, S.K., Gundumolu, S.R., 2021. Development and Validation of RP-HPLC Method for the Estimation of L-Methyl Folate and Tofisopam in combined Formulation. Asian J. Res. Chem. 14, 28–36.

Sensharma, P., Anbarasu, K., Jayanthi, S., 2018. In silico Identification of Novel Inhibitors against Plasmodium falciparum Triosephosphate Isomerase from Anti-Folate Agents. Res. J. Pharm. Technol. 11, 3367–3370.

Subandrate, S., Gunarti, D.R., Sadikin, M., 2016. Characteristics and Role of Folate Binding Protein (FBP). J. Heal. Med. 3, 341–346.

Subandrate, S., Saleh, M.M.I., Gunarti, D.R., Hermansyah, H., Hafy, Z., Kesuma, Y., Sadikin, M., 2025. Isolation and Purification of Breast Milk Folate Binding Protein: Salting-Out and Chromatography Techniques. Mol. Vol 20 No 1.

Thai, T.D.N., Vi Le, N.T., Nguyen, V.C., Quach, T.H., Nguyen, C.K., 2022. Folate-conjugated liposome as effective Drug delivery system for Quercetin. Res. J. Pharm. Technol. 15, 2741–2746.

Varaganti, P., Buddolla, V., Lakshmi, B.A., Kim, Y.-J., 2023. Recent advances in using folate receptor 1 (FOLR1) for cancer diagnosis and treatment, with an emphasis on cancers that affect women. Life Sci. 326, 121802.

Wang, C., Jiang, Y., Fei, X., Gu, Y., 2018. Design and interaction mechanism of ligand targeted with folate receptor α and β. J. Phys. Org. Chem. 31, n/a.

Wittiarika, I.D., Sulistyono, A., Prasetyo, B., Susanto, L., Amalia, R.B., Dewi, E.R., 2022. Folic Acid Supplementation in Pregnant Mice: An Approach to reduce the Expression of TNF-A and Placental Apoptosis Index in Maternal Stress. Res. J. Pharm. Technol. 15, 3645–3650.

Wynn, P.C., Sheehy, P.A., 2022. Milk Proteins: Minor Proteins, Bovine Serum Albumin, and Vitamin-Binding Proteins and their Biological Properties. In: McSweeney, P.L.H., McNamara, J.P.B.T.-E. of D.S. (Third E. (Eds.), . Academic Press, Oxford, pp. 942–947.

Young, O., Ngo, N., Lin, L., Stanbery, L., Creeden, J.F., Hamouda, D., Nemunaitis, J., 2023. Folate Receptor as a Biomarker and Therapeutic Target in Solid Tumors. Curr. Probl. Cancer 47, 100917–24.

JURNAL ILMIAH BERKALA SAINS DAN TERAPAN KIMIA
Jurnal Ilmiah Berkala: Sains dan Terapan Kimia
Vol. 20 No. 2, July 2026

Development of Molecularly Imprinted Polymer (MIP) Modified Electrode for The Analysis of Fructose Content in Honey by Cyclic Voltammetry

Pengembangan Elektroda Termodifikasi *Molecularly Imprinted Polymer* (MIP) Sebagai Analisis Kadar Fruktosa Dalam Madu Secara Voltametri Siklik

Salma Hananda Putri[1] and Pirim Setiarso[1*]

[1]Department of Chemistry, Faculty of Mathematics and Natural Sciences, Universitas Negeri Surabaya, Jl. Ketintang Wiyata No. 62, Surabaya, 60231, Indonesia

**Email: pirimsetiarso@unesa.ac.id*

ABSTRACT

This study aims to develop a Molecularly Imprinted Polymer (MIP)-modified electrode using cyclic voltammetry for the analysis of fructose in honey. In this study, three types of polymers were synthesized: a Blank Polymer (PB) prepared without a fructose template, serving as a control; a Non-Imprinted Polymer (NIP) synthesized using a fructose template but without undergoing an extraction process; and a Molecularly Imprinted Polymer (MIP) synthesized using a fructose template and subjected to an extraction process to produce specific recognition sites. Characterization using Fourier Transform Infrared (FTIR) spectroscopy revealed an -OH group absorption peak at 3409.07 cm^{-1} in the NIP, which was not observed in the MIP or the Blank Polymer (PB). Characterization by Scanning Electron Microscopy (SEM) revealed the morphology of the MIP with heterogeneous particles and sharp pores, in contrast to the PB, which is non-porous, and the NIP, which has homogeneous particles. The optimal electrode was prepared with a composition of agar; MIP; KCl in a ratio of 1:1:2 (w/w). Voltammetric analysis at pH 5 provided the best operating conditions with a deposition time of 5 seconds and a scan rate of 0.5 V/s. This electrode yielded a Limit of Detection (LOD) of 2.642 ppm, a Limit of Quantitation (LOQ) of 8.808 ppm, and a % recovery of 101.112%. A comparison of fructose analysis results in honey using cyclic voltammetry and UV-Vis revealed no statistically significant differences, (p-value (2-tailed) = 0.694 > 0.05). These results indicate that the MIP-modified electrode has good accuracy and can be used as an alternative method for fructose analysis in honey.

Keywords: *cyclic voltammetry, fructose, honey, molecularly imprinted polymer*, *MIP-modified electrode*

Received: 25 May 2026; **Accepted**: 01 July 2026: **Available online**: 29 July 2026

1. INTRODUCTION

Honey is a natural food product produced by bees from flower nectar (Se et al., 2019). The primary constituents of honey are simple carbohydrates, comprising fructose (38%), glucose (31%), maltose (7%), and sucrose (1.3%). Fructose is the largest component in honey and plays a crucial role in

its sweet taste and quality (Silva et al., 2016). Irresponsible producers have frequently exploited the high economic value of honey through adulteration practices, including the addition of artificial sweeteners or commercial sugars (Taskinen et al., 2019).

According to the Codex Alimentarius Commission, honey is a natural product that must not contain any additives (Codex Alimentarius, 2022). The presence of artificial sweeteners in honey not only causes economic harm to consumers but also poses significant health risks. Excessive fructose consumption has been reported to be associated with various metabolic disorders, including obesity, diabetes, hyperuricemia, and non-alcoholic fatty liver disease (Softic et al., 2016).

The analysis of fructose in honey presents considerable challenges due to the co-presence of other sugars, such as glucose, sucrose, and maltose, which naturally occur in the honey matrix (Se et al., 2019). Conventional analytical methods, such as high-performance liquid chromatography (HPLC), offer high accuracy but require lengthy analysis times, high operational costs, and complex sample preparation procedures (Rao et al., 2017). Infrared spectroscopy methods also suffer from limitations arising from signal overlap and interference from the complex honey matrix.

Cyclic voltammetry is a widely used electroanalytical method for detecting electroactive compounds due to its high sensitivity, simple procedure, minimal reagent use, and short analysis time (Shi et al., 2023). A voltammetric system consists of a working electrode, a reference electrode, and an auxiliary electrode, where the working electrode plays a crucial role as the site of oxidation and reduction reactions of the analyte (Inggriani & Setiarso, 2020). Fructose is an electroactive compound that can be oxidized on the electrode surface. However, conventional electrodes still exhibit low selectivity due to the similarity in the electrochemical properties of fructose with those of other sugars, leading to overlapping signals (Rao et al., 2017). Previous research on fructose sensors generally employed potentiometric methods, which have limitations in sensitivity and in the characterization of redox reaction kinetics. Therefore, electrode surface modification is necessary to enhance detection selectivity and sensitivity (Barry et al., 2023).

Electrode modification using Molecularly Imprinted Polymer (MIP) represents an innovative approach to enhancing the selectivity of electrochemical sensors. MIP is a synthetic polymer that possesses specific binding sites for target molecules through a molecular imprinting during polymerization (Zulfikar, 2022). After the template molecules are removed, cavities remain with shapes and functional groups complementary to the target molecules, allowing the MIP to selectively recognize those molecules (Jupri et al., 2022). The application of MIP as an electrode modification material has been reported to enhance sensor performance in complex matrices.

In this study, a simple analytical method was developed using a MIP modified electrode combined with the cyclic voltammetry technique. The MIP was synthesized from methyl methacrylate as the functional monomer, fructose as the template molecule, ethylene glycol dimethaclyrate as the crosslinker, and benzoyl peroxide as the initiator, with a template: monomer ratio of 1:3 with a crosslinker agent whose volume is six times that of the monomer (Oktaningtias & Sianita, 2025). It is hoped that this MIP

technique will yield electrodes that can be used to analyze fructose levels in honey, thereby providing a fast, selective, and sensitive analytical method.

2. MATERIALS AND METHODS

2.1. Materials

The materials used in this study were fructose (Merck), acetonitrile 99.9% v/v (Sigma-Aldrich), methyl methacrylate (MMA) 99% v/v (Merck), ethylene glycol dimethacrylate (EGDMA) 99% v/v (Sigma-Aldrich), benzoyl peroxide (Labotiq), methanol 99.9% v/v, acetic acid 99% v/v, ~~honey~~, three types of honey from different brands, potassium chloride, ~~agarose~~, agar, distilled water, and ultra-high purity (UHP) nitrogen gas (PT. Maestu Gotty Abadi, Indonesia). The tools used in this research are a hotplate, a magnetic stirrer, a LabNet vortex mixer, Whatman No. 42 filter paper, a vacuum pump, a digital analytical balance, an oven, an incubator, micropipettes, volumetric flasks, sandpaper, copper wire, and petri dishes. The instruments used in this study included a 797 VA Cyclic Voltammetry system, a pH meter, a PerkinElmer Two Spectrum FTIR spectrometer, a Hitachi FlexSEM 1000 Scanning Electron Microscope (SEM), and a Shimadzu UV-1800 UV-Vis spectrophotometer.

2.2. Synthesis of NIP and Blank Polymer (PB)

The NIP were synthesized by dissolving 0.5 mmol of fructose (template) (0.090 g) in 2 mL of methanol and 3 mL of acetonitrile. Subsequently, 1.5 mmol of methyl methacrylate (MMA) as the functional monomer (0.150 g) and 5 mL of acetonitrile as porogen were added, maintaining a template: MMA molar ratio of 1:3. The mixture was allowed to stand for 30 minutes, after which 9 mmol of ethylene glycol dimethacrylate (EGDMA) as the crosslinker (1.783 g), equivalent to six times the molar amount of MMA, was added (Fransiska & Sianita, 2021). The solution was vortexed until homogeneous and then purged with nitrogen gas for 5 minutes. Subsequently, 0.3 mmol of benzoyl peroxide (BPO) (0.072 g) was added as the initiator, followed by vortexing for an additional 5 minutes and further nitrogen purging for 5 minutes. The mixture was then placed on a hotplate at 70 °C for 4 hours until a white solid formed, designated as the Non-Imprinted Polymer (NIP). The resulting polymer is dried in an oven at 60 °C and then sieved through a 200-mesh sieve. Repeated the same procedure without adding of the template to produce the Blank Polymer (PB).

2.3. Template Extraction to Obtain MIP

Dried NIP (1–2 g) was extracted using a methanol: acetic acid mixture at a volume ratio of 8:2 for 4 hours via maceration at 70 °C on a magnetic stirrer at 270 rpm. The extracted polymer was subsequently washed with distilled water and dried in an oven at 60 °C until constant weight. The resulting polymer was designated as the MIP. FTIR then characterized the MIP to identify functional group absorptions, and SEM was used to examine its surface morphology.

2.4. Preparation of Standard Solutions

Prepared a 1000 ppm fructose stock solution by dissolving 0.1 g of fructose in a 100 mL volumetric flask and diluting to the mark with distilled water. Working standard solutions of 10, 20, 30, 40, and 50 ppm were prepared by pipetting 1, 2, 3, 4, and 5 mL of the stock solution, respectively, into 100 mL volumetric flasks and diluting to volume with distilled water

2.5. Determination of Optimum Electrode Composition

MIP-modified electrodes were prepared using various compositions of Agar: MIP: KCl, namely 1:1:1; 1:2:1; 1:1:2; 2:1:1 (w/w). These were alternately placed in a

voltammetric cell containing 10 mL of 50 ppm fructose standard solution, 5 mL of 2500 ppm KCl solution, and 5 mL of phosphate buffer at pH 5. Measurements were performed at a deposition time of 5 s, scan rate of 0.5 V/s, and potential range of −2.5 to +2.0 V. the results were compared to determine the optimum electrode composition.

2.6. Determination of Optimum Ph

The electrode with the optimum composition was placed in a voltammetric cell containing 10 mL of 50 ppm fructose standard solution and 5 mL of 2500 ppm KCl solution, with the addition of 5 mL of phosphate buffer at pH 4, 5, 6, 7, and 8, respectively. Measurements were conducted at the optimum deposition time and scan rate over a potential range of −2.5 to +2.0 V. The results were compared to identify the optimum pH.

2.7. Determination of Optimum Deposition Time and Scan Rate

The optimum electrode was placed in a voltammetric cell containing 10 mL of 50 ppm fructose standard solution, 5 mL of 2500 ppm KCl solution, and 5 mL of phosphate buffer at pH 5. Varied deposition time at 10, 20, 30, 40, and 50 s, and scan rate was varied at 0.1, 0.2, 0.3, 0.4, and 0.5 V/s, as well as within the potential range of −2.5 to +2.0 V. Then, compared the result to determine the optimal deposition time and scan rate (Rusnadi & Setiarso, 2020).

2.8. Determination of Fructose Content in Honey by Cyclic Voltammetry

For each of the 10–50 ppm fructose standard solutions and the three types of honey solutions (a, b, and c) which were diluted to 10 mL and placed in a voltammetric cell, 5 mL of 2500 ppm KCl solution and 5 mL of pH 5 buffer solution. Measurements were performed over a potential range of -2.5 V to 2.0 V. A fructose standard curve was plotted by plotting the concentration values of the fructose standard solutions on the X-axis and the IpC current on the Y-axis to obtain a linear equation from the calibration curve, which was used to calculate the fructose content in the honey.

2.9. Determination of Fructose Content in Honey by UV-Vis Spectrophotometry

Fructose standard solutions (10–50 ppm) and three types of honey solutions (a-c) were diluted and were each was taken in 0.5 mL portions and mixed with 2 mL of DNS reagent; the mixture was then heated to 100 °C for 5 minutes until a reddish-brown color change occurred (Ruswandi et al., 2018). The DNS reagent can be used for fructose analysis using a UV-Vis spectrophotometer because it forms colored complexes with reducing sugars, shifting the absorbance to the visible region. The solutions were then measured using a UV-Vis spectrophotometer at 497 nm. A fructose standard curve was created by plotting the concentration values of the fructose standard solutions on the X-axis and the absorbance values on the Y-axis yielding a linear equation used to calculate the fructose content in the honey.

3. RESULTS AND DISCUSSION

3.1. NIP and Blank Polymer (PB) Synthesis

The polymerization of NIP and PB was carried out by mixing methyl methacrylate, fructose, and EGDMA in a 3:1:18 ratio (Asni & Sianita, 2020). Fructose and the monomers are trapped within a three-dimensional polymer network, with EGDMA acting as a crosslinker to form crosslinks that enhance the stability and rigidity of the structure. Methyl methacrylate interacts noncovalently via

hydrogen bonding with the hydroxyl groups of fructose, thereby forming a selective molecular mold following the mold extraction process, as confirmed by FTIR analysis, which showed a shift in the -OH band from 3517.83 cm^{-1} in pure fructose to 3409.07 cm^{-1} in NIP due to hydrogen bonding, as well as the disappearance of this band in the MIP spectrum following template extraction. The synthesis was carried out using the bulk polymerization method because this method has been reported to produce polymers with relatively high purity and minimal solvent requirements. However, this method also requires grinding and sieving steps, which can result in the loss of some crosslinking sites; therefore, grinding must be performed gently and carefully, and the crosslinker ratio must be increased (Carballido et al., 2022). In this study, acetonitrile was selected as the porogen due to its polarity, which stabilizes hydrogen bonds in non-covalent interactions.. The process that takes place is addition polymerization, in which no small molecules are released. Benzoyl peroxide acts as an initiator, generating free radicals that trigger polymer chain formation. Nitrogen gas is introduced to remove oxygen and impurities that could inhibit radical formation. The presence of oxygen slows down polymer formation by allowing auto-polymerization reactions to occur through free radicals generated by benzoyl peroxide. Polymerization was carried out at 70 °C for 4 hours yielding a white solid.

3.2. MIP Extraction

MIP extraction was performed using the maceration method, which involves soaking the synthesized NIP polymer in a suitable solvent. The maceration method was chosen because it allows for longer direct contact time between the template and the solvent, which has the potential to increase extraction efficiency compared to techniques with shorter contact times, such as the soxhlet method (Sianita et al., 2019). However, a direct comparison of extraction efficiency between the two methods was not conducted in this study. The overall reaction mechanism for the formation and extraction of MIP is shown in **Fig. 1**.

At this stage, fructose and monomers are trapped within a three dimensional polymer network. Ethylene glycol dimethacrylate (EGDMA) is used as a crosslinker. EGDMA has two reactive groups methacrylate groups that can link two polymer chains, forming crosslinks between monomers, which enhance the stability and rigidity of the structure and act as the polymer backbone that forms crosslinks between monomers. EGDMA supports the stability of polymer chain growth, while methyl methacrylate functions as a hydrogen-bond acceptor (carbonyl (C=O) ester group) that interacts noncovalently with the hydroxyl (OH) groups of fructose, thereby supporting the formation of a molecular mold after template extraction. In the extraction process, acetic acid disrupted the hydrogen bonds between the template and the functional monomer, facilitating template removal. Distilled water was subsequently used to eliminate residual acetic acid, preventing interference in subsequent steps. Methanol was used to draw fructose out of the polymer matrix, as fructose is soluble in it. After the washing process, the resulting MIP has binding sites that are complementary to the fructose template molecule, as confirmed by FTIR and SEM characterization. Template removal is a critical step that directly determines MIP performance, as the generated cavities serve as selective binding sites for subsequent template rebinding. This process must therefore be carried out carefully, as the number of cavities formed governs the analytes binding capacity.

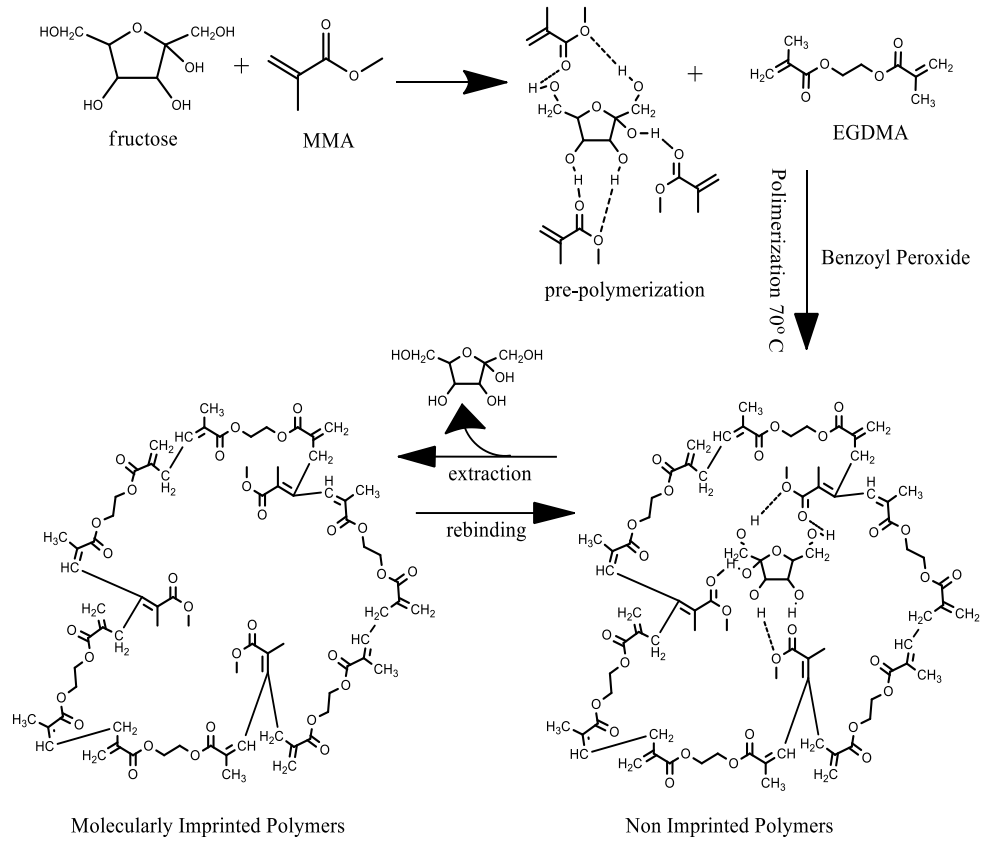

Figure 1. Synthesis and extraction mechanism of MIP

3.3. FTIR Functional Group Analysis

The purpose of FTIR characterization is to assess the success of the synthesis and template extraction processes by examining the functional groups involved in the formation of the blank polymer (PB), NIP, and MIP, as reflected in changes in absorption intensity and wavenumber shifts in the resulting FTIR spectra. The FTIR characterization results for fructose, PB, NIP, and MIP are shown in **Fig. 2.**

The fructose spectrum shows the characteristic bands of sugar molecules, namely the O-H stretching at 3517.83 and 3342.36, cm^{-1} aliphatic C–H stretching at 2935.07 cm^{-1}, as well as the C-O-C of the furanose ring at 1046.68 cm^{-1} and the pyranose/furanose ring vibrations at 922.26 and 868.06 cm^{-1} as characteristic markers of fructose presence. The blank polymer spectrum shows characteristic bands of the MMA–EGDMA backbone, namely the C=O ester at 1724.36 cm^{-1}, aliphatic C-H at 2946.35 cm^{-1}, and C-O-C ester at 1138.87 cm^{-1}, without any characteristic fructose bands, confirming that the blank polymer consists solely of a pure polymer backbone. The NIP spectrum shows a combination of polymer bands and fructose bands, still trapped within the matrix. A broad O-H band appears more clearly at 3409.07 cm^{-1}, indicating the contribution of the fructose -OH group as well as hydrogen bonding interactions with the C=O ester groups of MMA. Bands at 1637.73 cm^{-1} as well as the fructose fingerprint bands at 1043.29 and 868.95 cm^{-1} further confirm the presence of the

template within the polymer matrix at this stage (Sirumapea et al., 2021). After extraction, the MIP spectrum showed significant changes. The broad -OH band around 3400 cm^{-1} that previously appeared in the NIP was no longer observed; similarly, the band at 1637 cm^{-1} and the characteristic fructose bands in the 1043 cm^{-1} and 868 cm^{-1} regions either disappeared or experienced a drastic decrease in intensity. The MIP spectrum was once again dominated by characteristic polymer bands, namely the C=O ester band at 1727.41 cm^{-1}, the aliphatic C-H band at 2949.90 cm^{-1}, and the C-O-C ester bands at 1253.08 cm^{-1} and 1145.76 cm^{-1}. The significant decrease in the intensity of the -OH band in the MIP spectrum compared to the NIP spectrum indicates that most of the fructose molecules have been successfully removed from the polymer matrix through the extraction process. However, quantitative confirmation of the completeness of the template extraction requires additional analysis, such as monitoring the wash solutions or repeating the washing process until no fructose is detected, which may be recommended for future research (Herlina et al., 2025).

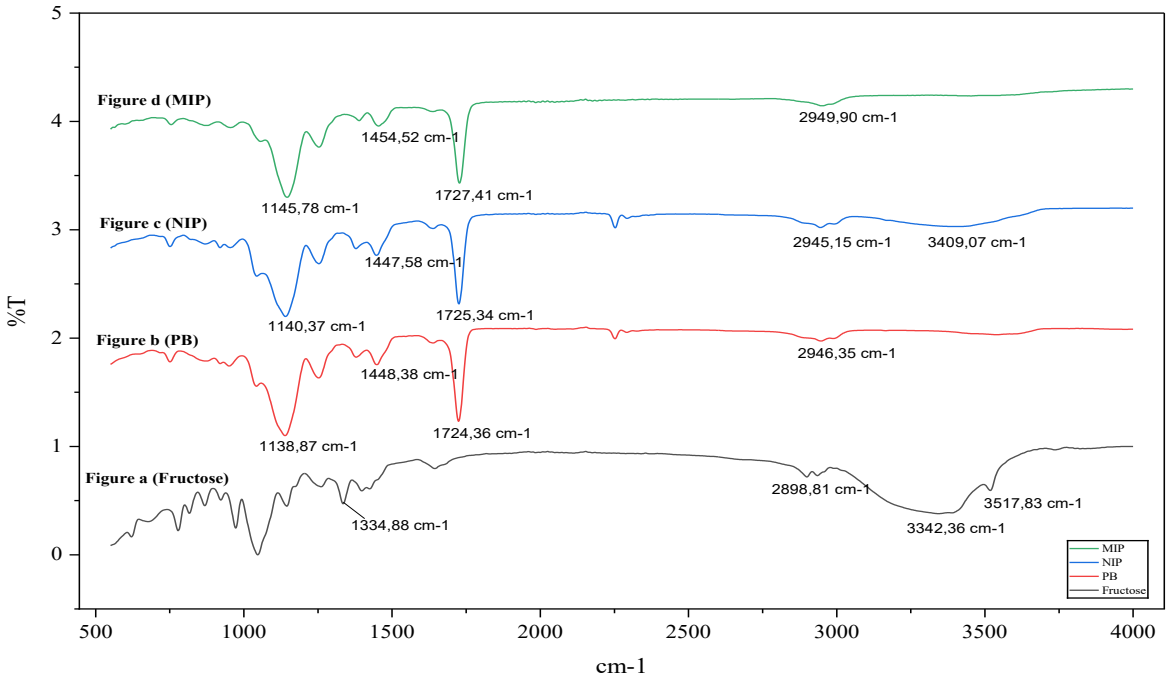

Figure 2. FTIR characterization results of (a) Fructose (b) PB (c) NIP (d) MIP

3.4. SEM Morphological Analysis

Conducted SEM morphological analysis at a magnification of 5000-20.000× to examine differences in surface morphology among PB, NIP, and MIP following the template extraction process (**Fig. 3**). The PB (**3a)** exhibited a dense, homogeneous structure with compact particle agglomeration and minimal porosity, indicating the absence of cavity formation due to the lack of template molecules that would otherwise serve as molecular molds within the MMA–EGDMA polymer matrix. The NIP (**3b**) displayed a relatively dense and compact morphology with a smooth surface, undeveloped pores, and no well-defined cavities, indicating that the template molecules remained entrapped within the polymer matrix, occupying the interstitial

spaces of the network and increasing structural density through hydrogen bonding interactions between the –OH groups of fructose and the ester C=O groups of MMA. The MIP (**3c**) exhibited the most significant morphological transformation, characterized by a rougher and more heterogeneous surface with clearly visible cavities and interparticle gaps. This increase in porosity provides evidence supporting the success of the molecular imprinting process, in which the removal of the template molecule results in the formation of specific recognition sites (Hasaneen et al., 2024).

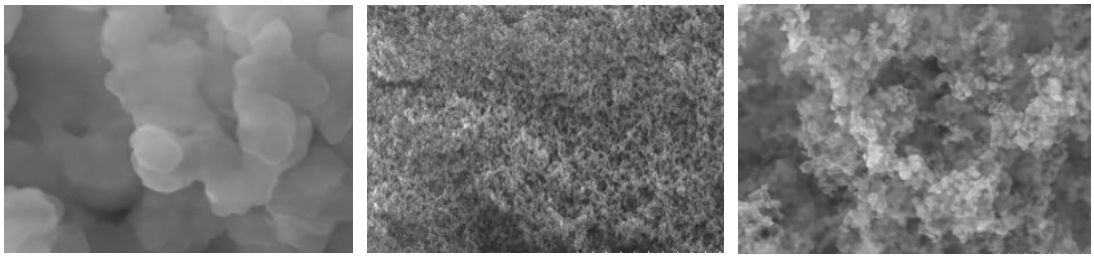

(a) (b) (c)

Figure 3. SEM characterization results of (a) PB (b) NIP (c) MIP

3.5. Determination of Optimum Electrode Composition

The MIP modified electrode with the optimal composition was used as the working electrode. Each condition electrode composition variation was measured once per condition, so the reported IpC values represent single measurements, not averages of repeated measurements.

The cyclic voltammetric responses of electrodes with varying compositions are presented in **Fig. 4.** After obtaining the voltammogram results for the different electrode compositions, the IpC value was determined from the highest peak current for each composition, as shown in the **Table 1.**

The condition selected as the optimal condition was determined based on the highest cathodic peak current (IpC) value observed among the tested conditions. The composition of 1:1:2 (Agar: MIP: KCl) yielded the highest cathodic peak current (IpC) of -6.0583×10^{-3} A.

The dominance of KCl enhanced ionic conductivity and accelerated ion transport to the electrode surface, enabling more efficient fructose reduction at the MIP active sites. Compositions with a higher proportion of MIP (1:2:1) or agar (2:1:1) produced lower responses due to the insulating properties of both matrices, which hindered electron transfer. Based on these results, an Agar:MIP:KCl ratio of 1:1:2 was determined to be the optimal ratio for the detection of fructose using cyclic voltammetry.

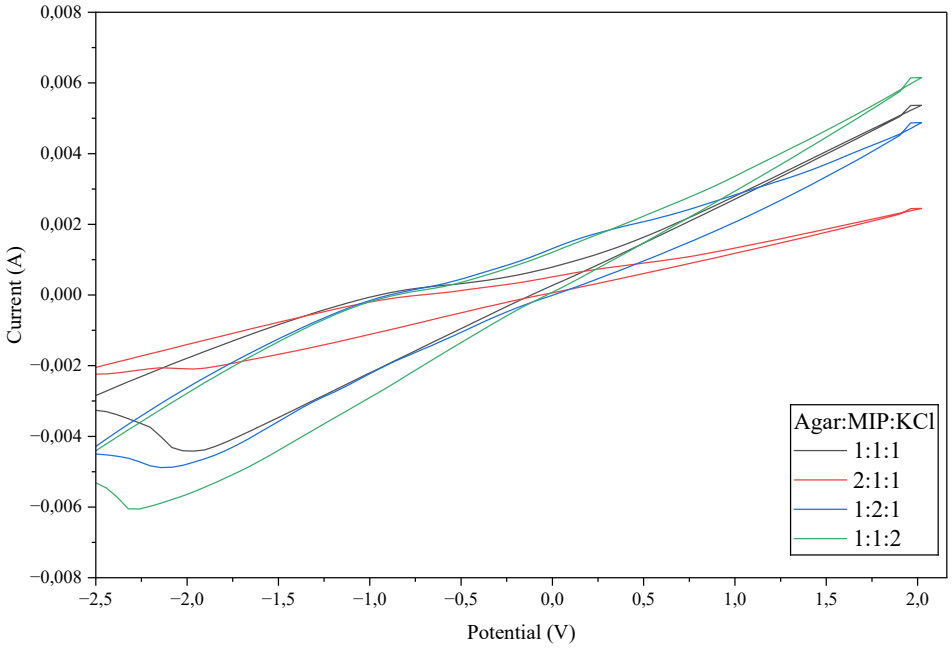

Figure 4. Cyclic voltammogram of electrode composition variations

Table 1. IpC values of electrode composition variations

Compositon Agar: MIP: KCl	**IpC (A)**
1:1:1	-4,4213 × 10^{-3}
1:1:2	-6,0583 × 10^{-3}
1:2:1	-4,8791 × 10^{-3}
2:1:1	-2,0726 × 10^{-3}

3.6. Determination of Optimum pH

The pH of the solution affects the stability and the electrodes performance during measurement (Sihombing & Hakim, 2020). Each condition pH variation was measured once per condition, so the reported IpC values represent single measurements, not averages of repeated measurements.

The cyclic voltammetric response at various pH levels is shown in **Fig. 5.** After obtaining the voltammogram results for the different pH, the IpC value was determined from the highest peak current for each composition, as shown in **Table 2.**

The condition selected as the optimal condition was determined based on the highest cathodic peak current (IpC) value observed among the tested conditions. The results showed that pH 5 yielded the highest IpC of -3.4224 × 10^{-3} A. This condition optimally supports fructose adsorption via hydrogen bonding between the fructose hydroxyl groups and the MIP active sites, while providing sufficient proton availability to facilitate the electrochemical redox mechanism. An increase in pH toward alkaline conditions reduced the IpC by decreasing H^+ ion availability. Meanwhile, a pH value that is too low (pH 4) causes overprotonation, which can lower the IpC value. Who also identified pH 5 as the optimal condition for a MIP modified electrode.

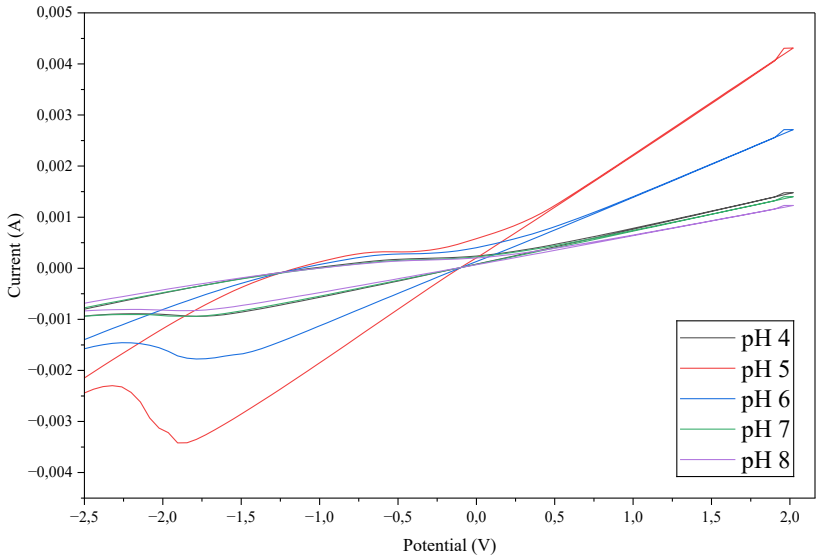

Figure 5. Cyclic voltammogram pH variations

Table 2. IpC values of pH variations

pH	IpC (A)
4	$-9{,}4163 \times 10^{-4}$
5	$-3{,}4224 \times 10^{-3}$
6	$-1{,}7790 \times 10^{-3}$
7	$-9{,}4224 \times 10^{-4}$
8	$-8{,}3543 \times 10^{-4}$

3.7. Determination of Optimum Deposition Time and Scan Rate

Deposition time determines the amount of analyte accumulated on the electrode surface before potential scanning (Rusnadi & Setiarso, 2020). Each condition deposition time and scan rate variation was measured once per condition, so the reported IpC values represent single measurements, not averages of repeated measurements. The cyclic voltammetric responses for variations in deposition time is shown in **Fig. 6.** After obtaining the voltammogram results for the different deposition time, the IpC value was determined from the highest peak current for each composition, as shown in the **Table 3.**

The condition selected as the optimal condition was determined based on the highest cathodic peak current (IpC) value observed among the tested conditions. The results showed that a deposition time of 5 seconds yielded the highest IpC of -4.9651×10^{-3} A. During longer deposition times, the accumulation of fructose on the electrode surface exceeds the binding capacity of the MIP cavities; this condition can inhibit electron transfer, leading to a decrease in cathodic current. Therefore, a deposition time of 5 seconds was established as the optimum condition, as it supported the most efficient electron transfer at the electrode surface.

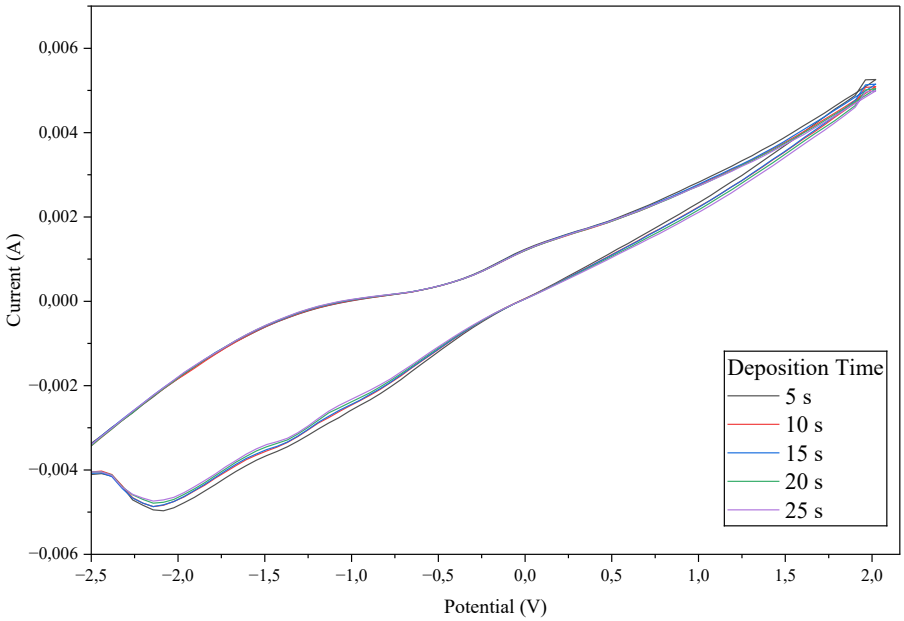

Figure 6. Cyclic voltammogram of deposition time variations

Table 3. IpC values of deposition time variations

Deposition time (s)	IpC (A)
5	-4,9651 x 10^{-3}
10	-4,8748 x 10^{-3}
15	-4,8678 x 10^{-3}
20	-4,7875 x 10^{-3}
25	-4,7359 x 10^{-3}

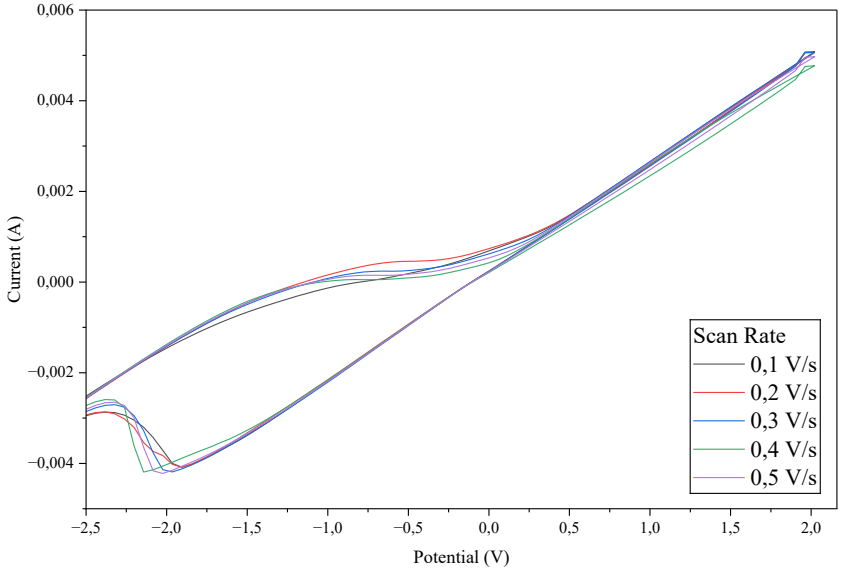

Figure 7. Cyclic voltammogram of scan rate variations

Table 4. IpC values of scan rate variations

Scan rate (V/s)	IpC (A)
0,1	-4,0860 × 10^{-3}
0,2	-4,0880 × 10^{-3}
0,3	-4,1210 × 10^{-3}
0,4	-4,1912 × 10^{-3}
0,5	-4,1924 × 10^{-3}

Scan rate influences the rate of diffusion layer formation and the magnitude of the peak current in the voltammogram. The cyclic voltammetric responses for variations in scan rate is shown in **Fig. 7**. After obtaining the voltammogram results for the different scan rate, the IpC value was determined from the highest peak current for each composition, as shown in the **Table 4**.

The condition selected as the optimal condition was determined based on the highest cathodic peak current (IpC) value observed among the tested conditions. The results demonstrated that IpC increased consistently with increasing scan rate, from -4.0860 × 10^{-3} A at 0.1 V/s to -4.1924 × 10^{-3} A at 0.5 V/s. This increase occurred because a higher scan rate accelerated the formation of the diffusion layer, thereby enhancing electron transfer at the electrode surface (Setiarso & Inggriani, 2021). Furthermore, the MIP and KCl modifiers accelerated the redox reaction rate at the electrode surface (Irdhawati et al., 2019). Based on these results, a scan rate of 0.5 V/s was established as the optimum condition for cyclic voltammetric measurement of fructose using the Agar: MIP: KCl modified electrode.

3.8. Comparison of MIP-modified electrodes in fructose and glucose

To ensure that the MIP-modified electrode used was selective for fructose, testing was conducted with another sugar glucosein three replicates. The testing was performed under various optimal conditions (electrode composition, pH, deposition time, and scan rate). The test results are shown in **Fig. 8**.

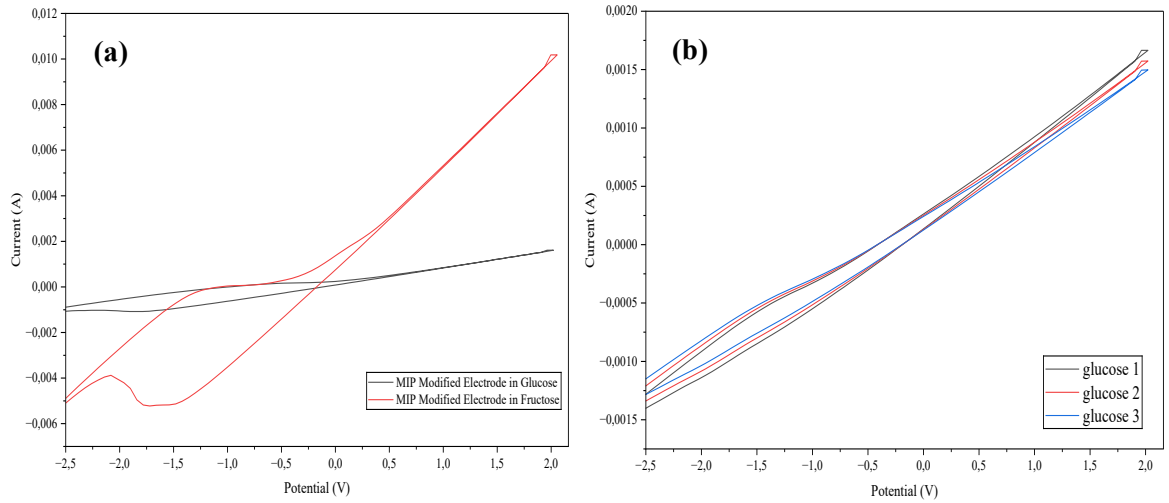

Figure 8. Comparison of MIP-modified electrodes in (a) fructose and (b) glucose

From the voltammogram data above, the IpC values were obtained from the highest current, as shown in **Table 5**. The measurement results show that the MIP (Molecularly Imprinted Polymer) electrode recorded the highest IpC value of -5.225 × 10^{-3} A. After the template extraction process, cavities of a specific size and shape corresponding to the fructose molecule were formed. These cavities allow fructose from the sample solution to enter and bind with optimal orientation, thereby significantly increasing the amount of fructose participating in the reduction reaction.

Supported by the ionic conductivity of KCl, electron transfer occurs more efficiently and produces the strongest electrochemical signal. When the electrode was tested on a glucose sample, the resulting peak current was very low, with an average IpC of (-1.276 × 10-3 A), and did not produce a broad electrochemical signal like that observed with the fructose sample. This data is crucial because it demonstrates that the cavities formed on the MIP are indeed specifically designed for fructose. Although glucose has a similar structure, it cannot fit perfectly into the MIP template. This proves that the developed MIP electrode exhibits high selectivity for fructose over glucose.

Table 5. IpC Values of MIP-modified electrodes in fructose and glucose

MIP-modified electrodes	IpC (Ampere)
In fructose	-5,225 × 10^{-3}
In glucose	-1,080 × 10^{-3}
In glucose 1	-1,402 × 10^{-3}
In glucose 2	-1,340 × 10^{-3}
In glucose 3	-1,285 × 10^{-3}

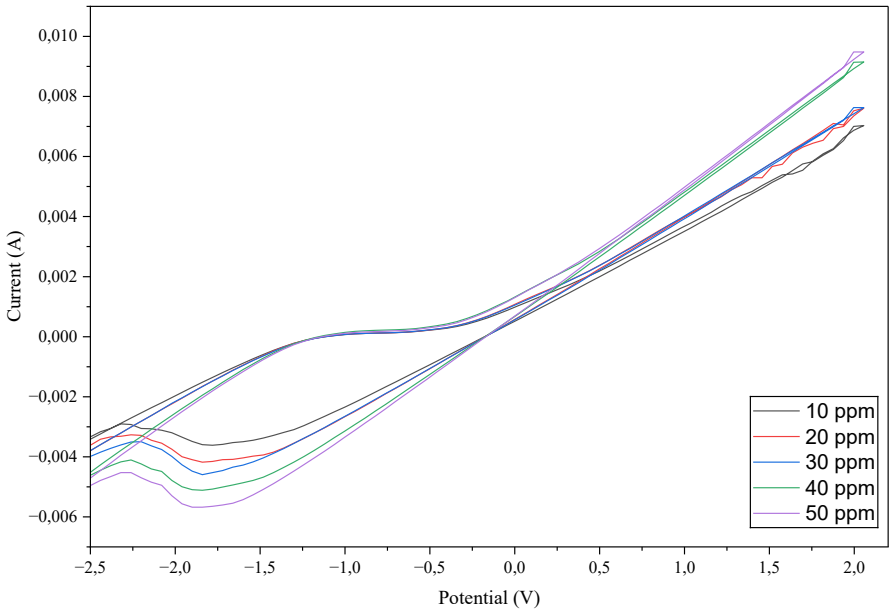

Figure 9. Cyclic voltammogram of fructose standard solutions

Table 6. IpC values of fructose standard solutions

Concentration (ppm)	IpC (A)
10	-3,6207 × 10^{-3}
20	-4,1810 × 10^{-3}
30	-4,5996 × 10^{-3}
40	-5,1199 × 10^{-3}
50	-5,6793 × 10^{-3}

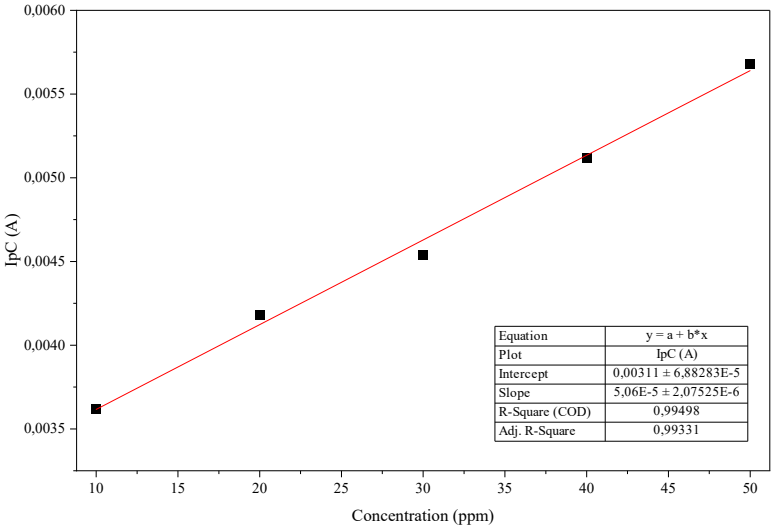

Figure 10. Calibration curve of IpC versus fructose standard solution concentration

Table 7. Absorbance values of fructose standard solutions

Concentration (ppm)	Absorbance
10	2,62 × 10^{-1}
20	2,73 × 10^{-1}
30	2,82 × 10^{-1}
40	2,93 × 10^{-1}
50	3,05 × 10^{-1}

3.9 Calibration Curves of Cyclic Voltammetry and UV-Vis Spectrophotometry

The cathodic peak current (IpC) values obtained from cyclic voltammetry at varying fructose concentrations were used to construct a calibration curve for fructose. The voltammogram results for the standard solution are shown in **Fig. 9.** Based on the results of the voltammogram, the IpC value was determined from the highest current value, as shown in **Table 6.** Next, a calibration curve was plotted showing the relationship between the standard solutions and the IpC values, as shown in the **Fig. 10.** Based on the IpC values, a standard fructose curve was plotted as

follows. From the cyclic voltammetry standard curve above, the equation of the line is $y = 0.0000506x + 0.00311$ with $R^2 = 0.99498$. Where these equations are used to calculate the recovery percentage, LOD, and LOQ as well as the honey content of each sample. Next, the standard solution was measured using UV-VIS spectrophotometry. The absorbance values are shown in the **Table 7.** Next, a calibration curve was plotted showing the relationship between the standard solutions and the absorbance values, as shown in the **Fig. 11.** From the UV-VIS spectrophotometer standard curve above, the equation is $y = 0.00105x + 0.2517$ with $R^2 = 0.9961$. Where these equations are used to calculate the recovery percentage, LOD, and LOQ as well as the honey content of each sample.

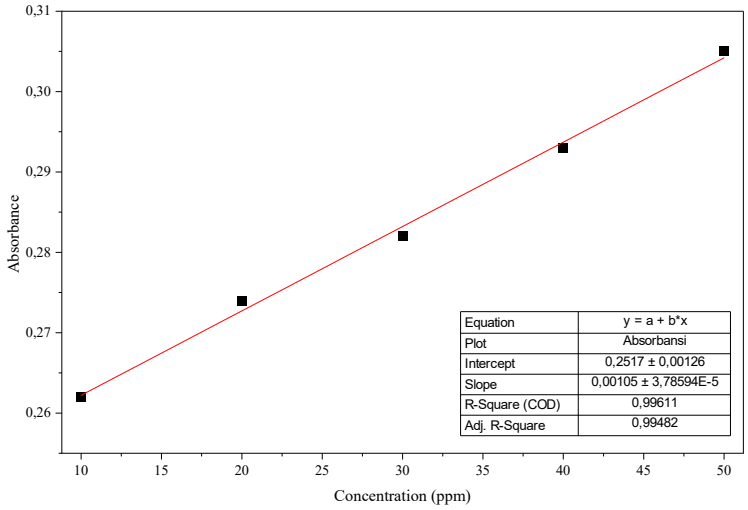

Figure 11. Calibration curve of Absorbance versus fructose standard solution concentration

3.9. Fructose Content Determination in Honey by Cyclic Voltammetry and UV-Vis Spectrophotometry

Subsequently, the honey samples were tested. The IpC values and sample absorbances were then substituted into the equations above to determine the honey's fructose content. The voltammogram results for the honey measurements are shown in **Fig. 12**. From the voltammogram results above, the IpC value is obtained from the highest current peak, as shown in **Table 8**.

Based on the IpC values above, the equation is $y = 0.0000506x + 0.00311$ with $R^2 = 0.99498$ was used to calculate the fructose content in honey. Thus, the cyclic voltammetric analysis yielded fructose contents of 27.667 ppm in honey A, 20.355 ppm in honey B, and 16.403 ppm in honey C. Next, the honey samples were analyzed using UV-Vis spectrophotometry, yielding the absorbance values shown in **Table 9**.

Based on the absorbance values above, the equation $y = 0.00105x + 0.2517$ with $R^2 = 0.9961$ was used to calculate the fructose content in honey. The UV-Vis spectrophotometry analysis yielded fructose contents of 25.047 ppm in honey A, 18.380 ppm in honey B, and 15.523 ppm in honey C.

The honey content results from both instruments were tested using an Independent Samples t-test in SPSS to determine whether there is a difference between measurements using UV-VIS and cyclic voltammetry, yielding a significance value (sig. 2-tailed) of $0.694 > 0.05$, indicating no significant difference between the cyclic voltammetry and UV-Vis spectrophotometry tests.

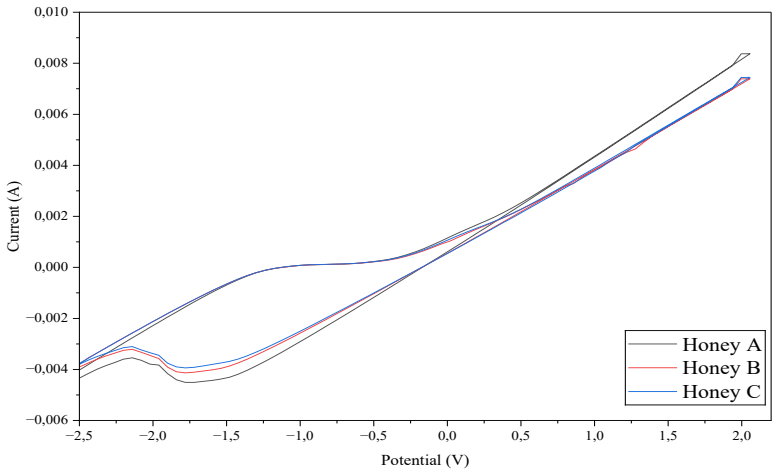

Figure 12. Cyclic voltammogram of fructose measurement in honey samples

Table 8. IpC values of honey sample measurements by cyclic voltammetry

Type of Honey	IpC (A)
Honey A	-4,5129 × 10^{-3}
Honey B	-4,1387 × 10^{-3}
Honey C	-3,9449 × 10^{-3}

Table 9. Absorbance values of honey sample measurements by UV-Vis spectrophotometry

Type of Honey	Absorbance
Honey A	2,780 × 10^{-1}
Honey B	2,710 × 10^{-1}
Honey C	2,680 × 10^{-1}

3.10. Limit of Detection (LOD), Limit of Quantitation (LOQ), and Percent Recovery

The Limit of Detection (LOD) is the lowest concentration of an analyte that an analytical instrument can detect. However, it cannot yet be accurately quantified. The Limit of Quantitation (LOQ) is the smallest concentration of an analyte that can be quantitatively determined with an acceptable level of accuracy and precision (Taleuzzaman, 2018). The calculations of the LOD and LOQ values using cyclic voltammetry can be found in **Table 10**.

$$\text{LOD} = \frac{3{,}3 \; x \; s(\frac{y}{x})}{slope} \quad \text{..... (1)}$$

$$\text{LOQ} = \frac{10 \; x \; s(\frac{y}{x})}{slope} \quad \text{..... (2)}$$

Based on the calculations, the cyclic voltammetry method yielded an LOD of 2.642 ppm, an LOQ of 8.808 ppm. Which demonstrates adequate detection capability for determining fructose levels in the sample matrix. The calculations of the LOD and LOQ values using UV-Vis spectrophotometry can be found in **Table 11.**

Table 10. LOD and LOQ Values Using Cyclic Voltammetry

Concentration (ppm)	IpC (Yi)	Ŷ	(Ŷ-Yi)²
10	3,620 × 10⁻³	3,616 × 10⁻³	1,600 × 10⁻¹¹
20	4,181 × 10⁻³	4,122 × 10⁻³	3,364 × 10⁻¹⁰
30	4,599 × 10⁻³	4,628 × 10⁻³	7,840 × 10⁻¹⁰
40	5,119 × 10⁻³	5,134 × 10⁻³	1,960 × 10⁻¹⁰
50	5,679 × 10⁻³	5,640 × 10⁻³	1,600 × 10⁻⁹
	∑(Ŷ − Yi)²		5,960 × 10⁻⁹
	s(y/x)		4,457 × 10⁻⁵
	slope		5,060 × 10⁻⁵
	LOD		2,642 ppm
	LOQ		8,808 ppm

Table 11. LOD and LOQ Values Using UV-Vis spectrophotometry

Concentration (ppm)	Absorbance (Yi)	Ŷ	(Ŷ-Yi)²
10	2,620 × 10⁻¹	2,620 × 10^{-1}	0
20	2,730 × 10⁻¹	2,730 × 10^{-1}	1 x 10^{-6}
30	2,820 × 10⁻¹	2,830 × 10^{-1}	1 x 10^{-6}
40	2,930 × 10⁻¹	2,930 × 10^{-1}	0
50	3,050 × 10⁻¹	3,040 × 10^{-1}	1 x 10^{-6}
	∑(Ŷ − Yi)²		3 x 10^{-6}
	s(y/x)		1 x 10^{-3}
	slope		1,050 x 10^{-3}
	LOD		2,857 ppm
	LOQ		9,524 ppm

Based on the calculations, the UV-Vis spectrophotometry yielded an LOD of 2.857 ppm, an LOQ of 9.524 ppm. Which demonstrates adequate detection capability for determining fructose levels in the sample matrix.

Percent recovery is a measure of how well an analytical method recovers a specific amount of a substance from a sample after testing. Percent recovery were calculated using the following equations.

$$\%\text{recovery} = \frac{Cmeasured}{Ctheoritical} \text{ x } 100\% \text{..... (3)}$$

The calculations of the recovery percentage using cyclic voltammetry are shown in **Table 12**. Based on the IpC values above, the equation $y = 0.0000506x + 0.00311$ with $R^2 = 0.99498$ was used to calculate the percentage recovery. The recovery percentage obtained using cyclic voltammetry was 101.112%. The calculations of the recovery percentage using UV-Vis spectrophotometry are shown in **Table 13**. Based on the absorbance values above, the equation $y = 0.00105x + 0.2517$ with $R^2 = 0.9961$ was used to calculate the percentage recovery. The recovery percentage obtained using UV-Vis spectrophotometry

was 98.500%. According to Harmita (2004), the acceptable range for the recovery percentage of an analyte is 90–110%. Both recovery values 101.112% for the cyclic voltammetric method and 98.50% for the UV-Vis spectrophotometric method fall within an acceptable range. This range is flexible depending on the analyte being tested, the sample concentration, and the laboratory conditions. Indicates that the voltammetry method using an MIP modified electrode good sensitivity and good accuracy for the analysis of fructose samples in honey.

Table 12. % Recovery in Cyclic Voltammetry

IpC (A)	C*theoritical* (ppm)	C*measured* (ppm)	%Recorvery
$3{,}620 \times 10^{-3}$	10	10,079	100,790%
$4{,}181 \times 10^{-3}$	20	21,146	105,730%
$4{,}599 \times 10^{-3}$	30	29,446	98,153%
$5{,}119 \times 10^{-3}$	40	39,723	99,307%
$5{,}679 \times 10^{-3}$	50	50,790	101,580%
	Mean		**101,112%**

Table 13. % Recovery in UV-Vis spectrophotometry

Absorbance	C*theoritical* (ppm)	C*measured* (ppm)	%Recorvery
$2{,}620 \times 10^{-1}$	10	9,809	98,090%
$2{,}730 \times 10^{-1}$	20	20,285	101,420%
$2{,}820 \times 10^{-1}$	30	28,857	96,190%
$2{,}930 \times 10^{-1}$	40	39,333	98,330%
$3{,}050 \times 10^{-1}$	50	50,761	101,430%
	Mean		**98,500%**

4. CONCLUSIONS

The optimal composition of the MIP-modified electrode was determined to be 1:1:2 (w/w) agar: MIP: KCl. The optimum measurement conditions for fructose determination in honey by cyclic voltammetry were pH 5, a deposition time of 5 seconds and a scan rate of 0.5 V/s, yielding an LOD of 2.642 ppm, an LOQ of 8.808 ppm, and a recovery of 101.112%. The fructose content determined by cyclic voltammetry was 27.667 ppm for honey A, 20.355 ppm for honey B, and 16.403 ppm for honey C, while the fructose content determined by UV-Vis spectroscopy was 25.047 ppm for honey A, 18.380 ppm for honey B, and 15.523 ppm for honey C. A comparison of fructose measurement results in honey using cyclic voltammetry and UV-Vis spectrophotometry showed no significant difference, as indicated by a significance value (sig. 2-tailed) of 0.694 > 0.05, confirming the reliability and validity of the developed MIP-modified electrode as a selective and sensitive analytical method for fructose determination in honey.

ACKNOWLEDGMENT

The authors funded this research with no external financial support.

LIST OF REFERENCES

Asni, N. K., & Sianita, M. M. (2020). Pengaruh jumlah *crosslinker* terhadap

persen ekstraksi pada sintesis *molecularly imprinted polymer* sebagai adsorben untuk kloramfenikol. *Unesa Journal of Chemistry*, *9*(3), 179–188. https://doi.org/10.26740/ujc.v9n3.p179-188

Barry, S. C. L., Franke, C., Mulaudzi, T., Pokpas, K., & Ajayi, R. F. (2023). Review on surface-modified electrodes for the enhanced electrochemical detection of selective serotonin reuptake inhibitors (SSRIs). *Micromachines*, *14*(7), 1334. https://doi.org/10.3390/mi14071334

Carballido, L., Karbowiak, T., Cayot, P., Gerometta, M., Sok, N., & Bou-Maroun, E. (2022). Applications of molecularly imprinted polymers and perspectives for their use as food quality trackers. *Chem*, 8(9), 2330–2341. https://doi.org/10.1016/j.chempr.2022.05.021

Codex Alimentarius. (2022). S *Standar for honey* (CXS 12-1981). FAO/WHO.

Silva, P. M., Gauche, C., Gonzaga, L. V., Costa, A. C. O., & Fett, R. (2016). Honey: Chemical composition, stability and authenticity. *Food Chemistry*, *196*, 309–323. https://doi.org/10.1016/j.foodchem.2015.09.051

Fransiska, S., & Sianita, M. M. (2021). Pengaruh suhu pada sintesis *Molecularly Imprinted Polymer* (MIP) terhadap kemampuan adsorpsi kloramfenikol. *Unesa Journal of Chemistry*, *10*(3), 209–219. https://doi.org/10.26740/ujc.v10n3.p209-219

Harmita. 2004. Petunjuk Pelaksanaan Validasi Metode dan Cara Perhitungannya. *Majalah Ilmu Kefarmasian.* 1(3).117 – 134. Departemen Farmasi FMIPA. Universitas Indonesia. Jakarta

Hasaneen, N., Akhtarian, S., Pulicharla, R., Brar, S. K., & Rezai, P. (2024). Surface molecularly imprinted polymer-based sensors for antibiotic detection. *TrAC Trends in Analytical Chemistry*, *170*, 117389. https://doi.org/10.1016/j.trac.2023.117389

Herlina, H., Ritonga, A. H., Andy Febriady, Asvia Rahayu, & Sinaga, N. G. (2025). Pengembangan material polimer cetak molekul sebagai elemen pengenalan selektif pada sensor elektrokimia meropenem. *Jurnal Farmasimed (JFM)*, *8*(1), 265–274. https://doi.org/10.35451/j884sv81

Inggriani, F. & Setiarso, P. (2020). Synthesis of graphene oxide-nanozeolite composite electrode for aspirin analysis by cyclic voltammetry. *Asian Journal of Chemistry*, *32*(10), 2541–2544. https://doi.org/10.14233/ajchem.2020.22556

Inggriani, F., & Setiarso, P. (2021). Pembuatan elektroda pasta karbon untuk analisis parasetamol secara differential pulse voltametri. *Indonesian Chemistry and Application Journal*, *4*(2), 27–31. https://doi.org/10.26740/icaj.v4n2.p27-31

Irdhawati, I., Indrayani, V. E., & Sahara, E. (2019). Teknik voltammetri pelucutan anodik menggunakan elektroda glassi karbon dalam penentuan kadar logam Fe dalam terong ungu. *Jurnal Kimia Riset*, *4*(2), 111–120. https://doi.org/10.20473/jkr.v4i2.15897

Jupri, R., Fauziah, S., & Taba, P. (2022). Sintesis dan karakterisasi *molecularly imprinted polymers* menggunakan metil metakrilat dan etilen glikol dimetakrilat sebagai adsorben di-(2-etilheksil) ftalat. *Journal of Pure and Applied Chemistry*, *5*(3), 105–120. http://dx.doi.org/10.26418/indonesian.v5i3.59132

Oktaningtias, E. F., & Sianita, M. M. (2025). Effect of extraction temperature of molecularly imprinted polymer in chloramphenicol adsorption using UV-Vis spectrophotometry based on diazotation reaction. *Jurnal Pijar Mipa*,

20(1), 29–34. https://doi.org/10.29303/jpm.v20i1.8001

Rao, H., Lu, Z., Ge, H., Liu, X., Chen, B., Zou, P., Wang, X., He, H., Zeng, X., & Wang, Y. (2017). Electrochemical creatinine sensor based on a glassy carbon electrode modified with a molecularly imprinted polymer and a Ni@polyaniline nanocomposite. *Microchimica Acta*, *184*(1), 261–269. https://doi.org/10.1007/s00604-016-1998-x

Rusnadi, W. R., & Setiarso, P. (2020). Pembuatan elektroda nano karbon untuk analisis logam Pb(II) secara siklik voltametri. *Unesa Journal of Chemistry*, *9*(1), 72–77. https://doi.org/10.26740/ujc.v9n1.p72-77.

Ruswandi, Oktavia, B., & Azhar, M. (2018). Penentuan kadar fruktosa hasil hidrolisis inulin dengan DNS sebagai pengoksidasi. *Eksakta*, *19*(1), 1–20. https://doi.org/10.24036/eksakta/vol19-iss01/102

Se, K. W., Wahab, R. A., Syed Yaacob, S. N., & Ghoshal, S. K. (2019). Detection techniques for adulterants in honey: Challenges and recent trends. *Journal of Food Composition and Analysis*, *80*, 16–32. https://doi.org/10.1016/j.jfca.2019.04.001

Shi, Z., Xia, L., & Li, G. (2023). Recent progress of electrochemical sensors in food analysis. *Chemosensors*, *11*(9), 478. https://doi.org/10.3390/chemosensors11090478

Sianita, M. M, Puspaningsih, N. N., Khazanah, M., & Supriyanto, G. (2019). Comparison of the method used for extraction chloramphenicol from its Molecularly Imprinted Polymer (MIP) using chloroform as porogen. *Atlantis Highlights in Chemistry and Pharmaceutical Sciences*, 1, 17-18. https://doi.org/10.2991/snk-19.2019.5

Sihombing, V. H., & Hakim, A. S. (2020). Penggunaan wolfram pada potensiometri untuk mendeteksi baffer pospat dan enzim urease. *Einstein Journal*, *9*(1), 46–52.

Sirumapea, L., Zulfikar, M. A., Amran, M. B., & Alni, A. (2021). Selective solid-phase extraction of meropenem from human blood plasma using a molecularly imprinted polymer. *Indonesian Journal of Chemistry*, *21*(5), 1167–1179. https://doi.org/10.22146/IJC.64025

Softic, S., Cohen, D. E., & Kahn, C. R. (2016). Role of dietary fructose and hepatic de novo lipogenesis in fatty liver disease. *Digestive Diseases and Sciences*, *61*(5), 1282–1293. https://doi.org/10.1007/s10620-016-4054-0

Taleuzzaman, M. (2018). Limit of Blank (LOB), Limit of Detection (LOD), and Limit of Quantification (LOQ). *Organic & Medicinal Chemistry International Journal*, *7*(5), 555722. https://doi.org/10.19080/omcij.2018.07.555722

Taskinen, M. R., Packard, C. J., & Borén, J. (2019). Dietary fructose and the metabolic syndrome. *Nutrients*, *11*(9), 1–16. https://doi.org/10.3390/nu11091987

Zulfikar, M. A. (2022). *Material fungsional polimer bercetakan molekul: Aplikasi dan tantangannya di masa depan* [Orasi Ilmiah Guru Besar]. Institut Teknologi Bandung.

Jurnal Ilmiah Berkala: Sains dan Terapan Kimia
Vol.20 No. 2, July 2026

In Silico Identification of Natural Compounds as Potential FGF2 Inhibitors for Glioblastoma Therapy

Identifikasi Senyawa Alami Secara In Silico sebagai Inhibitor FGF2 Potensial untuk Terapi Glioblastoma

Nico Berlinson Fernando[1], Siti Hodijah[1] Agus Kartono[1], and Setyanto Tri Wahyudi[1]*

[1]Department of Physics, Faculty of Mathematics and Natural Sciences, IPB University, Bogor, 16680, Indonesia

**Email: stwahyudi@apps.ipb.ac.id*

ABSTRACT

Glioblastoma multiforme (GBM) is the most aggressive primary malignant brain tumor and remains difficult to treat due to its high level of invasion, resistance to therapy, and poor prognosis. Fibroblast growth factor 2 (FGF2) plays a crucial role in glioblastoma development by increasing glioma cell proliferation, angiogenesis, and the maintenance of glioblastoma cancer stem cells. Therefore, this study aims to identify candidate FGF2 inhibitors from natural compounds through virtual screening and molecular docking approaches. The binding sites on FGF2 were identified through protein-protein docking approaches between FGF2 and FGFR1-FGFR4, then used as the basis for virtual screening of 1,496 natural compounds using AutoDock Vina. Compounds that showed competitive binding energy were further analyzed using targeted and blind docking with AutoDock4. The results showed that Pyranoamentoflavone, 5,3',5'-Trihydroxy-6,7,4'-trimethoxyflavone, Sotetsuflavone, and Isotrilobine have competitive binding affinity to the active site of FGF2. These findings indicate that these four compounds have potential as FGF2 inhibitor candidates for the development of targeted therapies for GBM. However, further validation through molecular dynamics simulations as well as in vitro and in vivo studies is still needed to confirm their binding stability, safety, and therapeutic efficacy.

Keywords: *GBM; FGF2; natural compounds; molecular docking; virtual screening*

Received: 21 April 2026; **Accepted**: 15 July 2026; **Available online**: 29 July 2026

1. INTRODUCTION

Glioblastoma (GBM) is a type of malignant brain tumor classified as a grade IV tumor by the World Health Organization (WHO) classification. GBM has a poor prognosis, with a median survival of only 12–15 months despite standard therapy (Lee et al., 2018).

One of the main reasons for the low therapeutic success is the presence of a subpopulation of stem cell-like cells (CSCs) that are resistant to cytotoxic therapy. Furthermore, the high rate of genomic mutations in GBM further increases therapy resistance and enhances treatment strategies

(Garnier et al., 2019). Various therapeutic strategies have been implemented in the treatment of GBM, including surgical resection, radiotherapy, and chemotherapy based on alkylating agents such as temozolomide (TMZ) and antiangiogenic agents such as bevacizumab. However, these therapeutic advances have not significantly improved the prognosis of GBM patients in recent decades (Kumari & Kumar, 2023).

Epidemiologically, the annual incidence of primary malignant brain tumors is reported to reach 7.08 cases per 100,000 population (Ostrom et al., 2020). Therefore, the development of more effective targeted therapies remains a major focus of research to improve the therapeutic efficacy and prognosis of GBM patients. Fibroblast Growth Factor 2 (FGF2) is an oncogenic factor that plays a crucial role in the development of glioblastoma (GBM), primarily through its ability to increase glioma cell proliferation, stimulate angiogenesis, and maintain self-renewal properties in glioblastoma cancer stem cells (GBM CSCs) (Haley & Kim, 2014; Toyoda et al., 2013). Based on these roles, the FGF2/FGFR signaling pathway is a promising therapeutic target for inhibiting GBM progression.

Experimental evidence suggests that FGF2 inhibition using antisense oligonucleotides and specific antibodies effectively suppresses glioma cell proliferation and angiogenesis (Haley & Kim, 2014). In addition to FGF2, this pathway can also be targeted at the FGFR receptor level. FGFR1 is the most studied receptor because it is associated with poor prognosis, increased glioma cell migration, GSC maintenance, and increased tumorigenicity in vivo. Conversely, FGFR1 inhibition suppresses tumor growth and GSC migration (Kowalski-Chauvel et al. 2019; Jimenez-Pascual et al. 2019).

Unlike FGFR1, the roles of FGFR2, FGFR3, and FGFR4 in GBM remain incompletely understood. FGFR2 is associated with the regulation of glioma progression, FGFR3 is known to undergo oncogenic fusion (FGFR3-TACC3) in some glioma cases, while FGFR4 has low expression levels and its biological function in GBM is still unclear (Di Stefano et al., 2015; Jimenez-pascual et al., 2019). Thus, targeting FGF2 is considered more potential than targeting a single FGFR receptor because FGF2 acts as an upstream regulator that initiates the activation of all members of the FGFR family (FGFR1–FGFR4) (Ornitz & Itoh, 2015). Research on the use of natural compounds as glioblastoma therapy candidates has continued to grow in recent decades because these compounds possess various pharmacological activities, including antitumor, antioxidant, antiviral, and anti-inflammatory activities (Copolovici et al., 2017).

One approach widely used in the early stages of drug discovery is virtual screening through molecular docking, which is able to predict the binding affinity and orientation of ligands to target proteins at the atomic level (Kiametis et al., 2017). This approach is widely used in the drug discovery process because it can accelerate the selection of candidate compounds more efficiently in terms of time and cost (Meng et al., 2011).

Among the various molecular docking software packages available, AutoDock Vina and AutoDock4 are two widely used software packages because they are able to predict binding poses with the lowest binding energy in a relatively short computation time (Chen et al., 2023; Trott & Olson, 2010). Therefore, this study aims to identify glioblastoma therapy candidates derived from natural compounds through virtual screening and molecular docking approaches.

2. MATERIALS AND METHODS

2.1. Materials

The crystal structure of Fibroblast Growth Factor 2 (FGF2; PDB ID: 4OEE) and the crystal structures of fibroblast growth factor receptors including FGFR1 (PDB ID: 5EW8), FGFR2 (PDB ID: 3B2T), FGFR3 (PDB ID: 6PNX), and FGFR4 (PDB ID: 4QQT) were obtained from the Protein Data Bank (PDB) (https://www.rcsb.org/). A total of 1,496 natural compounds were collected from several scientific articles and the UI Herbal database. The structures of these compounds were then downloaded from the PubChem database in SDF format.

2.2. Method

2.2.1 Selection of FGF2 target protein structures

A total of 22 crystal structures of FGF2 (homo sapiens) are available in the UniProt database (P09038). Target protein structures were selected based on X-ray imaging, resolution ≤ 2.5 Å, 100% sequence identity, and annotation as FGF2.

Based on these criteria, the FGF2 structure with PDB ID 4OEE was selected as the target protein due to its 100% sequence identity and the highest resolution (1.50 Å). The three-dimensional structure of the protein was downloaded from the Protein Data Bank (PDB) (https://www.rcsb.org/). Next, the FGF2 protein structure was separated from water molecules and attached substrate using VMD.

2.2.2 Prediction of FGF2 binding sites

Identification of FGF2 binding sites was carried out by utilizing its natural interactions with the crystal structures of the FGFR1 (PDB ID: 5EW8), FGFR2 (PDB ID: 3B2T), FGFR3 (PDB ID: 6PNX), and FGFR4 (PDB ID: 4QQT) receptors. Binding site prediction was performed using the ZDOCK 3.0.2 server (https://zdock.umassmed.edu/) through the protein–protein docking method. The docking results were analyzed to identify FGF2 residues that interact with each receptor. These residues were then used as a reference in determining the binding site and grid box position in the molecular docking process.

2.2.3 Ligand preparation

In this study, a total of 1,496 active compounds were compiled from several scientific articles and the UI Herbal Database (HerbalDB), a database of Indonesian medicinal plant compounds developed by the University of Indonesia and still publicly accessible at the time of dataset collection. The chemical structures of the active compounds were downloaded from PubChem (https://pubchem.ncbi.nlm.nih.gov/) in SDF format.

Next, the ligand structures were geometrically optimized using ORCA. The optimized structures were first converted to PDB format using Open Babel and then further converted to PDBQT format using AutoDockTools 1.5.7 (Forli et al., 2016) for use in the molecular docking process.

2.2.4 Virtual screening using AutoDock Vina

Virtual screening of 1,496 natural compounds was performed through molecular docking analysis using AutoDock Vina at four previously identified FGF2 binding sites. The entire docking process was performed using the same parameters for each binding site. The docking results were then sorted based on the obtained binding energy values.

The five compounds with the most negative binding energy values at each binding site were selected as initial candidates for further analysis. From these candidates, compounds identified at more than one binding site were further evaluated based on

drug-likeness and validated through targeted docking and blind docking using AutoDock4.

2.2.5 Drug-likeness prediction

Compounds identified at more than one binding site were then evaluated using SwissADME (http://www.swissadme.ch/) (Daina et al., 2017) to predict physicochemical, pharmacokinetic, and drug-likeness characteristics. Drug-likeness evaluation was performed based on Lipinski's Rule of Five, which includes a molecular mass <500 g/mol, hydrogen bond donor (HBD) ≤ 5, hydrogen bond acceptor (HBA) ≤ 10, logP value ≤ 5, and molar refractivity in the range of 40–130 (Mustafa et al., 2020).

In addition, Pan-Assay Interference Structures (PAINS) analysis was performed to identify molecular substructures that could potentially cause interference in various bioassays, resulting in false positives. This analysis is used as an initial screening stage to minimize the selection of compounds with non-specific biological activity (Baell & Holloway, 2010).

2.2.6 Further analysis of selected compounds using AutoDock4

In targeted docking, the docking process was performed using the Lamarckian Genetic Algorithm (LGA) with 25,000,000 energy evaluations, a population size of 300, and 100 iterations (runs). The resulting docking poses were then clustered using an RMSD tolerance of 2.0 Å. For each compound, the pose with the lowest binding energy value from the dominant cluster was selected as a representation of the docking results. The interactions between the ligand and amino acid residues in the FGF2 protein were then analyzed and visualized using LigPlot+. Next, blind docking was performed using the same parameters as targeted docking, but with an expanded search space to cover the entire surface of the FGF2 protein. At this stage, three grid spacing variations were used, namely 0.375 Å, 0.500 Å, and 0.625 Å, to evaluate the effect of grid resolution on the docking results.

3. RESULTS AND DISCUSSION

3.1. Identification of FGF2 binding sites

Identification of FGF2 binding sites was performed through protein-protein docking with FGFR1, FGFR2, FGFR3, and FGFR4. **Table 1** presents a visualization of the interaction sites between FGF2 and FGFR1, FGFR2, FGFR3, and FGFR4, along with the FGF2 amino acid residues involved in these interactions. The protein-protein docking results indicate that FGF2 interacts with FGFR1, FGFR2, FGFR3, and FGFR4 through different amino acid residues on the protein surface.

In binding site 1, the residues involved include Arg97, Arg109, Thr112, Lys110, Trp114, and Gln134. Binding site 2 consists of Tyr24, Phe31, Lys46, Ser100, Gly133, and Leu140, while binding site 3 involves Pro14, Tyr24, Glu59, Gly61, Leu98, and Asr102. Binding site 4 is composed of Lys26, Phe31, Arg42, Glu45, Pro49, Arg120, Lys135, and Met142. Differences in the residues involved in each binding site indicate that FGF2 has multiple interface areas that can interact with members of the FGFR family. These residues were then used as references in determining binding sites for molecular docking of test compounds with the FGF2 protein.

Table 1 Interaction sites of FGF2 with FGFR1–FGFR4 predicted by protein–protein docking

Binding Site	Binding Area	FGF2 Amino Acid Residues
1	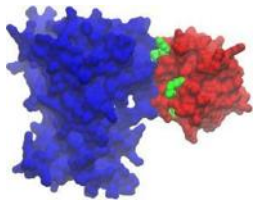	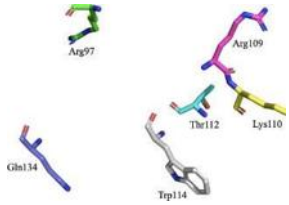
2	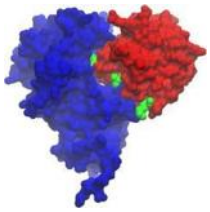	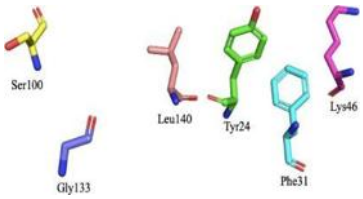
3	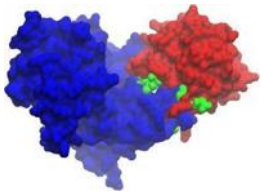	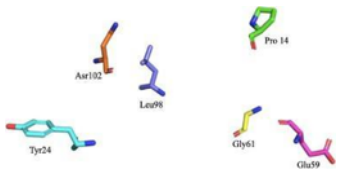
4	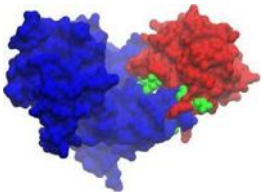	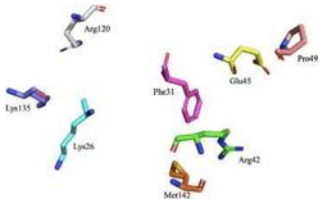

Note: Red indicates FGF2, blue indicates FGFR, and green indicates the protein–protein interaction interface.

3.2. Virtual screening of compounds against FGF2

Molecular docking is a computational method widely used in drug discovery and design to predict the binding mode of ligands to target proteins. This method allows for the evaluation of binding affinity based on binding energy and identifies interaction patterns between ligands and residues in the protein's active site (Sivakumar et al., 2020).

In this study, molecular docking of 1,496 natural compounds was performed using AutoDock Vina at four previously identified FGF2 binding sites. **Fig. 1** shows the distribution of binding energy values resulting from molecular docking of 1,496 natural compounds at each FGF2 binding site. All compounds are sorted based on their binding energy values, with candidates with the highest binding affinity at the beginning of the graph. This distribution indicates that only a small proportion of compounds have competitive binding affinity for the target protein. Based on the distribution of binding energy values, the five compounds with the most negative binding energy values at each binding site were selected as initial candidates and presented in **Table 2**. The more negative the binding energy value obtained, the stronger the interaction between the ligand and the target protein (Khan et al., 2025). Based on **Table 2**, pyranoamentoflavone is included in

the five best candidates and appears at all binding sites while 5,3',5'-trihydroxy-6,7,4'-trimethoxyflavone appears at binding sites 1, 2, and 4. Isotrilobine appears at binding sites 1 and 4, and sotetsuflavone at binding sites 1 and 2. The consistency of the appearance of the four compounds at several binding sites indicates a competitive binding affinity to FGF2 so they were selected as candidates for further analysis using AutoDock4.

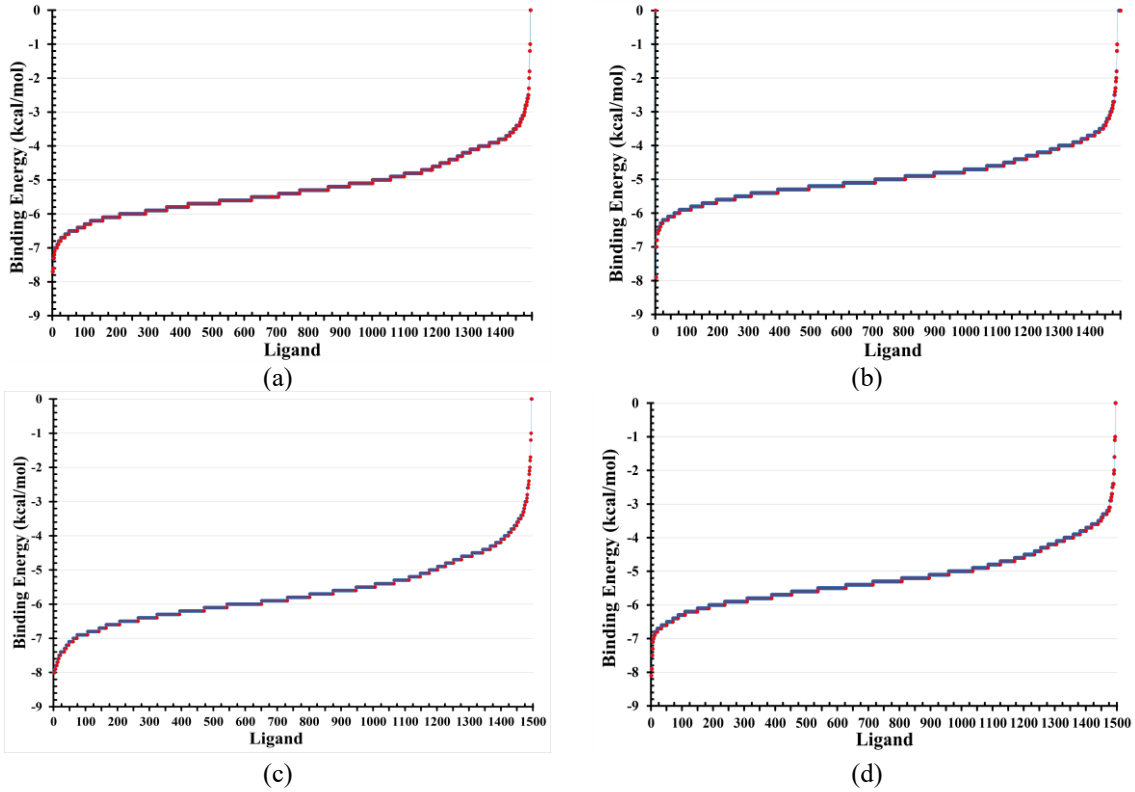

Figure 1. Distribution of binding energy values for 1,496 natural compounds at the four FGF2 binding sites obtained from molecular docking using AutoDock Vina: (a) binding site 1, (b) binding site 2, (c) binding site 3, and (d) binding site 4

Table 2 Top five compounds with the most negative binding energies at each FGF2 binding site

Binding Site FGF2	Information	CID	Compound	Binding Energy (kcal/mol)
1	Top 1	21581557	5,3',5'-Trihydroxy-6,7,4'-trimethoxyflavone	-7.7
	Top 2	21582613	Pyranoamentoflavone	-7.7
	Top 3	12310578	Isotrilobine	-7.6
	Top 4	442728	Cassiamin C	-7.3
	Top 5	5494868	Sotetsuflavone	-7.3

Binding Site FGF2	Information	CID	Compound	Binding Energy (kcal/mol)
2	Top 1	21581557	5,3',5'-Trihydroxy-6,7,4'-trimethoxyflavone	-7.9
	Top 2	21582613	Pyranoamentoflavone	-7.9
	Top 3	5280486	Raucaffricine	-7.0
	Top 4	441876	Agavoside A	-6.8
	Top 5	5494868	Sotetsuflavone	-6.8
3	Top 1	5322012	Grossamide	-8.0
	Top 2	12302850	Chandalone	-8.0
	Top 3	5281246	Mutatochrome	-7.9
	Top 4	21582613	Pyranoamentoflavone	-7.9
	Top 5	102034490	(4*aR*,4*bS*,7*S*,8*aS*,10*aS*)-3-[2-[(2*R*,4*aS*,4*bS*,8*aS*)-2,4*b*,8,8-tetramethyl-4,4*a*,5,6,7,8*a*,9,10-octahydro-3*H*-phenanthren-2-yl]-2-oxoethyl]-7-ethenyl-4*b*,7,10*a*-trimethyl-1-methylidene-5,6,8,8*a*,9,10-hexahydro-4*aH*-phenanthren-2-one	-7.9
4	Top 1	5281694	Robustaflavone	-8.1
	Top 2	21581557	5,3',5'-Trihydroxy-6,7,4'-trimethoxyflavone	-7.9
	Top 3	21582613	Pyranoamentoflavone	-7.9
	Top 4	12310578	Isotrilobine	-7.5
	Top 5	42607760	6,4'-Dihydroxyaurone 4-O-rutinoside	-7.3

3.3. Drug-likeness properties of selected compounds

Lipinski's Rule of Five (Ro5) is used as an initial parameter to predict the potential of a compound as a drug candidate with good oral bioavailability based on its structural characteristics. A compound that meets all rules or has only one violation can still be considered as a potential drug candidate (Mustafa et al., 2022). The analysis results presented in **Table 3** show that 5,3',5'-trihydroxy-6,7,4'-trimethoxyflavone does not violate Lipinski's rule, while pyranoamentoflavone and sotetsuflavone each show one violation. Meanwhile, isotrilobine shows two violations of Lipinski's rule. Nevertheless, these results still provide an initial picture that most compounds have structural characteristics that still support their potential as oral drug candidates. In addition to Ro5, PAINS analysis was used to evaluate the possibility of molecular structures that can cause false-positive results in biological tests. All compounds showed 0 PAINS structural alerts, indicating that no structural fragments were found that could potentially interfere with the results of biological tests (Abdizadeh, 2024). Based on pharmacokinetic predictions, 5,3',5'-trihydroxy-6,7,4'–trimethoxyflavone and isotrilobine have high GI absorption, so they are predicted to have better oral absorption potential than

pyranoamentoflavone and sotetsuflavone. In addition, most of the compounds are predicted not to be P-glycoprotein (P-gp) substrates, so they have the potential to not experience efflux mediated by this transporter. Overall, the results of this evaluation indicate that all four compounds have their respective advantages and limitations. However, the absence of PAINS alerts and the presence of pharmacokinetic parameters that still support these compounds indicate that these compounds remain relevant to be considered in further studies as FGF2 inhibitor candidates.

Table 3. Physicochemical parameters and predicted pharmacokinetic profiles of the selected compounds

Compound	Pyranoamentoflavone	5,3',5'-Trihydroxy-6,7,4' -trimethoxyflavone	Isotrilobine	Sotetsuflavone
Molecular weight (g/mol)	604.56	360.31	576.68	552.48
No of rotatable bonds	3	4	2	4
Num. H-bond acceptor	10	8	7	10
Num. H-bond donor	5	3	0	5
TPSA (Å^2)	170.8	118.59	52.63	170.8
Lipinski rule of 5	1	0	2	1
PAINS alerts	0	0	0	0
Pgp substrate	No	Yes	No	No
GI absorption	Low	High	High	Low

3.4. Advanced analysis of selected compounds using targeted docking AutoDock4

Based on the results of virtual screening using AutoDock Vina, four compounds with competitive binding affinities were selected for further analysis using targeted docking with AutoDock4. The use of different search algorithms and scoring functions in AutoDock4 is expected to provide a more comprehensive evaluation and increase confidence in the docking results (Chen et al., 2023). The results of targeted docking using AutoDock4 for the four selected compounds at each FGF2 binding site are presented in **Tables 4** and **5**. Based on the data in **Table 4**, pyranoamentoflavone showed the best binding affinity compared to other compounds with the most negative binding energy value of -7.90 kcal/mol at binding site 2. In addition, this compound was the only compound identified at all binding sites, indicating the ability to interact at various FGF2 binding areas. The compound 5,3',5'-trihydroxy-6,7,4'-trimethoxyflavone also showed relatively good binding affinity, especially at binding site 4, with a binding energy of -7.03 kcal/mol. Meanwhile, isotrilobine showed the best binding affinity at binding site 1, with a binding energy of -6.88 kcal/mol, while sotetsuflavone showed lower binding affinity than the other compounds. The positions of the compounds resulting from targeted docking on the surface of the FGF2 protein are shown in **Fig. 2**.

The reliability of the targeted docking results was further evaluated based on the entropy parameters and the percentage of cluster conformation, as presented in **Table 5**.

Isotrilobine showed the highest percentage of cluster conformation, at 100% at binding sites 1 and 4, with an entropy value of 0.00. These results indicate that all the resulting docking poses are concentrated in a single dominant cluster, indicating high reproducibility of the binding mode. Pyranoamentoflavone has a cluster percentage ranging from 36–64%, while 5,3',5'-trihydroxy-6,7,4'-trimethoxyflavone has a cluster percentage ranging from 31–48%. On the other hand, sotetsuflavone exhibits a relatively lower cluster percentage (33–35%), indicating that the docked conformation is more variable than the other compounds. This finding supports the reliability of the docking poses, which were subsequently used for residue interaction analysis in the FGF2 protein.

Table 4 Binding energy values from targeted docking of selected compounds against FGF2

Compound	Local/ Indonesian Name	Scientific Name	Binding site 1	Binding site 2	Binding site 3	Binding site 4
Pyranoamentoflavone	Nyamplung	*Calophyllum Inophyllum)*	-6.01	-7.9	-6.00	-7.04
5,3',5'-Trihydroxy-6,7,4' - trimethoxyflavone	Kemuning	*Murraya Paniculata*	-5.93	-5.13	-	-7.03
Isotrilobine	Cincau minyak	*Stephania Hernandifolia*	-6.88	-	-	-5.50
Sotetsuflavone	Jambe	*Cycas Revoluta*	-4.88	-4.75	-	-

Note: The "-" sign indicates that docking was not performed because the compound was not selected at the relevant binding site based on the virtual screening results using AutoDock Vina.

Table 5 Conformational cluster analysis of selected compounds based on targeted docking results

Binding site	Compound	Entropy	Conformation cluster (%)
1	5,3',5'-Trihydroxy-6,7,4' trimetoxyflavone	0.23	46
	Pyranoamentoflavone	0.17	64
	Isotrilobine	0.00	100
	Sotetsuflavone	0.45	35
2	5,3',5'-Trihydroxy-6,7,4'-trimethoxyflavone	0.32	48
	Pyranoamentoflavone	0.37	36
	Sotetsuflavone	0.45	33
3	Pyranoamentoflavone	0.34	51
4	5,3',5'-Trihydroxy-6,7,4'-trimethoxyflavone	0.43	31
	Pyranoamentoflavone	0.43	36
	Isotrilobine	0.00	100

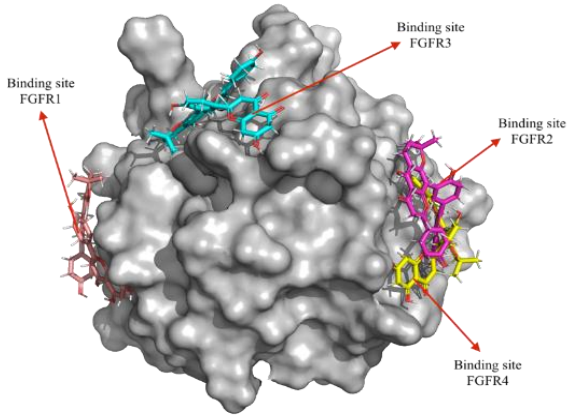

Figure 2. Binding pose of selected compounds resulting from targeted docking on the FGF2 protein

The pose with the lowest binding energy, derived from the dominant cluster, was then selected as a representative for further interaction analysis using LigPlot+ (**Fig. 3**). Pyranoamentoflavone and 5,3',5'-trihydroxy-6,7,4'-trimethoxyflavone showed similar interaction patterns by forming three hydrogen bonds with residues Arg44, Lys135, and Tyr103, as well as a number of hydrophobic interactions with residues Arg120, Gly28, Lys26, Phe31, Met142, Lys46, Leu140, and Tyr24.

In contrast to these two compounds, isotrilobine did not form hydrogen bonds and only interacted through hydrophobic contacts with residues Glu78, Lys110, Ser113, Thr112, Trp114, and Tyr111. Meanwhile, sotetsuflavone formed two hydrogen bonds with Thr112 as well as hydrophobic interactions with Glu78, Arg109, Lys110, Tyr111 and Trp114.

3.5. Blind docking analysis of selected compounds using AutoDock 4.2.6

After targeted docking at the predetermined binding sites, the four selected compounds were then analyzed using blind docking with AutoDock 4.2.6. Unlike targeted docking, which focuses on a specific binding site, this approach allows identification of the pose with the lowest binding energy without any binding site restrictions. The blind docking results are presented in **Table 6**, while the best pose on the FGF2 protein surface is visualized in **Fig. 4**.

All compounds yielded negative binding energy values at all three grid spacing variations (0.375, 0.500, and 0.625 Å), indicating that all compounds were still able to interact with the FGF2 protein even when docked without restrictions on specific binding sites. Furthermore, changes in grid spacing did not significantly impact the binding energy values obtained, so the blind docking results were relatively consistent at each grid resolution used.

The obtained binding energy values ranged from −6.08 to −7.19 kcal/mol. Sotetsuflavone showed the most negative binding energy value of −7.19 kcal/mol at a grid spacing of 0.375 Å, while pyranoamentoflavone, 5,3',5'-trihydroxy-6,7,4'-trimethoxyflavone, and isotrilobine showed the most negative binding energy values of −6.73, −6.84, and −6.52 kcal/mol, respectively.

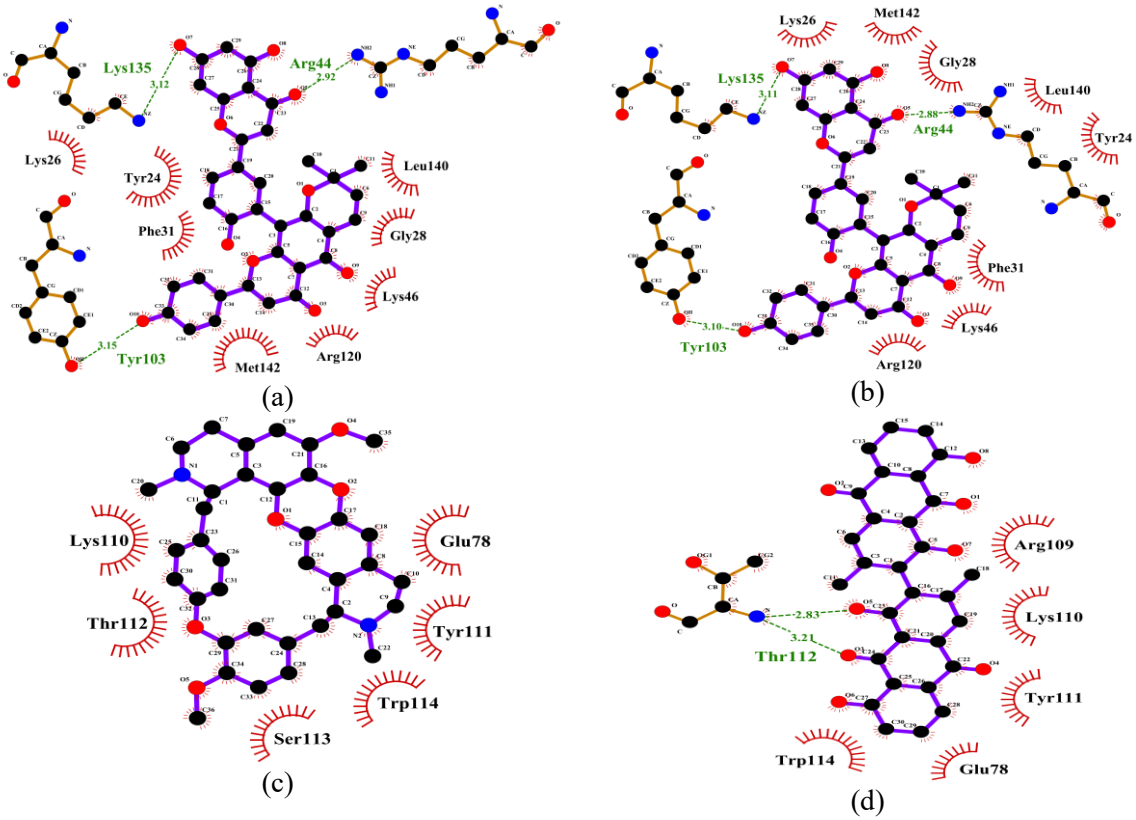

Figure 3. Interaction diagram of the best poses of selected compounds against FGF2, (a) Pyranoamentoflavone, (b) 5,3',5'-Trihydroxy-6,7,4'-trimethoxyflavone, (c) Isotrilobine, and (d) Sotetsuflavone

Table 6 Binding energy values from blind docking of selected compounds with FGF2

Compound	Grid spacing (Å)		
	0.375	0.500	0.625
Pyranoamentoflavone	-6.73	-6.39	-6.15
5,3',5'-Trihydroxy-6,7,4'-trimethoxyflavone	-6.15	-6.84	-6.22
Sotetsuflavone	-7.19	-6.76	-6.29
isotrilobine	-6.52	-6.29	-6.08

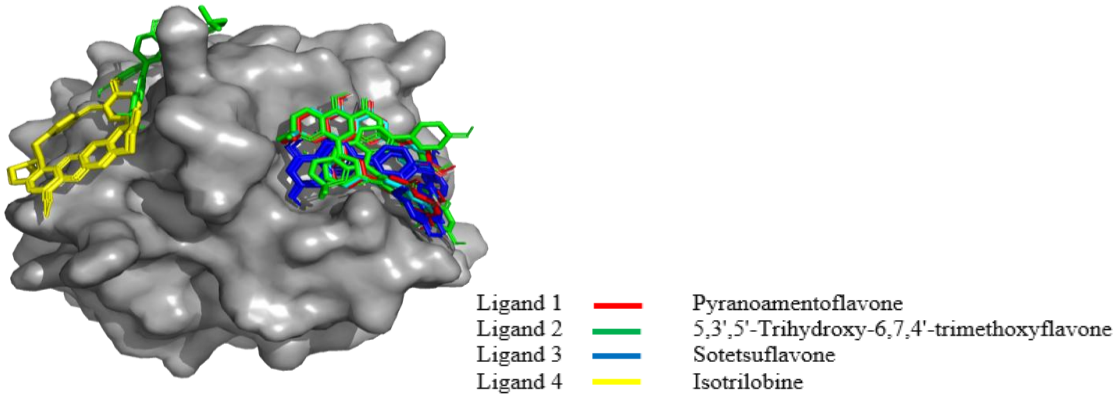

Figure 4. Binding pose of selected compounds resulting from blind docking on the FGF2 protein

4. CONCLUSIONS

In this study, four potential binding sites on the FGF2 protein identified through a protein-protein docking approach with the FGFR1-FGFR4 receptors were used as the basis for virtual screening using molecular docking of 1,496 Indonesian natural compounds. Based on the results of virtual screening using AutoDock Vina, four compounds were selected that consistently showed competitive binding energy values at several binding sites to be further validated using AutoDock4 through targeted docking and blind docking. The analysis results showed that pyranoamentoflavone, 5,3',5'-trihydroxy-6,7,4'-trimethoxyflavone, sotetsuflavone, and isotrilobine have competitive binding affinity to the FGF2 protein. Therefore, these four compounds have the potential as FGF2 inhibitor candidates and require further validation through molecular dynamics simulations as well as in vitro and in vivo studies in the development of targeted glioblastoma therapy based on FGF2 inhibition.

LIST OF REFERENCES

Abdizadeh, T. (2024). Identification of novel potential inhibitors of monkeypox virus thymidine kinase using molecular docking, molecular dynamics simulation and MM/PBSA methods. *Molecular Diversity*, *28*(4), 2513–2546. https://doi.org/10.1007/s11030-023-10692-w

Baell, J. B., & Holloway, G. A. (2010). New substructure filters for removal of pan assay interference compounds (PAINS) from screening libraries and for their exclusion in bioassays. *Journal of Medicinal Chemistry*, *53*(7), 2719–2740. https://doi.org/10.1021/jm901137j

Chen, T., Shu, X., Zhou, H., Beckford, F. A., & Misir, M. (2023). Algorithm selection for protein–ligand docking: strategies and analysis on ACE. *Scientific Reports*, *13*(1), 1–15. https://doi.org/10.1038/s41598-023-35132-5

Copolovici, D., Bungau, S., Boscencu, R., Tit, D. M., & Copolovici, L. (2017). The fatty acids composition and antioxidant activity of walnut cold press oil. *Revista de Chimie*, *68*(3), 507–509.

Daina, A., Michielin, O., & Zoete, V. (2017). SwissADME: a free web tool to evaluate pharmacokinetics, drug-likeness and medicinal chemistry friendliness of small molecules. *Scientific Reports*, *7*(1), 42717. https://doi.org/10.1038/srep42717

Di Stefano, A. L., Fucci, A., Frattini, V., Labussiere, M., Mokhtari, K., Zoppoli, P., Marie, Y., Bruno, A., Boisselier, B., Giry, M., Savatovsky, J., Touat, M., Belaid, H., Kamoun, A., Idbaih, A., Houillier, C., Luo, F. R., Soria, J.-C., Tabernero, J., … Lavarone, A. (2015). Detection, characterization, and inhibition of FGFR–TACC fusions in IDH wild-type glioma. *Clinical Cancer Research*, *21*(14), 3307–3317. https://doi.org/10.1158/1078-0432.CCR-14-2199

Forli, S., Huey, R., Pique, M. E., Sanner, M. F., Goodsell, D. S., & Olson, A. J. (2016). Computational protein–ligand docking and virtual drug screening with the AutoDock suite. *Nature Protocols*, *11*(5), 905–919. https://doi.org/10.1038/pj.2016.37

Garnier, D., Renoult, O., Alves-Guerra, M. C., Paris, F., & Pecqueur, C. (2019). Glioblastoma Stem- Like Cells , Metabolic Strategy to Kill a Challenging Target. *Frontiers in Oncology*, *9*(118), 1–18. https://doi.org/10.3389/fonc.2019.00118

Haley, E. M., & Kim, Y. (2014). The role of basic fibroblast growth factor in glioblastoma multiforme and glioblastoma stem cells and in their in vitro culture. *Cancer Letters*, *346*(1), 1–5.

https://doi.org/10.1016/j.canlet.2013.12.003

Jimenez-pascual, A., Hale, J. S., Kordowski, A., Pugh, J., Silver, D. J., Bayik, D., Roversi, G., Alban, T. J., Rao, S., Chen, R., Mcintyre, T. M., Colombo, G., Taraboletti, G., Holmberg, K. O., Forsberg-nilsson, K., Lathia, J. D., & Siebzehnrubl, F. A. (2019). ADAMDEC1 maintains a growth factor signaling loop in cancer stem cells. *Cancer Discovery*, *9*(11), 1574–1589. https://doi.org/10.1158/2159-8290.CD-18-1308

Khan, W. M. A., Alam, M. J., Sherwani, S., Alouffi, S., Al-Motair, K., Khan, S., & Khan, S. N. (2025). Molecular docking and simulation analysis of glioblastoma cell surface receptors and their ligands: identification of inhibitory drugs targeting fibronectin ligand to potentially halt glioblastoma pathogenesis. *International Journal of Molecular Sciences*, *26*(20), 10038. https://doi.org/10.3390/ijms262010038

Kiametis, A. S., Silva, M. A., Romeiro, L. A., Martins, J. B., & Gargano, R. (2017). Potential acetylcholinesterase inhibitors: molecular docking, molecular dynamics, and in silico prediction. *Journal of Molecular Modeling*, *23*(2), 67. https://doi.org/10.1007/s00894-017-3228-9

Kumari, S., & Kumar, P. (2023). Design and computational analysis of an mmp9 inhibitor in hypoxia-induced glioblastoma multiforme. *ACS Omega*, *8*(11), 10565–10590. https://doi.org/10.1021/acsomega.3c00441

Lee, A. E., Yong, R. L., Paddison, P., & Zhu, J. (2018). Comparison of glioblastoma (GBM) molecular classification methods. *Seminars in Cancer Biology*, *53*, 201–211. https://doi.org/10.1016/j.semcancer.2018.07.006

Meng, X.-Y., Zhang, H.-X., Mezei, M., & Cui, M. (2011). Molecular docking: a powerful approach for structure-based drug discovery. *Current Computer-Aided Drug Design*, *7*(2), 146–157. https://doi.org/10.2174/157340911795677602

Mustafa, G., Mahrosh, H. S., Zafar, M., Attique, S. A., & Arif, R. (2022). Exploring the antihyperglycemic potential of tetrapeptides devised from AdMc1 via different receptor proteins inhibition using in silico approaches. *International Journal of Immunopathology and Pharmacology*, *36*, 1–15. https://doi.org/10.1177/03946320221103120

Mustafa, G., Majid, M., Ghaffar, A., Yameen, M., Samad, H. A., & Mahrosh, H. S. (2020). Screening and molecular docking of selected phytochemicals against NS5B polymerase of hepatitis C virus. *Pakistan Journal of Pharmaceutical Sciences*, *33*(5), 2317–2322. https://doi.org/10.36721/PJPS.2020.33.5.SUP.2317-2322.1

Ornitz, D. M., & Itoh, N. (2015). The fibroblast growth factor signaling pathway. *Wiley Interdisciplinary Reviews: Developmental Biology*, *4*(3), 215–266. https://doi.org/10.1002/wdev.176

Ostrom, Q. T., Patil, N., Cioffi, G., Waite, K., Kruchko, C., & Barnholtz-sloan, J. S. (2020). CBTRUS statistical report: primary brain and other central nervous system tumors diagnosed in the United States in 2013–2017. *Neuro-Oncology*, *22*(1), iv1–iv96. https://doi.org/10.1093/neuonc/noaa200

Sivakumar, K. C., Haixiao, J., Naman, C. B., & Sajeevan, T. P. (2020). Prospects of multitarget drug designing strategies by linking molecular docking and molecular dynamics to explore the protein–ligand recognition process. *Drug Development Research*, *81*(6), 685–699.

https://doi.org/10.1002/ddr.21673

Toyoda, K., Tanaka, K., Nakagawa, S., Thuy, D. H. D., Ujifuku, K., Kamada, K., Hayashi, K., Matsuo, T., Nagata, I., & Niwa, M. (2013). Initial contact of glioblastoma cells with existing normal brain endothelial cells strengthen the barrier function via fibroblast growth factor 2 secretion: a new in vitro blood–brain barrier model. *Cellular and Molecular Neurobiology*, *33*(4), 489–501. https://doi.org/10.1007/s10571-013-9913-z

Trott, O., & Olson, A. J. (2010). AutoDock Vina: improving the speed and accuracy of docking with a new scoring function, efficient optimization, and multithreading. *Journal of Computational Chemistry*, *31*(2), 455–461. https://doi.org/10.1002/jcc.21334